UNIVERSITY OF CYPRUS

DEPARTMENT OF ELECTRICAL AND
COMPUTER ENGINEERING

NOVEL TECHNIQUES FOR RESOLUTION IMPROVEMENT IN OPTICAL COHERENCE TOMOGRAPHY

DOCTOR OF PHILOSOPHY DISSERTATION

EVGENIA BOUSI

2012

Department of Electrical and Computer Engineering
School of Engineering
University of Cyprus

Novel Techniques for Resolution Improvement in Optical Coherence Tomography

Evgenia Bousi

A Dissertation
Submitted in Partial Fulfilment of the Requirements for the
Degree of *Doctor of Philosophy*

July 2012

APPROVAL PAGE FOR THESIS DISSERTATION

SUBMITTED IN FULFILMENT OF THE REQUIREMENTS FOR THE DEGREE OF DOCTOR OF PHILOSOPHY AT THE UNIVERSITY OF CYPRUS BY:

Evgenia Bousi
Candidate

TITLE: **Novel Techniques for Resolution Improvement in Optical Coherence Tomography**

APPROVED:

Stavros Iezekiel Committee Chairperson	Signature
Constantinos Pitris Research Supervisor	Signature
Wolfgang Drexler Committee Member	Signature
Georgios Mitsis Committee Member	Signature
Michalis Averkiou Committee Member	Signature

DATE: July 2012

Abstract

Optical coherence tomography (OCT), a method for cross sectional tissue imaging, is gaining significant ground as a diagnostic tool in various fields. However many early disease changes remain below the resolution of the technique. In OCT the resolution is fundamentally limited by the spectrum of the laser source and the optics used. Enhancements can only be marginal since the spectral increase required for further axial resolution improvement cannot be supported even by the highest end lasers. The lateral resolution of OCT can be improved by use of high numerical aperture (NA) objectives. However, use of a high NA objective restricts the depth of focus**.** In this dissertation we propose some novel methods for axial and lateral resolution improvement which are independent of the above limitations, providing the opportunity for cellular and sub-cellular resolution imaging, without increasing the cost and complexity of the system.

A method for axial resolution improvement was developed, which was based on the modulation of the axial PSF of the system. With this method the axial resolution may be improved by a factor of 7. The application of this method in time domain OCT differs significantly from that in frequency domain OCT systems. However different formulations have been developed for both. Their mechanical basis and experimental validation are presented in this thesis.

A method for lateral resolution improvement based on the oversampling of the OCT images was also developed. The information in the oversampled OCT images was used to estimate the locations of multiple scatterers, assuming each contributes a weighted portion to the detected signal. This method was applied to laterally oversampled OCT images, and a resolution improvement of a factor of 3.7 was experimentally demonstrated.

The theoretical and experimental framework developed in this thesis can significantly improve the resolution of OCT images allowing imaging of diagnostically crucial cellular level characteristics. Such technological improvements can increase the effectiveness of OCT as a tool for diagnosis of very early cancer and other diseases.

Περίληψη

Η Οπτικά Σύμφωνη Τομογραφία (ΟΣΤ), είναι μια μέθοδος οπτικής απεικόνισης της εσωτερικής δομής των ιστών, και κερδίζει ολοένα και πιο σημαντικό έδαφος ως εργαλείο διάγνωσης σε διάφορους τομείς. Ωστόσο, οι αλλαγές που συμβαίνουν σε πρώιμα στάδια αρκετών ασθενειών παραμένουν κάτω από την ευκρίνεια (διακριτική ικανότητα) της μεθόδου αυτής. Η ευκρίνεια της μεθόδου ΟΣΤ περιορίζεται θεμελιωδώς από το φάσμα της πηγής λέιζερ και τα χαρακτηριστικά των οπτικών μέσων που χρησιμοποιούνται. Η χρήση αναβαθμισμένων μέσων προκαλεί οριακές (μικρές) βελτιώσεις στην ανάλυση αφού η φασματική αύξηση που απαιτείται για περαιτέρω βελτίωση της αξονικής ευκρίνειας δεν υποστηρίζεται ούτε από τα λέιζερ τελευταίας τεχνολογίας. Η εγκάρσια ευκρίνεια της μεθόδου ΟΣΤ μπορεί να βελτιωθεί με τη χρήση οπτικών φακών μεγάλου αριθμητικού ανοίγματος (ΑΑ). Ωστόσο, η χρήση οπτικών φακών με μεγάλο αριθμητικό άνοιγμα περιορίζει το βάθος της εστίασης. Αυτή η διδακτορική διατριβή προτείνει νέες μεθόδους για βελτίωση της αξονικής και εγκάρσιας ευκρίνειας των συστημάτων ΟΣΤ, που είναι ανεξάρτητες από τους παραπάνω περιορισμούς, παρέχοντας τη δυνατότητα απεικόνισης με κυτταρική και ενδοκυτταρική ευκρίνεια, χωρίς να αυξήσει το κόστος και την πολυπλοκότητα του συστήματος.

Η μέθοδος που αναπτύχθηκε για την βελτίωση της αξονικής ευκρίνειας, βασίζεται στην διαμόρφωση της αξονικής συνάρτησης μεταφοράς (ΣΜΣ) του συστήματος. Με αυτή τη μέθοδο η αξονική ευκρίνεια μπορεί να βελτιωθεί κατά επτά φορές. Η εφαρμογή αυτής της μεθόδου σε συστήματα ΟΣΤ που λειτουργούν στο πεδίο του χρόνου διαφέρει σημαντικά από τα συστήματα ΟΣΤ που λειτουργούν στο πεδίο της συχνότητας. Για αυτό αναπτύχτηκαν δυο ξεχωριστές μεθοδολογίες-διατυπώσεις για την εφαρμογή της μεθόδου αυτής και στους δυο τύπους συστημάτων ΟΣΤ. Οι αρχές λειτουργίας και η πειραματική εφαρμογή και αξιολόγηση της μεθόδου και για τους δυο τύπους συστημάτων παρουσιάζεται σε αυτήν την διατριβή.

Επίσης, αναπτύχθηκε μια μέθοδος για την βελτίωση της εγκάρσιας ευκρίνειας που βασίζεται στην υπερδειγματοληψία (oversampling) των εικόνων ΟΣΤ. Η επιπλέον πληροφορία που εμπεριέχεται στις υπερδειγματοληπτύμενες εικόνες ΟΣΤ χρησιμοποιήθηκε για την εκτίμηση των θέσεων των πολλαπλών σκεδαστών, υποθέτοντας ότι κάθε σκεδαστής συμβάλλει ένα σταθμισμένο ποσοστό στο

ανιχνευόμενο σήμα. Η μέθοδος αυτή εφαρμόστηκε σε εγκάρσιως υπερδειγματοληπτούμενες εικόνες ΟΣΤ και η βελτίωση της εγκάρσιας ευκρίνειας κατά έναν συντελεστή 3.7 παρουσιάζεται πειραματικά σε αυτήν την διατριβή.

Το θεωρητικό και πειραματικό πλαίσιο που αναπτύχθηκε σε αυτή τη διδακτορική διατριβή μπορεί να βελτιώσει σημαντικά την ευκρίνεια των εικόνων ΟΣΤ επιτρέποντας την απεικόνιση διαγνωστικά κρίσιμων και ζωτικής σημασίας χαρακτηριστικών σε κυτταρικό επίπεδο. Τέτοιες τεχνολογικές βελτιώσεις μπορεί να αυξήσουν την αποτελεσματικότητα της ΟΣΤ ως ένα εργαλείο για τη διάγνωση των πρώιμων σταδίων του καρκίνου και άλλων ασθενειών

Acknowledgements

First and foremost, I would like to express my sincere gratitude to my supervisor Dr. Constantinos Pitris, for his valuable guidance and many encouragements during this project. Working with him has been both pleasant and very fruitful for my personal and professional development.

Special thanks to my colleagues and friends at the University of Cyprus for their helpfulness, useful discussions and encouragement at all times.

For financial support, I am very grateful to the Kios Reasearch Center for Intelligent Systems and Networks, and to the Cyprus Research Promotion Foundation.

Finally, I would like to thank my family that have been next to me with their love and support all the time.

To my husband and son

Contents

CHAPTER 1 1

1. INTRODUCTION 1
1.1 Motivation 3
1.2 Aim of the Thesis 4
1.3 Research Objectives 5
1.4 Dissertation Organization and Overview 5
1.4.1 Dissertation Organization 5
1.4.2 Dissertation Overview 6

CHAPTER 2 9

2. OPTICAL COHERENCE TOMOGRAPHY: INTRODUCTION AND THEORY 9
2.1 Summary 9
2.2 Introduction 9
2.3 Development of OCT: 10
2.3.1 Time-Domain OCT 12
2.3.2 Fourier-Domain OCT 13
2.4 OCT Theory 14
2.4.1 Low Coherence Interferometry 14
2.4.2 OCT Signal from Multiple Scatterers 18
2.4.3 Time Domain Optical Coherence Tomography (TD OCT) 20
2.4.4 Fourier Domain Optical Coherence Tomography 22
2.4.5 Wavelength Tuning (Swept Source) OCT 27
2.4.6 Spatial Resolution in Optical Coherence Tomography 29
2.4.6.1 Axial Resolution 29
2.4.6.2 Transverse Resolution 30
2.4.7 Axial Range Limitations 31
2.5 Clinical Applications of OCT 33
2.6 Conclusions 34

CHAPTER 3 37

3. SWEPT SOURCE OCT SYSTEM IMPLEMENTATION 37
3.1 Summary 37
3.2 System Implementation 37
3.3 Data Acquisition 39
3.4 Digital signal and image processing 44
3.4.1 Background subtraction 44
3.4.2 Interpolation to linear k-space 44
3.5 System Characterization 47
3.5.1 Dynamic Range 47
3.5.2 Imaging Range 47
3.5.3 Sensitivity Roll –off 48
3.5.4 Axial Resolution 48
3.5.5 Lateral Resolution 49

CHAPTER 4 51

4. Optical Coherence Tomography Axial Resolution Improvement by Step-frequency Encoding 51
4.1 Summary 51
4.2 Introduction 51
4.3 Methodology 53
4.3.1 Frequency Summation in Optical Coherence Tomography 54
4.3.1.1 Frequency Summation 55
4.3.1.2 Discrete Reflectors 56
4.3.2 Deconvolution of the OCT signal 57
4.3.3 Step Frequency Encoding, Resolution Enhancement, and Limitations 60
4.3.3.1 Axial Resolution Improvement with Step Frequency Encoding and Deconvolution 60
4.3.3.2 Sidelobe Amplitude 61
4.3.3.3 Location Shift 62
4.3.3.4. Design Trade-offs 64
4.4 Experimental Method 64
4.5. Results 66
4.6 Conclusion 71

CHAPTER 5 73

5. Axial Resolution Improvement by Modulated Deconvolution in Fourier Domain Optical Coherence Tomography 73
5.1 Summary 73
5.2 Introduction 74
5.3. Methodology 74
5.3.1 Frequency Summation 74
5.3.2 Selection of Shift Amount 76
5.3.3 Multiple Discrete Reflectors 76
5.3.4 Quantization of Position 77
5.3.4 Modulated Deconvolution, Resolution Enhancement, and Limitations 80
5.3.4.1 Axial Resolution Improvement with Modulated Deconvolution 80
5.3.4.2 Sidelobe amplitude and location shift 81
5.3.4.3. Design Trade-offs 82
5.4. Experimental Method 83
5.5 Results 85
5.6. Conclusion 90

CHAPTER 6 93

6. Lateral Resolution Improvement using Oversampling 93
6.1 Summary 93
6.2 Introduction 94
6.3 Theory 95
6.4. Methodology 96
6.4.1 Resolution Enhancement using Capon's Method. 99
6.4.1.1 Capon Spectral Estimation. 99
6.4.1.2 Adaptation of Capon to Laterally Oversampled OCT. 100
6.4.2 PSF Estimation 101
6.5 Experimental Results 102
6.5.1 Inverse Matrix Solution 103
6.5.2 Weighting Method. 105
6.5.2.1 Method 1 105
6.5.2.2 Method 2 107
6.5.2.3 Method 3 109
6.6 Conclusion 111

CHAPTER 7 113

7. Conclusion and Future work 113
7.1 Conclusion 113
7.2 Future Work 116
7.3 Contributions of the Thesis 117

BIBLIOGRAPHY 119

LIST OF PUBLICATIONS OUT OF THESIS..... 127

List of Figures

Figure 2.1 Principle of OCT. OCT measures the backscattering intensity as a function of depth. Cross-sectional images are generated by scanning a beam across the tissue. A gray scale or false color image can then be displayed. [18]..... 10

Figure 2.2 Schematic of low coherence interferometry..... 12

Figure 2.3 Michelson interferometer used for low coherence interferometry. 15

Figure 2.4Typical fiber-optic implementation of time domain OCT system, interferogram and the A-Scan envelope..... 21

Figure 2.5 Typical fiber-optic implementation of Fourier Domain OCT, spectrogram, backreflection profile. 23

Figure 2.6 Amplitude of the results of the Fourier transform of the spectral interferogram recorded with FD OCT. 27

Figure 2.7 Typical fiber-optic implementation of Swept Source OCT, interferogram, and backreflection profile. 29

Figure 3.1 SSOCT configuration setup..... 38

Figure 3.2 A photograph of the Swept Source OCT System..... 39

Figure 3.3 Labview user interface for data acquisition..... 40

Figure 3.4 Flow diagram of data acquisition process 42

Figure 3.5 Synchronization diagram for data acquisition.(a) The trigger TTL pulse from the source for each A-scan acquisition.(b) (red) trigger pulse synchronized with the beginning of each sweep, (black) acquisition of A-scans with the DAQ. (c) Trigger signal for image acquisition and waveform generation for transversal scanning (image consists of 500 lines) . (d) Waveform for transversal scanning. 43

Figure 3.6 Electrical connection diagram 43

Figure 3.7 A-scans from a mirror obtained at different depths. Blue line are the A-scans without interpolation, and red line are the A-scans after interpolation. 47

Figure 4.1 Axial resolution versus bandwidth illustrating the asymptotic relationship between axial resolution and bandwidth..... 52

Figure 4.2 Beating of the interferogram of a single peak. 56

Figure 4.3 Dependence of sidelobes from frequency steps. (a) 3kHz frequency difference between steps. (b) 6kHz frequency difference between steps. Intensity scales are linear. 62

Figure 4.4 Different beating patterns as a result of different phases of interferograms.(a) zero distance shift corresponding to zero phase shift of the main lobe from the real position. (b), maximum distance shift corresponding to $\pi/2$ phase shift of the main lobe from the real position. Intensity scales are linear. 63

Figure 4.5 Configuration of the experimental time domain (TD) OCT system 65

Figure 4.6 Sample, consisting of 3 microscope cover slips (~ 170 μm thickness, spaced at ~ 170 μm apart), used to collect the interferograms of 6 individual peaks from each A-Scan. They were subsequently used as kernels for the deconvolution. 66

Figure 4.7 Sample consisting of two tightly adjacent microscope slides used to evaluate the resolving power of the proposed technique. 66

Figure 4.8 (a) Single peaks from demodulated standard OCT interferogram used as kernels for deconvolution. (b) Single peaks from demodulated encoded OCT interferogram used as kernels for deconvolution. (c) A-Scan from standard OCT (blue line), and deconvolution of demodulated A-Scans from standard (red line) and encoded OCT(black line) in one plot for comparison reasons. (d) Center peak of Fig. 4.8(c). (e) First peak of Fig. 4.8(c). y axis normalized, (a) and (b) normalized to 1, (d) and (e) normalized to the highest peak of (c). Intensity scales are linear. 67

Figure 4.9 (a) Onion imaged with standard OCT, (b) after deconvolution of the standard OCT image, (c) onion imaged with encoded OCT after deconvolution and (d) onion image with encoded OCT after deconvolution and motion correction. (Image size: 1.5mm x 0.5 mm). The area in the red rectangle appears in Fig. 4.10. Intensity scales are log. 69

Figure 4.10 (a) Onion imaged with standard OCT, (b) after deconvolution of the standard OCT image, (c) onion imaged with encoded OCT after deconvolution., (d) onion image with encoded OCT after deconvolution and motion correction and (e) Light microscopy image of onion cells. (Image size: 0,5mm x 0,2 mm). Intensity scales are log. 69

Figure 4.11 (a) Rabbit lung parenchyma imaged *ex vivo* with standard OCT, (b) after deconvolution of the standard OCT image, and (c) imaged with encoded OCT after deconvolution. (Image size: 0,5mm x 0,5 mm). (d – f) Details of images a-c, where small alveoli are indicated by the arrow. (e) Light microscopy image of a section of lung parenchyma from an unrelated site included for reference purposes. Intensity scales are log. 70

Figure 4.12 Speckle images from (a) standard OCT, (b) deconvolution of standard OCT, and (c) step-frequency encoded and deconvoluted OCT. The images are displayed using the same contrast and brightness scale for comparison purposes. Each image is 1.5x0.8 mm. Intensity scales are log. 71

Figure 4.13 Single OCT A-Scans from the images of Fig. 9: standard OCT (blue), deconvoluted standard OCT (red), and encoded and deconvoluted OCT

(green) signals. Specular reflections appear at the surface of the sample (at 0.2 mm). 71

Figure 5.1 (a) Backscattered signal from a sample consisting of seven peaks, (b) signal from the same point shifted in relation to the first, (c) characteristic beating patterns at each peak after summation of two A-scans and FFT, and (d) a single peak from standard FDOCT and modulated FDOCT for comparison. 76

Figure 5.2 (a) black line: Beating frequency which is constant for all A-scans. Blue and red line: two adjacent A-scans. (b) black line: Beating frequency which is constant for all A-scans. Blue and red line: two modulated adjacent A-scans after multiplication with the beating frequency. After deconvolution the two scatterers cannot be resolved..... 79

Figure 5.3 (a) blue and red line: Beating frequencies (which are different) and two adjacent A-scans. (b) blue and red line: two modulated adjacent A-scans after multiplication with their corresponding beating frequencies. After deconvolution the two scatterers can be resolved. 79

Figure 5.4 Two different beating patterns resulting from two different scatterer locations of Figure 1(c). (a) zero distance shift of the main lobe from the real position. (b), maximum distance shift of the main lobe from the real position. Intensity scales are linear. 82

Figure 5.5 Configuration of the experimental swept source OCT system..... 84

Figure 5.6 Sample, consisting of three microscope cover slips (~ 170 μm thickness, spaced at ~ 170 μm apart), used to collect the interferograms of 6 individual peaks from each A-scan. 85

Figure 5.7 Sample consisting of two tightly adjacent microscope slides used to evaluate the resolving power of the proposed technique. 85

Figure 5.8 Single peaks from (a) a standard OCT interferogram and (b) a modulated OCT interferogram used as kernels for deconvolution. (c) A-scan from standard OCT (blue line), and deconvolution of demodulated A-scans from standard (red line) and modulated OCT (black line) in one plot for comparison reasons. (d) Intermediate modulated deconvolution results for the first peak of Fig. 5.8(c). (e) and (g) Center peak of Fig. 5.8(c). (f) and (h) Last peak of Fig. 5.8(c). The y axis is normalized to 1 for (a) and (b) and normalized to the highest peak of (c) for (e) and (f). 86

Figure 5.9 (a) Standard OCT image of an onion. (b) Same image after deconvolution. (c) Same data after modulated deconvolution. (Image size: 1.15 mm x 1.35 mm). The area in the red rectangle appears in Fig. 5.10. Intensity scales are normalized log. 88

Figure 5.10 (a) Standard OCT image of an onion. (b) Same image after deconvolution. (c) Same data after modulated deconvolution. (d) Light microscopy image of onion cells. (Image size: 0.65 mm x 0.40 mm). Intensity scales are normalized log. 88

Figure 5.11 (a) Rabbit lung parenchyma imaged *ex vivo* with standard OCT. (b) Same image after deconvolution. (c) Same data after modulated deconvolution. (Image size: 1.2 mm x 0.83 mm). (d – f) Details of images (a)-(c), where

small alveoli are indicated by the arrow. (g) Light microscopy image of a section of lung parenchyma from an unrelated site included for reference purposes. Intensity scales are normalized log. 89

Figure 5.12 (a) *In vivo*, standard OCT, image of skin (finger tip). (Image size: 1.15 mm x 2.7 mm). (b) Close up of the region marked with the rectangle in (a). (c) Same section after deconvolution of the standard OCT image. (d) Same data after modulated deconvolution. The area of the sweat duct (marked with d) clearly exhibits characteristic tubular structure. Areas of speckle are also indicated (marked with s). Intensity scales are normalized log..... 89

Figure 6.1 Resolution and depth of focus for a high numerical aperture and a low numerical aperture lens. 96

Figure 6.2 A schematic diagram of L=3 lateral oversampling. Each oversampled signal Vi(t) consists of independent signals from L subvolumes (S_i to S_{L+i-1}) [107] 97

Figure 6.3 A schematic diagram of *L*=3 lateral oversampling and a Gaussian PSF. Each oversampled signal $V_i(t)$ consists of independent signals from *L* subvolumes (S_i *to* S_{L+i-1})..... 98

Figure 6.4 (a) The image to be processed. (b) PSFs estimated with the blind deconvolution algorithm from 3 different depths of (a). 103

Figure 6.5 (a) Standard OCT image. (b) Deconvolution of Standard OCT image. (c) Inverse solution of OCT image without filtering. (d) Inverse solution of regular OCT image with filtering. (e) Zoomed region of the area in the red rectangle of (a). (f) Zoomed region of the area in the red rectangle of (b). (g) Zoomed region of the area in the red rectangle of (d). (h) The line in the position indicated by the arrow (Red line: Standard OCT. Green line: Deconvoluted OCT. Blue line: Inverse solution)..... 104

Figure 6.6 (a) the Standard OCT image. (b) The deconvoluted OCT image with the estimated PSF. (c) The OCT image after applying the weighting method. (e) Zoomed region of the area in the red rectangle of (a). (f) Zoomed region of the area in the red rectangle of (b). (g) Zoomed region of the area in the red rectangle of (c). (h) The line in the position indicated by the arrow (Red line: Standard OCT. Green line: Deconvoluted OCT. Blue line: Weighting method 1) 106

Figure 6.7 (a) the Standard OCT image. (b) The deconvoluted OCT image with the estimated PSF. (c) The OCT image after applying the weighting method. (e) Zoomed region of the area in the red rectangle of (a). (f) Zoomed region of the area in the red rectangle of (b). (g) Zoomed region of the area in the red rectangle of (c). (h) The line in the position indicated by the arrow (Red line: Standard OCT. Green line: Deconvoluted OCT. Blue line: Weighting method 2) 108

Figure 6.8 (a) the Standard OCT image. (b) The deconvoluted OCT image with the estimated PSF. (c) The OCT image after applying the weighting method. (e) Zoomed region of the area in the red rectangle of (a). (f) Zoomed region of the area in the red rectangle of (b). (g) Zoomed region of the area in the red rectangle of (c). (h) The line in the position indicated by the

arrow (Red line: Standard OCT. Green line: Deconvoluted OCT. Blue line: Weighting method 3)). 110

Figure 6.9 (a) Standard OCT image, (b) Deconvoluted OCT image with the estimated PSF. (c) The same image after applying the weighting method. (d) The line at the position indicated by the arrow (Red line: Standard OCT, Green line: deconvoluted OCT, black line: weighting method). 111

List of Tables

Table 5.1 Quantitative assessment of SNR and CNR of images in Fig 5.7. 90

Table 6.1 Measurments of PSFs for Standard, Deconvoluted and Inverse Solution OCT images, as well as SNR for Standard, Deconvoluted, and Inverse Solution OCT images. 105

Table 6.2 Measurements of PSFs for Standard OCT, Deconvoluted OCT and Weighting method, as well as SNR for Standard OCT, Deconvoluted OCT, and Weighting method. 106

Table 6.3 Measurments of PSFs for Standard OCT, Deconvoluted OCT and Weighting method, as well as SNR for Standard OCT, Deconvoluted OCT, and Weighting method. 108

Table 6.4 Measurments of PSFs for Standard OCT, Deconvoluted OCT and Weighting method, as well as SNR for Standard OCT, Deconvoluted OCT, and Weighting method. 110

Chapter 1

Introduction

Optical coherence tomography (OCT) is a diagnostic medical imaging technology for performing high-resolution cross-sectional imaging. OCT is analogous to ultrasound imaging expect that is based on the detection of infrared light waves backscattered (reflected) from different layers and structures within the tissue rather than sound. However, unlike ultrasound, the speed of light is very high, rendering electronic measurement of the echo delay time of the reflected light (time for the signal to return) impossible. Similar measurements can be performed using a technique known as low coherence interferometry. Within the interferometer, the light beam from the optical light source is split into two parts, a reference and a sample beam. The reference beam is reflected off a mirror at a known distance and returns to the detector. The sample beam reflects off different layers within the tissue and the light returning from the sample and reference arms combines. If the two beams have travelled the same distance (optical path length) the two beams will interfere. OCT measures the intensity of interference obtained from different points within the tissue by moving the mirror in the reference arm that changes the distance light travels in that arm. Low coherence can be used to localize backreflection sites and provide the desired high resolution by limiting the interference pattern to a coherence length of mismatch between the two arms. Two or three-dimensional images are produced by scanning the beam across the sample and recording the optical backscattering versus depth at different transverse positions. The resulting data is a two or three dimensional representation of the optical backscattering of the sample on a micrometer scale. The logarithm of the backscattering signal is represented as a false color or a gray scale image. Image resolutions of 1-15 μm can be achieved with this method which is one to two orders of magnitude higher than conventional ultrasound. The main

disadvantage of OCT is that, in most tissues, the optical scattering limits the image penetration depth to 2-3 mm.

OCT imaging was first demonstrated in 1991 [1] for cross-sectional imaging of the retina and coronary artery. The first *in vivo* OCT images of the human retina were demonstrated in 1993 [2][3], and since then ophthalmology remains the most developed application area of OCT.

With recent advances in OCT technology, providing faster acquisition speeds and better sensitivity and resolution, this technique has developed into a noninvasive diagnostic imaging modality with ubiquitous applications [4][5][6].Clinical applications of OCT have emerged in a variety of fields including further advances in ophthalmology, intravascular imaging in cardiology, and applications in oncology, gastroenterology, dermatology, dentistry, urology, gynecology and many others. However, many of the hallmark changes associated with early cancer are not discernible even with this advanced OCT technology. As a result, further resolution improvement is required for the identification of these subtle changes. Unfortunately, resolution is fundamentally limited by the spectrum of the laser source and the optics used. Enhancements of the axial resolution can only be marginal since the spectral increase required for further improvement cannot be supported by even the highest end lasers. The lateral resolution of OCT can be improved by the use of high numerical aperture (NA) objectives. However, use of a high NA objective severely restricts the depth of focus and significantly degrades the resolution for out of focus layers.

Deconvolution algorithms have shown to improve the axial and lateral resolution in OCT. Commonly used deconvolution algorithms include iterative methods, such as the Jansson-van Cittert algorithm [7], algorithms based on Fourier filtering, such as the Wiener filter method and classical least-squares regularization methods based on the minimization of a Tikhonov functional [8], and algorithms based on Bayesian inference, the most popular being the Richardson-Lucy [9] algorithm which is shown to give better performance in image contrast and quality for OCT imaging [10]

In addition high resolution algorithms for multiple scatterer localization have been used in radar imaging. Perhaps the most widely used algorithms, are the MUSIC [11] and Capon's algorithms [12]. The MUSIC algorithm takes advantage of the autocorrelation matrix eigenstructure, resulting in a decomposition of the space into

two orthogonal subspaces, called the signal and noise subspace. This technique offer good resolution, however selection of the the number of scattering centers poses a considerable challenge. Capon's maximum- likelihood (ML) method was an early attempt at high- resolution spectrum estimation based on an optimality criterion. It is also known as the minimum-variance distortionless response (MVDR) and the reduced-variance distortionless response (RVDR). With this technique the resolution is improved by minimizing the energy contributed by interferers while keeping unit gain on the location of interest.

In this dissertation we propose some novel methods for axial and lateral resolution improvement which will be independent from the source bandwidth and the optics used, giving the opportunity for cellular and sub-cellular resolution imaging. For axial resolution improvement the methods are based on the modulation of the axial PSF of the system, and subsequently deconvolution with appropriately chosen modulated kernel functions. The Lucy Richardson algorithm is used for deconvolution operation. For lateral resolution improvement the method is based on the oversampling and estimation of the locations of the multiple scatterers which contribute to the signal. The information in the oversampled images is used to estimate the locations of multiple scatterers assuming each contributes a weighted portion to the detected signal. The weights are obtained using the Capon's algorithm described above.

1.1 Motivation

Imaging at cellular and subcellular level resolutions is important for the diagnosis of early neoplasias as well as other applications. Early neoplastic changes are characterized by accelerated rate of growth, mass growth, local invasion, lack of differentiation, anaplasia and metastasis. For the correct identification and grading of neoplasias, it is necessary to evaluate such structural and cellular features. Glandular organization and architectural morphology can be imaged with OCT and any change in their architecture, is easy to identify since they fall within the resolution limits of most standard resolution OCT systems. However, preliminary OCT imaging studies have not yet demonstrated the ability to differentiate sub-cellular morphologic changes. Consequently the ability to diagnose and grade dysplastic early changes remains an open question. In ophthalmology, high resolution imaging of retinal features such as retinal thickness and retinal nerve fiber layer thickness, would allow

for detection and screening of macular edema and glaucoma. Additional improvements in resolution would allow those measurements to be performed with increased accuracy.

The axial resolution of OCT is determined by the coherence length of the light source used for imaging. Broad bandwidth light sources are necessary for high resolution OCT imaging. In addition, for a sufficient signal to noise ratio light sources with powers of several milliwats are typically necessary. One approach for achieving high resolution is to use short pulse femptosecond solid state lasers as light sources[13][14]. However these light sources are not clinically viable because of their complexity and expense. In addition, due to the asymptotic inverse dependence of resolution on bandwidth, significant increases in bandwidth are required even for marginal resolution improvement.

The transverse resolution depends on the focusing characteristics of the objective lens. The use of high numerical aperture (NA) objectives results in high transverse resolution. Unfortunately, high NA also results in a decrease in the depth of field.

In this dissertation, we investigate methods for axial and lateral resolution improvement without the need to further increase the bandwidth of the light source or restrict the depth of focus. Those methods can be applied to any OCT system and significantly enhance its axial and lateral resolution.

1.2 Aim of the Thesis

The aim of this thesis is to develop techniques for improving the axial and lateral resolution of OCT systems, without any noticeable adverse effects on the system's complexity cost, and performance.

A novel technique for axial resolution improvement has been developed and applied to a time domain OCT and a Fourier domain OCT system. This novel technique is inspired from radar and ultrasound and is based on the modulation of the point spread function (PSF) of the system. In radar and ultrasound it has been shown that superior performance can be obtained with smart manipulations of the space and frequency characteristics of the beams. OCT is not analogous to ultrasound but we draw inspiration and create a method to apply modulation to an OCT beam.

A technique for lateral resolution improvement has also been developed and applied to OCT images. This technique is based on oversampling, and is also inspired from radar. It has been shown that this technique can improve the radar range resolution, and its implementation for OCT can also improve the lateral resolution of oversampled OCT images.

These techniques can significantly improve the resolution of OCT images, allowing imaging of diagnostically important cellular level characteristics and thus increasing the effectiveness of OCT as a tool for diagnosis of very early cancer and other diseases.

1.3 Research Objectives

The main research objectives of this work are summarised as follows:

- Development of a swept source optical coherence tomography (SSOCT) system which has been used to confirm experimentally the result of the theoretical investigations.
- Investigation of methods for axial resolution improvement of a time domain OCT system.
- Experimental confirmation of the applicability of those methods to a time domain OCT system
- Investigation of methods for axial resolution improvement of a Fourier domain OCT system.
- Experimental confirmation of the applicability of those methods to a swept source OCT (SSOCT) system.
- Investigation of methods for lateral resolution improvement of OCT systems.
- Experimental confirmation of the applicability of the above methods to a SSOCT system.

1.4 Dissertation Organization and Overview

1.4.1 Dissertation Organization

The thesis is divided and organised into seven chapters.

Specifically, **Chapter 1** is the introduction and includes the motivation, the aim and the research objectives of the proposed thesis. **Chapter 2** presents a detailed theoretical analysis of optical coherence tomography. It begins with a general description of the technique, a historical overview of its development follows, and subsequently the various technologies are described. Finally an extensive theoretical analysis behind each technology is presented. In **Chapter 3**, a detailed description of the implementation of a swept source OCT system, is presented, followed by the characterization of the system. **Chapter 4** includes a method for axial resolution improvement in a time domain OCT system. The chapter begins with a literature review, related to the topic. The description of the methodology follows, and finally the experimental evaluation of the technique and the experimental results are presented. In **Chapter 5** we present a method for axial resolution improvement in a swept source OCT system. It begins with a description of the methodology. The experimental evaluation of the technique and experimental results follows. In **Chapter 6** we present a method for lateral resolution improvement of OCT systems. As before the chapter begins with a literature review, related to the topic. It is followed by a description of the methodology, the experimental evaluation of the technique, and the experimental results. Finally, in the last chapter, **Chapter 7**, conclusions, future work and contributions will be presented.

1.4.2 Dissertation Overview

The summary of each chapter follows:

Chapter 2 presents the background of OCT. The first part of this chapter is a general introduction to OCT. In the second part the development of OCT from a historical perspective will be reviewed, including an overview of the technology, and the capabilities of OCT imaging systems. In the third part the basic theoretical background is provided, and finally clinical applications of OCT are presented.

Chapter 3 describes the swept source OCT system developed in our lab. First, the implementation of the system will be presented and afterwards the system characterization will follow. The implementation of the system consists of hardware

implementation, and data acquisition. In addition, some post processing procedures which are necessary for the swept source OCT signal will be described.

Chapter 4 presents a novel technique for axial resolution improvement of optical coherence tomography (OCT) systems. The technique is based on step-frequency encoding, using frequency shifting, of the OCT signal. A resolution improvement by a factor of ~ 7 is achieved without the need for a broader bandwidth light source. This method exploits a combination of two basic principles: the appearance of beating, when adding two signals of slightly different carrier frequencies, and the resolution improvement by deconvolution of the interferogram with an encoded autocorrelation function. In time domain OCT, step-frequency encoding can be implemented by performing two scans, with different carrier frequencies, and subsequently adding them to create the encoded signal. When the frequency steps are properly selected, deconvolution of the resulting interferogram, using appropriate kernels, results in a narrower resolution width.

Chapter 5 describes a novel technique for axial resolution improvement in Fourier domain optical coherence tomography (FDOCT). The technique is based on the deconvolution of modulated OCT signals. In FDOCT, the real part of the Fourier transform of the interferogram is modulated by a frequency which depends on the position of the interferogram in *k* space. A slight numerical *k* shift, results in a different modulation frequency. By adding two shifted signals, beating can appear in the A-scan. When the amount of shifting is appropriately selected, deconvolution of the resulting depth profile, using suitable modulated kernels, yields a narrower resolution width. A resolution improvement by a factor of ~ 7 can be achieved without the need for a broader bandwidth light source.

Chapter 6 discusses a novel method for lateral resolution improvement of optical coherence tomography (OCT) images, which is independent of the focusing of the delivery optics and the depth of field. This method was inspired by radar range oversampling techniques. It is based on the lateral oversampling of the image and the estimation of the locations of the multiple scatterers which contribute to the signal. The information in the oversampled images is used to estimate the locations of multiple scatterers, assuming each contributes a weighted portion to the detected signal, the weight determined by the location of the scatterer and the point spread

function (PSF) of the system. *A priori* knowledge of the PSF is not required since there are methods to sufficiently estimate it from the image. Results of such an approach on laterally oversampled OCT images have shown that it is possible to achieve a several fold lateral resolution improvement. Such improvement can be significant, especially in cases where the numerical aperture (NA) of the delivery optics is limited, such as, for example, in the case of ophthalmic imaging where the optics of the eye itself limits the lateral resolution.

Chapter 7 presents some concluding remarks and indicates possible future directions. Contributions of this work are also presented in this chapter.

Chapter 2
Optical Coherence Tomography: Introduction and Theory

2.1 Summary

Optical coherence tomography (OCT) is a diagnostic medical imaging technology that has found widespread applications in various medical fields. The first part of this chapter is a general introduction to OCT. In the second part, the development of the OCT from a historical perspective will be overviewed, including an overview of the technology, and a description of the capabilities of OCT imaging systems. In the third part, the basic theoretical background is provided, and finally clinical applications of OCT are presented.

2.2 Introduction

OCT is an emerging medical imaging technology which enables micrometer scale, cross-sectional and three-dimensional imaging of the microstructure of biological tissues *in situ* and in real time [1][15][4]. OCT can function as a type of "optical biopsy" imaging tissue microstructure with 1-10 μm resolutions and 1-3mm penetration depths, approaching those of standard excisional biopsy and histopathology, but without the need to remove and process tissue specimens [5][16][17]. OCT is analogous to ultrasound B-mode imaging, except that imaging is performed by measuring the intensity of back-reflected or backscattered light rather than sound. An optical beam is scanned across the tissue and backscattered light is

measured as a function of axial range (depth) and transverse position (Fig. 2.1). Two-dimensional cross-sectional OCT images of tissue are constructed by juxtaposing a series of axial measurements at different transverse positions. The resulting data set is a two-dimensional array which represents the optical backscattering within a cross-sectional slice of the tissue. Three-dimensional imaging can also be created by stacking the two-dimensional cross-sectional images at different transverse positions.

OCT imaging has a number of features which make it attractive for a broad range of applications. OCT can perform imaging with resolutions approaching that of conventional histopathology, but imaging is possible *in situ* and in real time. OCT can be implemented fiber-optically using devices such as handheld probes, endoscopes, catheters, laparoscopes, and needles which enable non-invasive or minimally invasive internal body imaging. OCT can be performed in real time, allowing guidance of excisional biopsy or interventional procedures. 3D-OCT data sets provide comprehensive, volumetric information on architectural morphology. Cross-sectional images with arbitrary orientations, as well as projection and rendered views, can be generated. OCT data is in digital form, facilitating quantitative image processing techniques as well as electronic storage and transmission.

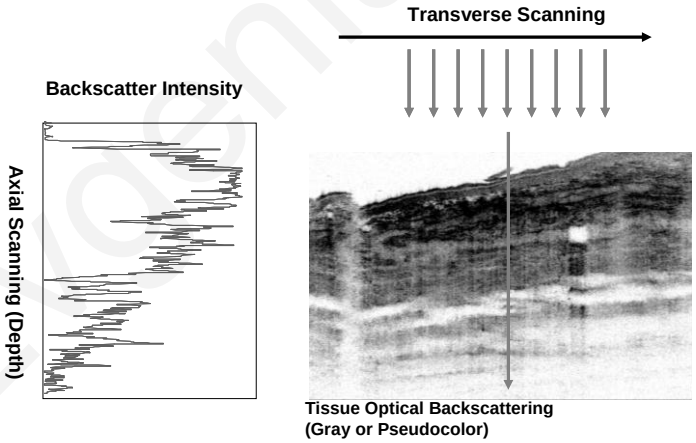

Figure 2.1 Principle of OCT. OCT measures the backscattering intensity as a function of depth. Cross-sectional images are generated by scanning a beam across the tissue. A gray scale or false color image can then be displayed. **[**18]

2.3 Development of OCT:

OCT is a technique for precise measurement of the dimensions of the structures within the tissue ("see through the tissue"), a process similar to object ranging using sonar or radar. The dimensions of structures can be determined by measuring the echo

delay time it takes for a short pulse of sound or electromagnetic wave to be back-reflected from the different structures at various distances.

Ultrasound utilizes this principle to generate depth-resolved measurement of biological tissues (A-mode). The speed of sound in tissue is approximately 1500 m/s, therefore, the measurement of distances with a resolution of 100 μm (typical ultrasound resolution) corresponds to a temporal resolution in the range of 100 ns, which is well within the limits of fast electronic detection. However, ultrasound imaging resolution is not sufficient to reveal the fine biological structures.

Optical methods have the advantage of higher resolution due to the shorter wavelength of light compared to sound. However, the echo delay times associated with light are extremely short. For example, the measurement of a structure with a resolution on the 10 μm scale (typical OCT resolution) will correspond to a temporal resolution in the range of 10 fs given that the speed of light ($3x10^8$ m/s in air) is much faster than sound. Direct electronic detection is not possible on this time scale.

Interferometric detection can measure the backscattered light with high sensitivity and dynamic range. This technique is analogous to coherent optical detection communications. OCT is based on low coherence interferometry, which has been previously applied in photonic devices to perform optical ranging [19][20]. Fig. 2.2 shows a schematic of low coherence interferometry. Measurements are performed using a Michelson interferometer with a low coherence length light source. One arm of the interferometer illuminates the tissue and collects the backscattered light (typically referred to as "sample arm"). The second arm of the interferometer has a reference path delay which is scanned as a function of time (typically referred to as "reference arm"). Optical interference between the light from the sample and reference arms occurs only when the optical delays match to within the coherence length of the light source. Low coherence interferometry enables one-dimensional measurement of the magnitude of backscattered light from internal tissue microstructures versus the delay (and hence the depth) with high accuracy. The first biological application of low coherence interferometry was in ophthalmology for the measurement of eye length [21] . A dual beam interferometer was used to perform the first *in vivo* measurement of axial eye length [22] and high resolution measurements of corneal thickness *in vivo* were also demonstrated using low coherence interferometry [23][24]. Low coherence interferometry has been applied to the precise

biometric measurements of highly scattering biological tissues [25][26]. The successful demonstration of promising biological applications using low coherence interferometry soon triggered the further development of OCT. Two major forms of OCT has been developed independently, namely, time-domain and Fourier-domain OCT.

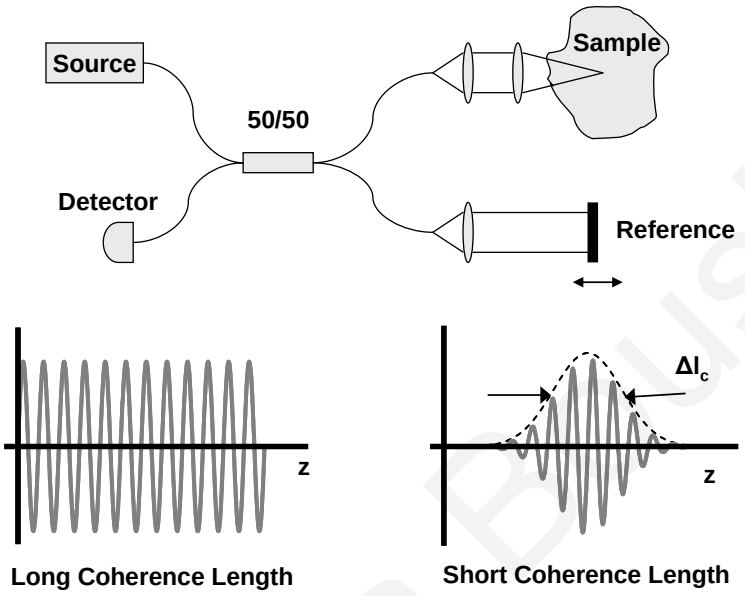

Figure 2.2 Schematic of low coherence interferometry

2.3.1 Time-Domain OCT

The majority of the OCT systems reported between 1991 to 2003 were based on the time-domain detection. In time-domain OCT (TDOCT), the optical depth ranging is achieved by physically scanning the reference arm mirror. The backscattered light coming from the internal tissue structures with optical pathlengths different from the distance selected by the reference mirror (either closer or further) will be rejected by the low coherence gating. TDOCT can achieve >100 dB detection sensitivity and up to several kHz axial scan speed [27][28][29] which enables near-real-time imaging of tissue at a frame rate on the order of 1-10 frames per second.

The growing interest in OCT applications prompted rapid technical development. Important imaging characteristics such as axial (depth) resolution, transverse resolution, imaging speed and detection sensitivity, have improved significantly over time. Axial resolution has also improved greatly during this period to better visualize the internal tissue microstructure. Standard OCT achieves axial image resolution of

10-20 μm using superluminescent diodes (SLDs) [1][3][30] . Using Kerr-lens mode-locked Ti:Sapphire or Cr:Forsterite lasers, axial resolutions around 5μm can be achieved [13][14][31]. Ultrahigh axial resolutions approaching 1-2 μm has been demonstrated [32][33]. The issue of improving the resolution continues to be an active research topic [34][35][36][37][38]. Transverse resolution can be improved by using high numerical aperture (NA) objectives to focus the light to a tighter spot. Typical OCT systems have 10-20 μm transverse resolution which permits sufficient depth of field. Optical coherence microscopy (OCM), which combines confocal microscopy with coherence detection, achieves cellular level transverse resolution [39] . OCM has been applied to *ex vivo* [40] and *in vivo* [41] human tissue imaging.

2.3.2 Fourier-Domain OCT

In 2003, several research groups independently demonstrated that Fourier-domain detection enables a 10-100 fold improvement in detection sensitivity and speed over the time-domain configuration [42][43][44]. These advances not only greatly improve the performance of OCT, but enable three-dimensional OCT (3D-OCT) imaging *in vivo*. 3D-OCT promises to be a powerful advance since three-dimensional comprehensive volumetric data can enable new visualization and processing techniques such as the generation of cross-sectional views with arbitrary orientation, improved quantitative measurements of morphology, and virtual manipulation of tissue geometry for the visualization of morphology.

Fourier-domain detection can achieve very high detection sensitivity. In Fourier or frequency domain detection, the reference mirror position is fixed, and reflections of light are obtained by Fourier transforming the interference spectrum. This technique is analogous to Fourier transform spectroscopy and has a significant sensitivity and speed advantage compared to previous time-domain OCT methods, because it measures the optical echo signals from different depths along the entire A-scan simultaneously rather than sequentially.

Fourier-domain OCT (FDOCT) can be performed using two complementary methods, known as spectral domain OCT (SDOCT) and swept source OCT (SS-OCT), which is also known as optical frequency domain imaging, OFDI). Spectral domain detection uses a spectrometer and a high speed line scan camera to measure the interference spectrum. Although the basic principle of SDOCT has been known

since 1995 [45], limitations in CCD technology and the failure to recognize the performance advantages have delayed the use of this technology for nearly a decade. The first demonstration of *in vivo* retinal imaging using SDOCT was reported in 2002 [46] and high-speed imaging using line-scan CCDs was demonstrated in 2003 [43]. SDOCT was rapidly developed since then and can perform high-speed imaging at 15 kHz - 75 kHz axial scan rates using line-scan CCD cameras [47][48][49][50][51][52], and 70 kHz - 300 kHz axial scan rates using CMOS cameras[53]. SDOCT had a powerful impact on OCT imaging because it enabled ultrahigh resolutions as well as 3D-OCT imaging [54][55][56][57].

In contrast, SS-OCT uses a frequency-swept laser light source and a photo detector to measure the interference spectrum [58][59][47][60]. SS-OCT technology has the advantage of performing imaging at longer wavelengths where CCD performance is limited. Imaging at those wavelengths is important because of reduced optical scattering and improved penetration depths[61]. SS-OCT was first demonstrated in 1997, but performance was poor because of limitations in available laser technologies [58][59]. Recently, advances in frequency swept lasers have enabled high speed imaging with 19 kHz axial scan rates was demonstrated in 2003 [62] and 115 kHz axial scan rates achieved in 2005. Using further advanced laser technology, ultrahigh speed SS-OCT imaging has been recently demonstrated at record imaging speeds of 370 kHz axial scan rates, ~100 times faster than previous TDOCT technology [63][64]. SS-OCT enables three-dimensional OCT imaging of highly scattering tissues that could have a significant impact on disease diagnosis [65][66][67][68].

2.4 OCT Theory

2.4.1 Low Coherence Interferometry

When two light beams combine, their fields are added resulting in a new wave pattern. This phenomenon is known as interference. Low coherence interferometry (LCI), which is the basis of OCT, is the interference between a reference and a sample beam limited by the short coherence length of the light source. This, so-called, “coherence gating” results in high resolution localization of the origin of the interfering beams and can be used for ranging or, in two-dimensions, for imaging of complex scattering samples.

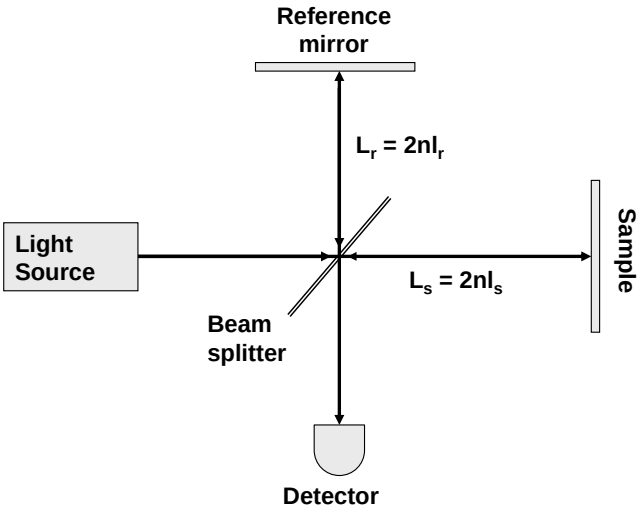

Figure 2.3 Michelson interferometer used for low coherence interferometry.

A simplified schematic of a low coherence Michelson interferometer is shown in Fig. 2.3. In the interferometer, the beam from the light source is directed onto a beam splitter which divides the beam into a reference and a sample, i.e. a measurement, beam. If the sample is a perfectly reflecting mirror and the polarization effects of light are ignored, then the back-reflection of the beam from the sample and the reference mirror can be represented by the complex functions $E_s(t)$ and $E_r(t)$ where

$$E_r(t) = A_r exp\{-i(kL_r - \omega t)\}$$

and

$$E_s(t) = A_s exp\{-i(kL_s - \omega t)\}$$

L_s and L_r are the corresponding optical path lengths of the arms of the interferometer and c is the speed of light. Thus, the resulting light intensity, I_d, at the photodetector is:

$$I_d(t) = \left\langle [E_s(t) + E_r(t+\tau)][E_s(t) + E_r(t+\tau)]^* \right\rangle, \qquad (2)$$

or

$$I_d = \left\langle E_s(t)E_s^*(t) + E_s(t)E_r^*(t+\tau) + E_s^*(t)E_r(t+\tau) + E_r^*(t+\tau)E_r(t+\tau) \right\rangle,$$

where the brackets denote the time averaging over the integration time of the detector, the asterisk indicates the complex conjugate operation and τ is the time delay

corresponding to the round-trip optical path length difference between the two arms and is given by:

$$\tau = \frac{\Delta L}{c} = \frac{L_s - L_r}{c} = \frac{2n(l_s - l_r)}{c}$$

where n is the refractive index of the medium, and ℓs and ℓr are the geometric lengths of the arms. Since the intensities of the sample and reference beams can be represented as

$$I_s = \left\langle E_s(t) E_s^*(t) \right\rangle$$

and

$$I_r = \left\langle E_r(t+\tau) E_r^*(t+\tau) \right\rangle$$

and

$$\left\langle E_s(t) E_r^*(t+\tau) + E_s^*(t) E_r(t+\tau) \right\rangle = 2\,\mathrm{Re}\{\left\langle E_s^*(t) E_r(t+\tau) \right\rangle\}$$

the intensity at the photodetector becomes

$$I_d(\tau) = I_s + I_r + 2Re\left\{\left\langle E_s^*(t) E_r(t+\tau) \right\rangle\right\}$$

or

$$I_d(\tau) = I_s + I_r + 2\sqrt{I_s I_r}\, Re\left\{V_{mc}(\tau)\right\}, \tag{3}$$

where

$$V_{mc}(\tau) = \frac{\left\langle E_s(t) E^*_r(t+\tau) \right\rangle}{\sqrt{I_s I_r}}, \tag{4}$$

The first two components of I_d, I_s and I_r, are the backscattered intensities by the sample and the reference arm, respectively, and the third term is the interference signal. The interference signal carries the information about the structure of the sample, and depends on the optical path delay between the reference and sample arm. The normalized mutual coherence function $V_{mc}(\tau)$ in Eq. 4 is a measure of the degree to which the temporal and spatial characteristics of E_s and E_r match.

If the complex spectral components are ignored, the phase difference, with respect to the optical path delay, can be expressed as $\varphi = 2\pi f_0 \tau$, where f_0 is the center frequency of

the light source. If E_s and E_r originate from a single wave front, spatial coherence can be neglected and the complex mutual coherence function reduces to self-coherence. If a mirror is placed in sample arm [69],[70]. Eq. 3 can be rewritten in the form

$$I_d(\tau) = I_s + I_r + 2\sqrt{I_s I_r}\,Re\{V_{tc}(\tau)\}, \tag{5}$$

where

$$V_{tc}(\tau) = \frac{\langle E(t)E^*(t+\tau)\rangle}{\sqrt{I_s I_r}}.$$

If V_{tc} is expressed as

$$V_{tc}(\tau) = A(t)e^{i2\pi f_0 \tau}$$

then

$$Re\{V_{tc}(\tau)\} = A(\tau)\cos(2\pi f_0 \tau) = |V_{tc}|\cos(2\pi f_0 \tau)$$

which finally results in

$$I_d(\tau) = I_s + I_r + 2\sqrt{I_s I_r}\,|V_{tc}(\tau)|\cos(2\pi f_0 \tau). \tag{6}$$

The Wiener–Khinchin theorem (also known as the Wiener–Khinchin–Einstein theorem or the Khinchin–Kolmogorov theorem) states that the power spectral density of a wide-sense-stationary random process is the Fourier transform of the corresponding autocorrelation function, i.e.

$$S_{xx}(f) = \int_{-\infty}^{\infty} r_{xx}(\tau)e^{-j2\pi f\tau}\,d\tau$$

where

$$r_{xx}(\tau) = E[\,x(t)x^*(t-\tau)\,]$$

is the autocorrelation function. According to the Wiener- Khinchin theorem, the temporal coherence function V_{tc} is actually the Fourier transform of the power spectral density $S(f)$ of the light source, which is fully characterized by its shape, its spectral bandwidth, and its center wavelength [20],[70],[71],[72].

$$V_{tc}(\tau) = I\{S(f)\} = \int_{0}^{\infty} S(f)\exp(-j2\pi f\tau)df\,. \tag{7}$$

This relationship reveals that the shape and width of the emission spectrum of the light source are important variables since they influence the resolution of the low coherence interferometer.

Eq. 6 can be rewritten so that I_d is presented as a function of ΔL based on

$$2\pi f_0 \tau = 2\pi \frac{c}{\lambda_0}\tau = \frac{2\pi \Delta L}{\lambda_0} = k_0 \Delta L$$

$$k_0 = \frac{2\pi}{\lambda_0}, f_0 = \frac{c}{\lambda_0}, c\tau = \Delta L.$$

resulting in

$$I_d(\Delta L) = I_s + I_r + 2\sqrt{I_s I_r}\left|\Im\{S(k)\}\right|\cos(k_0 \Delta L) \tag{8}$$

where $k_0=2\pi/\lambda_0$ is the average wave number and the relation $\lambda_0=c/f_0$ is used to transform from the time domain to the path domain [69],[70].

So far, including Eq. 8, it was assumed that the sample is a perfectly reflecting mirror, that does not affect the amplitude and coherence of the sample beam, but induces only a time delay. In reality, the light reflected from the sample is composed of single or least scattered light and diffuse or multiply scattered light. In contrast to diffuse backscattered light, the light that undergoes only single scattering or very little scattering maintains its coherence and contributes to the LCI signal. Taking into account the scattering path inside the media, the total round-trip path length L_s of the sample arm is

$$L_s = L_{so} + L_s' \tag{9}$$

where L_{so} is the round-trip path length to the sample surface and L_s' is the total round-trip path length inside the sample to the scatterer site.

2.4.2 OCT Signal from Multiple Scatterers

Any given sample can be expressed as a series of scatterers, i.e.

$$L_s' = \sum n_s l_i \tag{10}$$

where n_s is the refractive index of each layer of the medium and ℓ_i the scattering path of light inside the medium. In such a case, the intensity given in Eq. 2 can be written in the form

$$I_d(\tau) = \left\langle [\int_{L_{s0}}^{¥} E'_s(t,L_s)dL_s + E_r(t+\tau)][\int_{L_{s0}}^{¥} E'_s(t,L_s)dL_s + E_r(t+\tau)]^* \right\rangle \quad (11)$$

where $E'(t,L_s)$ is the path length-resolved field density. Eq. 11 yields

$$I_d(L_s,L_r) = I_s + I_r + 2Re\int_{L_{SO}}^{+¥} \left\langle E_s'(t,L_s)dL_s E_r(t+\tau) \right\rangle$$

Since

$$E'_s(t,L_s) = E_s(t)^* R(L_s) = E_r(t)R(L_s)$$

then

$$I_d(L_s,L_r) = I_s + I_r + 2\sqrt{I_s I_r}\int_{-¥}^{+¥} \sqrt{R(L_s)}\,Re\{V_{tc}(\Delta L)\}dL_s \quad (12)$$

or

$$I_d(L_s,L_r) = I_s + I_r + 2\sqrt{I_s I_r}\int_{-¥}^{+¥} \sqrt{R(L_s)}\,|V_{tc}(\Delta L)|\cos(k_0\Delta L)dL_s \quad (13)$$

where $R(L_s)$ is the normalized path length-resolved diffuse reflectance, i.e. the normalized derivative of the intensity depth distribution of the sample wave, representing the fraction of power reflected from the layer located at position L_s within the object.

The signal-carrying interference term, i.e. the interference modulation, in Eq. 12 can also be expressed as a convolution

$$I_{signal}(L_s,L_r) = 2\sqrt{I_s I_r}\left[\sqrt{R(L_s)}\ Ä\ Re\{V_{tc}(\Delta L)\}\right] \quad (14)$$

$$Re\{V_{tc}(\Delta L)\} = \frac{\langle E(L_s)^* E^*(L_s - L_r)\rangle}{\sqrt{I_s I_r}}$$

where $Re\{V_{tc}(\Delta L)\}$ is the coherence function, i.e. the interferometric response in the ideal case of a mirror in both arms and ⊗ denotes the convolution operation. The function $Re\{V_{tc}(\Delta L)\}$ is also called the point spread function (PSF) of the system, since it defines the resolution of OCT, and is a function of the properties of the light source [69][73][70][74].

In order to examine the spectral equivalent of Eq. 13, let r_{ii} describe the source autocorrelation, i.e.

$$r_{ii}(\Delta L) = \left\langle E_{source}(L_s)E^*_{source}(L_s + L_r)\right\rangle .$$

The cross-correlation function for an arbitrary specimen in the sample arm of the interferometer is

$$r_{is}(\Delta L) = \left\langle E_s(L_s)E^*_i(L_s - L_r)\right\rangle$$

and is equal to

$$r_{is}(\Delta L) = \sqrt{R(L_s)}\ \text{Ä}\ [r_{ii}(\Delta L)] .$$

Using the correlation terms, Eq. 14 can be re-written as

$$I_d(L_s, L_r) = I_s + I_r + 2\left[r_{is}(\Delta L)\right]. \quad (15)$$

Finally, the corresponding spectral relations can be obtained using the Wiener-Khinchin theorem. First, the power spectrum of the light source is obtained as the Fourier transform of its autocorrelation, i.e.

$$S(k) = I\left\{(r_{ii}(\Delta L)\right\} \quad (16)$$

Furthermore, the cross spectral density function of two waves is obtained as the Fourier transform of the cross-correlation function as

$$S_{is}(k) = I\left\{r_{is}(\Delta L)\right\} \quad (17)$$

The following spectral interference law is obtained from Eq. 15:

$$I(k) = S_i(k) + S_s(k) + 2Re\left\{S_{is}(k)\right\}$$

(18)

2.4.3 Time Domain Optical Coherence Tomography (TD OCT)

The term *tomography* is used whenever two-dimensional data is derived from a three-dimensional object to construct a slice image of the object's internal structure. In OCT, multiple parallel LCI scans are performed to generate the two-dimensional

image. A typical measurement system consists of a Michelson interferometer illuminated by a low temporal coherence light source, such as a superluminescent diode or a broad bandwidth laser. In OCT, the object to be measured is placed in one arm of the interferometer. A measurement beam emitted by the light source is reflected or backscattered from the object with different delay times, depending on the various optical properties of the different layers within the object. A longitudinal profile of reflectivity versus depth is obtained by translating the reference mirror, or by other means changing the pathlength of the reference arm, and synchronously recording the magnitude of the intensity of the resulting interference fringes. A fringe signal is evident at the detector only when the optical path difference in the interferometer is less than the coherence length of the light source. Locating the maximum fringe visibility position allows one to determine the location of internal structures of the object with a resolution on the micrometer scale [30]. A simple TDOCT system with the interference signal and the A-Scan envelope is shown in Fig. 2.4.

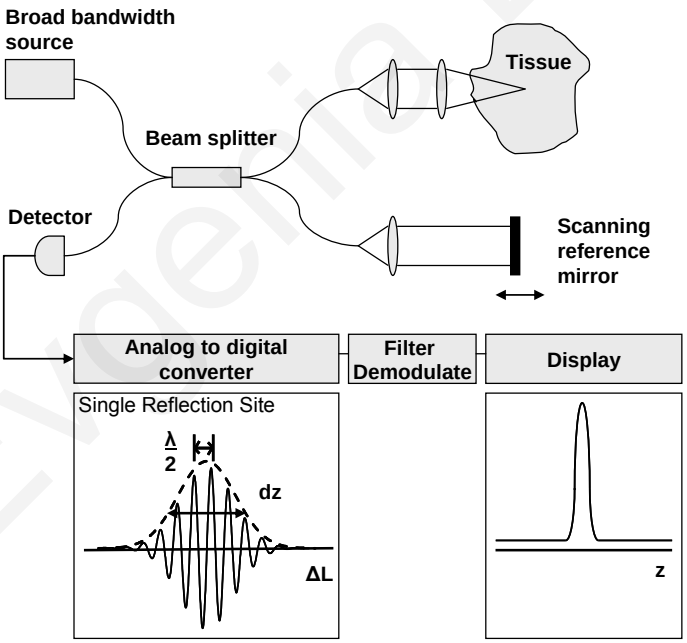

Figure 2.4 Typical fiber-optic implementation of time domain OCT system, interferogram and the A-Scan envelope.

Modulation of the optical delay between the arms, for example by translating the reference mirror at a constant speed, shifts the interference signal to the corresponding Doppler frequency defined by

$$f_d = \frac{2v}{\lambda_0}$$

where v is the speed of the moving mirror and λ_0 is the center wavelength of the light source. Shifting to the Doppler frequency facilitates the removal of the dc background components and other low-frequency noise during demodulation. To extract the signal carrying component, the detection circuit usually contains three main components: (1) a trans-impedance amplifier, (2) a band-pass filter centered at f_d, and (3) an amplitude demodulator to extract the envelope of the interferometric signal

2.4.4 Fourier Domain Optical Coherence Tomography

The basis of Fourier domain OCT (FDOCT) is evident in Eq. 17. In contrast to TD OCT, depth information in FDOCT is provided by an inverse Fourier transform of the spectrum of the backscattered light. The amplitude of the spectrum of the backscattered sample light *I(k),* is obtained using a spectrometer. The inverse Fourier transform of the recorded spectral intensity yields the same line scan signal as obtained by standard low coherence interferometry and provides a backreflection profile as a function of depth.

A simplified optical setup of an FD OCT interferometer is shown in Fig. 2.5. The broadband source used is similar to TD OCT. In contrast to time domain techniques, the time-consuming mechanical OCT depth scan is replaced by a spectral measurement. FD OCT measures the signal in the Fourier domain and, by Fourier transformation, delivers the scattering profile in the spatial domain. The interference spectrum *I(k*) for a single scatterer at a distance z_1 from the reference plane is a cosine function multiplied by the spectrum of the source, *S(k).* The Fourier transform provides the location of the peak at that frequency which corresponds to the scatterer location. The backscattering profile of a complicated, real, sample is the sum of many such signals.

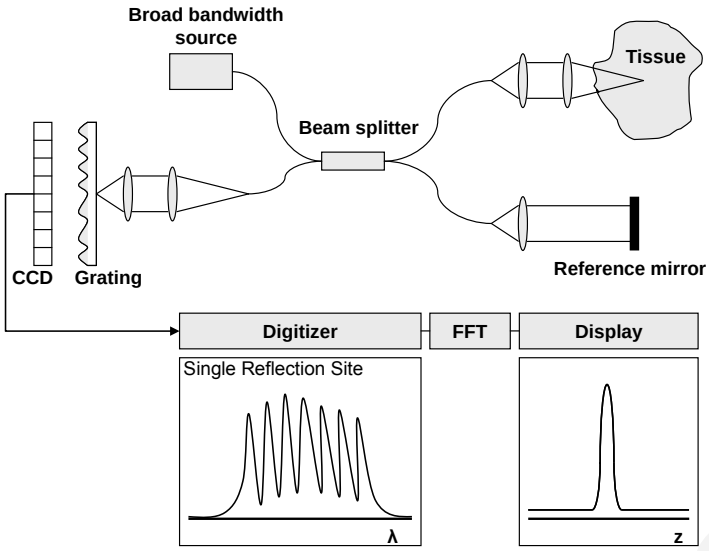

Figure 2.5 Typical fiber-optic implementation of Fourier Domain OCT, spectrogram, backreflection profile.

Analytically, the signal in the sample arm, backscattered from different depths within the sample, is combined with the signal in the reference arm to produce an interferogram. The total interference signal is given by the spectral intensity distribution of the light source multiplied by the square of the sum of the backreflected reference and sample signals:

$$I(k) = S(k)\left|a_R exp(j2kr) + \int_0^{\infty} a(z)exp(j2k(r + n(z).z)dz\right|^2 \qquad (19)$$

k: wavenumber $k=2\pi/\lambda$

r: path length in the reference arm

r +z: path length in the object arm

z: path length in the object arm, measured from the reference plane

n: refractive index (n = 1 for $z < z_0$ and varying depending on the sample for longitudinal positions in the object $z > z_0$)

a_R*:* reflection coefficient of the reference

a(z): backscattering coefficient of the object signal

S(k): spectral intensity distribution of the light source

Assuming a_R=1, the interference signal *I(k)* can be written as:

$$I(k) = S(k)\left|1 + \int_0^{\infty} a(z)exp(j2knz)dz\right|^2 \tag{20}$$

Expanding the complex exponential results in

$$I(k) = S(k)\left|1 + \int_0^{\infty} a(z)cos(2knz)dz + j\int_0^{\infty} a(z)sin(2knz)dz\right|^2$$

The absolute value of a complex three-term can be evaluated by multiplying with the complex conjugate term

$$I(k) = S(k)\left(\left(1 + \int_0^{\infty} a(z)cos(2knz)dz\right) + j\int_0^{\infty} a(z)sin(2knz)dz\right)\left(\left(1 + \int_0^{\infty} a(z)cos(2knz)dz\right) - j\int_0^{\infty} a(z)sin(2knz)dz\right)$$

The result is

$$I(k) = S(k)\left(\left(1 + \int_0^{\infty} a(z)cos(2knz)dz\right)^2 - \left(j\int_0^{\infty} a(z)sin(2knz)dz\right)^2\right)$$

$$I(k) = S(k)\left(1 + 2\int_0^{\infty} a(z)cos(2knz)dz + \underbrace{\left(\int_0^{\infty} a(z)cos(2knz)dz\right)^2 - \left(j\int_0^{\infty} a(z)sin(2knz)dz\right)^2}_{\left|\int_0^{\infty} a(z)exp(j2kz)dz\right|^2}\right)$$

Substituting

$$\left|\int_0^{\infty} a(z)exp(j2kz)dz\right|^2 = \left(\int_0^{\infty} a(z)exp(-j2kz)dz\right)\left(\int_0^{\infty} a(z')exp(j2kz')dz'\right) = \int_0^{\infty}\int_0^{\infty} a(z)a(z')exp(-j2kz)exp(j2kz')dzdz'$$

in the above equation results in an interference signal of the form

$$I(k) = S(k)\left(1 + 2\int_0^{\infty} a(z)cos(2knz)dz + \int_0^{\infty}\int_0^{\infty} a(z)a(z')e^{-j2kn(z-z')}dzdz'\right) \tag{21}$$

Therefore, the interference signal is a sum of three terms. The first is a DC term. The second term encodes the depth information of the object. The backreflection intensity is incorporated in *a(z)*, while the corresponding optical pathlength difference is found in the argument of the cosine term. The third term describes the mutual interference of

all elementary waves. Assuming that *a(z)* is symmetrical with respect to *z* suggests that *a(z)* can be replaced by the symmetrical expansion $\hat{a}(z) = a(z) + a(-z)$ and, therefore,

$$I(k) = S(k)\left(1 + \int_0^{\infty} a(z)\cos(2knz)dz + \int_0^{\infty} a(z)\cos(2knz)dz + \frac{1}{2}\int_0^{\infty}\frac{1}{2}\int_0^{\infty} a(z)a(z')e^{-j2kn(z-z')}dzdz' + \frac{1}{2}\int_0^{\infty}\frac{1}{2}\int_0^{\infty} a(z)a(z')e^{-j2kn(z-z')}dzdz' \right)$$

$$I(k) = S(k)\left(1 + \int_0^{\infty} a(z)\cos(2knz)dz + \int_{-\infty}^{0} a(-z)\cos(2knz)dz + \frac{1}{2}\int_0^{\infty}\frac{1}{2}\int_0^{\infty} a(z)a(z')e^{-j2kn(z-z')}dzdz' + \frac{1}{2}\int_{-\infty}^{0}\frac{1}{2}\int_{-\infty}^{0} a(-z)a(-z')e^{-j2kn(z-z')}dzdz' \right)$$

$$I(k) = S(k)\left(1 + \int_{-\infty}^{\infty} \hat{a}(z)\cos(2knz)dz + \frac{1}{4}\int_{-\infty}^{\infty}\int_{-\infty}^{\infty} \hat{a}(z)\hat{a}(z')e^{-j2kn(z-z')}dzdz' \right)$$

Expanding the second term in complex exponentials and sum using again, the symmetrical properties of *a(z)* results in

$$\int_{-\infty}^{\infty} \hat{a}(z)\cos(2knz)dz = \int_{-\infty}^{\infty} \hat{a}(z)\left(\frac{e^{j2knz} + e^{-j2knz}}{2} \right)dz$$

$$= \frac{1}{2}\int_{-\infty}^{\infty} \hat{a}(z)e^{j2knz}dz + \frac{1}{2}\int_{-\infty}^{\infty} \hat{a}(z)e^{-j2knz}dz$$

$$= \frac{1}{2}\int_{-\infty}^{\infty} \hat{a}(-z)e^{-j2knz}dz + \frac{1}{2}\int_{-\infty}^{\infty} \hat{a}(z)e^{-j2knz}dz$$

$$= \int_{-\infty}^{\infty} \hat{a}(z)e^{-j2knz}dz$$

Since the amplitude is real, the third term can be re-formed as a function of the autocorrelation term

$$AC[\hat{a}(z)] = \int_{-\infty}^{\infty} \hat{a}(z)\hat{a}^*(z_0 + z')dz$$

resulting in

$$\frac{1}{4}\int_{-\infty}^{\infty}\int_{-\infty}^{\infty}\hat{a}(z)\hat{a}(z')e^{-j2k\pi(z-z')}dzdz'$$

$$=\frac{1}{4}\int_{-\infty}^{\infty}\int_{-\infty}^{\infty}\hat{a}(z)\hat{a}(z+z'')e^{-j2k\pi(z)}e^{j2k\pi(z_0+z'')}dzdz''$$

$$=\frac{1}{4}\int_{-\infty}^{\infty}e^{-j2k\pi(z)}dz\underbrace{\int_{-\infty}^{\infty}\hat{a}(z)e^{j2k\pi(z_0)}\hat{a}(z+z'')e^{j2k\pi(z'')}dz''}_{AC[\hat{a}(z)]}$$

$$=\frac{1}{4}\int_{-\infty}^{\infty}AC[\hat{a}(z)]e^{-j2k\pi(z)}dz$$

where $z'=z_0+z''$ (with z_0 an offset constant) and $dz'=dz''$. Incorporating the above results, the intensity of the spectral interferometric signal becomes

$$I(k)=S(k)\left(1+\int_{-\infty}^{\infty}\hat{a}(z)e^{-j2knz}dz+\frac{1}{4}\int_{-\infty}^{\infty}AC[\hat{a}(z)]e^{-j2k\pi(z)}dz\right)$$

The second and the third terms are actually Fourier transforms of the scattering amplitude $\hat{a}(z)$ and of the autocorrelation term $AC[\hat{a}(z)]$ over the variable z. By using the Fourier transform scaling property the interferogram can be re-written as

$$I(k)=S(k)\left(1+\int_{-\infty}^{\infty}\hat{a}(z)e^{-jknz\ \overset{time\ scale}{(2)}}dz+\frac{1}{4}\int_{-\infty}^{\infty}AC[\hat{a}(z)]e^{-jknz\ \overset{time\ scale}{(2)}}dz\right)$$

$$I(k)=S(k)\left(1+\frac{1}{2}I_z\left\{\hat{a}(z)\right\}+\frac{1}{8}I_z\left\{AC\left[\hat{a}(z)\right]\right\}\right)$$

Performing the inverse Fourier transformation generates the following relationship

$$F^{-1}\left\{I(k)\right\}=F^{-1}\left\{S(k)\right\}\ \ddot{A}\left(\left[\delta(z)\right]+\frac{1}{2}\hat{a}(z)+\frac{1}{8}AC\left[\hat{a}(z)\right]\right)$$
$$=\quad A\quad\ddot{A}(\quad B\quad+\quad C\quad+\quad D\quad) \tag{22}$$

where $\otimes$ denotes convolution. The signal C is the symmetrical scattering amplitude $\hat{a}(z)$ and therefore the strength of the scattering versus the depth of the sample.

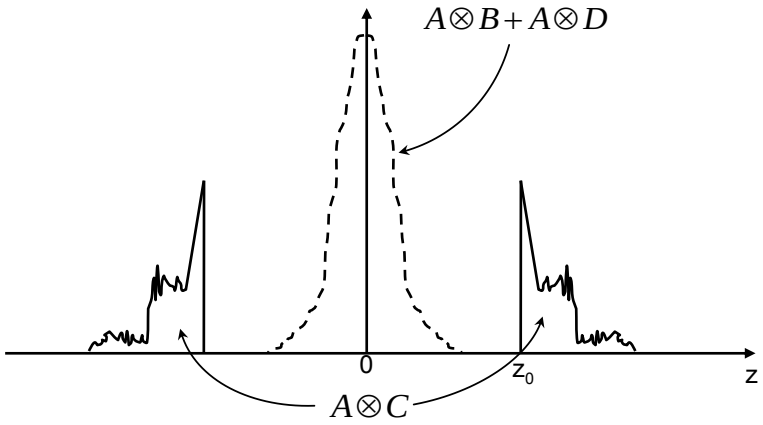

Figure 2.6 Amplitude of the results of the Fourier transform of the spectral interferogram recorded with FD OCT.

The first convolution $A\otimes B$ is the Fourier transformation of the source spectrum (correlogram) located around $z = 0$. It can be separated from the information-carrying signal by shortening the optical pathlength in the reference arm, compared to the sample arm, thus increasing the frequency separation between the terms (Fig. 2.6). $A\otimes D$ designates the autocorrelation terms, which describe the mutual interference of all scattered elementary waves. In strongly scattering media, such as skin, the influence of *D* can be neglected because the autocorrelation term is much weaker than the signal term, which is weighted by the strong reference amplitude. Moreover, these terms are also located around z = 0. Therefore, the autocorrelation term can also be separated from the object signal *a(z)* with a small offset z_0 (Fig. 2.6). However, if the object exhibits high backscattering from large depths, there is still the possibility for the $A\otimes D$ term to interfere with the object signal. High backscattering deep within tissue can lead to overlap of the terms which can, in turn, result in artifacts in the data. A solution is to perform, at each position, a second measurement with no reference signal and subtract that signal from *I(k)*. Also in Eq. 22 the signal *C* is convolved with the correlogram of the source. To achieve high resolution measurements, a light source with a sufficiently broad and smooth spectrum, without noise and ripple, must be selected so that the resulting convoluted peaks from individual scatterers will be sufficiently narrow.

2.4.5 Wavelength Tuning (Swept Source) OCT

In wavelength tuning or swept source OCT (SS-OCT) the wavelength-dependent intensity data are not recorded simultaneously by using a broadband light source and

a spectrometer. Instead, they are recorded sequentially, with a single photodetector, at the detector side, while tuning the wavelength of the light source. If the wavelength λ of the tunable laser in Fig. 2.7 is constant, the intensity at the photodetector can be calculated as [75]

$$I = I_s + I_r + 2\sqrt{I_s I_r}\cos(2\pi\Delta\Phi) \tag{23}$$

where I_s and I_r are the light intensities reflected from the sample and reference, respectively. $\Delta\Phi$ is the phase difference between the two beams,

$$\Delta\Phi = 2\frac{L}{\lambda} = 2L\frac{k}{2\pi} \tag{24}$$

where k is the wavenumber corresponding to λ. If the wavenumber is changed, the phase difference changes accordingly. This causes the intensity at the photodetector to oscillate with a frequency

$$f = \frac{d\Delta\Phi}{dt} = \frac{d\Delta\Phi}{dk}\frac{dk}{dt} = \frac{L}{\pi}\frac{dk}{dt} \tag{25}$$

Hence, the frequency is directly proportional to the tuning rate of the wavenumber dk/dt and to the path difference, L. If dk/dt is constant, L can be obtained by a Fourier transform of the time-dependent intensity signal recorded by the photodetector during tuning. Fourier transforming the time depended beat signal yields the sample depth structure, i.e. the magnitude of the beat signal defines the amplitude reflectance and the beat frequency defines the depth position of light scattering sites in the sample.

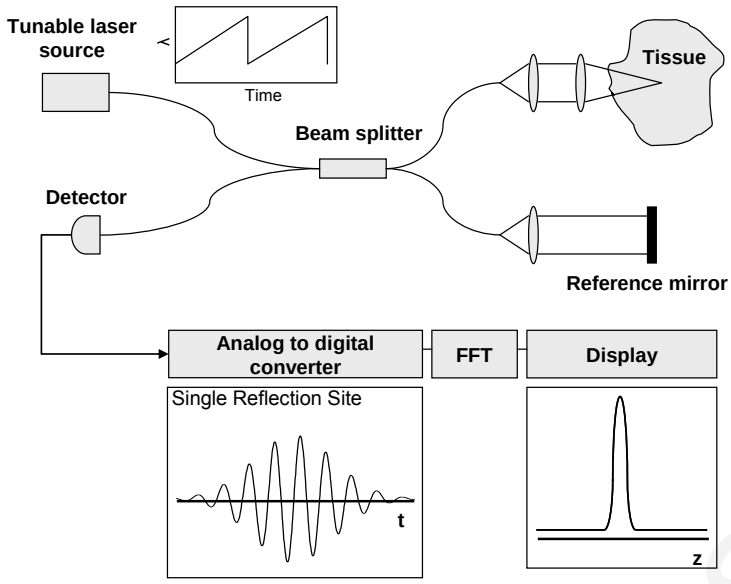

Figure 2.7 Typical fiber-optic implementation of Swept Source OCT, interferogram, and backreflection profile.

As in the case of FD OCT, the main advantage of this technique, compared to standard OCT techniques, is that the reference arm length is fixed and no moving parts are required. This significantly increases the speed of scanning. The use of a single photodetector provides the added advantage of simple elimination of the unwanted dc intensity terms by high-pass filtering of the photodetector signal or heterodyne detection. This enhances the usable dynamic range of the detection system considerably. Compared to FD OCT, SS OCT offers similar high data acquisition speed but without the drawbacks of the spectral limitations of the CCD camera. The price currently to be paid is that the light sources are expensive and so far only available for a limited range of wavelengths. However, it is expected that these limitations will be overcome in the near future.

2.4.6 Spatial Resolution in Optical Coherence Tomography

2.4.6.1 Axial Resolution

The axial resolution in OCT is determined by the coherence length of the light source, implying that high axial resolution can be achieved independently of the beam-focusing conditions. The coherence length is the spatial width of the field autocorrelation produced by the interferometer. As shown above, the envelope of the field autocorrelation is the Fourier transform of the power spectrum. Thus, the width of the autocorrelation function, or the axial resolution, is inversely proportional to the

width of the power spectrum. Therefore, for a source with a Gaussian spectral distribution, the axial resolution, Δz, is

$$\Delta z = \frac{2\ln 2\lambda_0^{\,2}}{\pi\Delta\lambda} \tag{26}$$

where $\Delta\lambda$ is the full width at half maximum (FWHM) wavelength range of the light source [76]. Eq. 26 is valid only in a vacuum. In the more common case where the sample is dispersive, the refractive index of the sample material depends on the wavelength and affects the system's resolution. This effect is particularly significant when broad-band sources are used. Distances measured with LCI are optical distances. The geometric equivalent is derived by dividing the optical distance by the group refractive index n_g of the media. In real materials, not only is the refractive index n a function of wavelength, but also the group index n_g:

$$n_g = n - \lambda\frac{dn}{d\lambda} \tag{27}$$

This dispersion effect, when different in the two arms of the interferometer, results in a broadening of the interferogram and an increase in coherence length which, in turn, translates into a deterioration in resolution. In a dispersive medium, the coherence length Δz_m can be calculated by

$$\Delta z_m = \sqrt{\Delta z^2 + (\frac{dn_g}{d\lambda} d_g \Delta\lambda)^2} \tag{28}$$

where d_g is the geometric depth in the medium [77],[78].

2.4.6.2 Transverse Resolution

The transverse resolution of an OCT system is determined by the optics of the imaging device and does not depend on the axial resolution. The selection of optics is a tradeoff between the transverse resolution and the imaging depth range, i.e. the depth of focus. The transverse resolution Δx can be approximated by

$$\Delta x = \frac{4\lambda}{\pi}\left(\frac{f_1}{d}\right) = \frac{4\lambda}{\pi NA} \tag{29}$$

where f_1 is the focal length of the focusing lens, d is the light beam diameter on the lens aperture, and NA is the numerical aperture of the lens. High transverse resolution

can be obtained by using a large *NA* and focusing the beam to a small spot size. The transverse resolution is also related to the Rayleigh range, z_r, which is a measure of the depth of focus, i.e.

$$z_r = \frac{\pi \Delta x^2}{4\lambda}$$

(30)

The Rayleigh range is the distance from the focal plane to the point where the light beam diameter has increased by a factor of $\sqrt{2}$. Given the above relationships, it is obvious that improving the transverse resolution produces a decrease in the depth of focus, a significant trade-off in the design of OCT imaging devices.

2.4.7 Axial Range Limitations

In TDOCT the axial range is defined by the mechanical scanning range of the optical delay-line. However the axial range in SDOCT is limited by two mechanisms which do not affect TDOCT systems. The first mechanism that limits the imaging depth is the spectral sampling interval. The spectral sampling interval determines the maximum observable depth. A large difference between the object and reference optical paths results in a high frequency interferogram in the spectral domain. According to the sampling theorem, the sampling frequency must be at least twice as large as the highest occurring frequency in the spectrum. The interference spectrum *I(k)* for a mirror at a distance z_1 from the reference plane contains the cosine function $a(z)\cos(2knz_1)$ multiplied by *S(k)*. For $z = z_{max}$, the period of the cosine fringes becomes

$$dk = \frac{\pi}{nz_{\max}}$$

Therefore the spectral sampling interval must be $\delta_{sk}=dk/2$, and the maximum depth is given by:

$$z_{\max} = \frac{\pi}{2n\delta_{sk}}$$

(31)

From the relation

$$k = \frac{2\pi}{\lambda} \Rightarrow dk = \frac{2\pi(d\lambda)}{\lambda^2}$$

the maximum resolvable depth is also given by

$$Z_{\max} = \frac{{\lambda_0}^2}{4n(\delta_{s\lambda})}. \tag{32}$$

where $\delta_{s\lambda}$ denotes the wavelength sampling interval defined by the detector separation of a linear detector array in a FDOCT system. Generally if M is the number of samples in the spectral interferogram then $\delta_{sk} = \frac{\Delta k}{M}$, and $\delta_{s\lambda} = \frac{\Delta\lambda}{M}$, where Δk and Δλ are the total wavenumber range and the total wavelength range of the source respectively. By substituting these relations into Eq. 31 and Eq. 32, we have:

$$z_{\max} = \frac{\pi}{2n\Delta k} M \tag{33}$$

and

$$z_{\max} = \frac{{\lambda_0}^2}{4n(\Delta\lambda)} \mathrm{M} \tag{34}$$

From Eq. 33, and 34, we can see that for a given source bandwidth the axial scan range is limited by the number of samples.

A second parameter that limits the imaging depths in SDOCT systems, is the limited spectral resolution. In SDOCT the spectral resolution is defined by the spectral resolution of the spectrometer, while in SSOCT the spectral resolution is limited by the shape of the instantaneous linewidth of the swept source. The effect of the finite spectral resolution can be interpreted as the convolution of the spectral interferogram with a Gaussian function which has a half maximum width equal to the spectral resolution. By performing the Fourier transform of the spectral interferogram to obtain the A-scan data, the convolution operator converts to multiplication. This means that the A-scan data is multiplied with a function whose shape is given by the Fourier transform of the Gaussian function which is also Gaussian. This function reduces the intensity of the signal as a function of depth even if the reflectivity remains constant, a phenomenon which is known as sensitivity roll-off. This roll-off

can be characterized as the one sided depth, at which the sensitivity drops by one half, or by 6dB, and is given by [79]:

$$z_{6dB} = \frac{2\ln(2)}{\delta_{rk}} = \frac{\ln(2)}{\pi}\frac{\lambda_0^2}{\delta_{r\lambda}}$$

where δ_{rk} and $\delta_{r\lambda}$ are the spectral resolutions in wavenumber and wavelength units respectively.

In addition, other components of the OCT system, such as the grating and focusing optics in particular, can contribute to the roll-off. Aberrations and diffraction, which degrade the wavelength resolution, result in signal decay. Another limitation of Fourier domain imaging comes from the fact that the spectral interferogram is a real function and the DFT of a real function is an even function. This means that each signal peak in the positive frequency range will have a mirror image in the negative frequency range. Any signal that exceeds the maximum axial range, will appear as an aliased signal.

2.5 Clinical Applications of OCT

Several features of OCT point to its potential to become a very powerful imaging technology for the diagnosis of a wide range of pathologies.

1. OCT can image with axial resolutions of 1-10 μm, one to two orders of magnitude higher than competing technologies such as conventional ultrasound. This resolution approaches that of histopathology, allowing architectural morphology as well as cellular features to be resolved. Unlike ultrasound, imaging can be performed directly through air without requiring direct contact with the tissue or a transducing medium.

2. Imaging can be performed *in situ*, without the need to excise a specimen. This enables imaging of structures in which biopsy would be hazardous or impossible. It also allows better tissue or organ area coverage, reducing the sampling errors associated with excisional biopsy.

3. Imaging can be performed in real time, without the need to process a specimen as in conventional biopsy and histopathology. This allows pathology to be monitored on screen and stored in high resolution. Real time imaging can

enable real time diagnosis, and coupling this information with surgery, can enable surgical guidance.

4. OCT is fiber-optically based, and therefore can be interfaced to a wide range of instruments including catheters, endoscopes, laparoscopes, and surgical probes. This enables access to a wide range of internal organ systems.

5. Finally, OCT is compact and portable, which is an important feature for a clinically viable device.

There are three general application scenarios that are envisioned for OCT in the diagnosis of disease. First, OCT can enable guiding standard excisional biopsy to reduce sampling errors and false negative results. This can improve the accuracy of biopsy as well as reduce the number of biopsies that are taken, resulting in better prognosis as well as significant cost savings. Second, after more extensive clinical studies have been performed, it may be possible to use OCT to directly diagnose or grade disease. This application will be more challenging since it implies making a diagnosis on the basis of OCT rather than conventional pathology. Applications include situations where OCT might be used to grade early neoplastic changes or determine the depth of neoplastic invasion. Third, there may be scenarios where diagnosis and treatment are performed in real time based on OCT imaging. This would require the OCT diagnostic information to be directly and immediately coupled to treatment decisions. The integration of diagnosis and treatment could reduce the number of patient visits, yielding a significant reduction in health care costs and improve patient compliance. Each of these scenarios requires a different level of OCT performance not only in its ability to image tissue pathology, but to achieve the required level of sensitivity and specificity for each clinical situation. The most developed clinical OCT applications are those focusing on ophthalmic, cardiovascular, and gastrointestinal imaging.

2.6 Conclusions

OCT can perform a type of optical biopsy, i.e. imaging of tissue morphology the micron-scale, *in situ*, and in real time. Image information is available immediately without the need for excision and histologic processing of a specimen. The development of high-resolution and high-speed OCT technology, as well as OCT compatible catheter/endoscopes and other delivery devices, represent enabling steps

for many, future, OCT imaging clinical applications. More research remains to be done and numerous clinical studies must be performed to determine in which clinical situations OCT can play a role. However, the unique capabilities of OCT imaging suggest that it has the potential to significantly impact the diagnosis and clinical management of many diseases and improve patient prognosis. In addition, OCT can be a powerful research tool for applications in many areas, including developmental biology, where non-destructive, serial imaging, on the same samples can offer new insights and significant cost and time advantages.

Chapter 3
Swept Source OCT System Implementation

3.1 Summary

This chapter describes the development of the swept source OCT system used throughout this thesis. First, the implementation of the system will be described and system characterization will follow. The construction of the system consists of hardware implementation and data acquisition. In addition post processing procedures which are necessary for swept source OCT signals will be described.

3.2 System Implementation

The diagram of a swept source OCT (SS-OCT) setup is shown in Fig. 3.1. The swept light source (center wavelength 1310 nm, scan range 110 nm, 20-kHz scan rate, Santec Corporation HSL 2000, Komaki, Aichi, Japan) output power is 10 mW. The beam from the source is split by a beam splitter designed for infrared light (Newport benchtop coupler WDM, 90/10, Model F-CPL-L22131-A, 1310nm). The 90/10 coupler splits the output power. 90% of the output power was coupled into the sample arm and the remaining 10% into the reference arm. Two circulators are used in both the reference and sample arms to redirect the back- reflected light to a 2×2 fiber coupler (50/50 split ratio Newport F-CPL-F22135 1300nm) for detection.

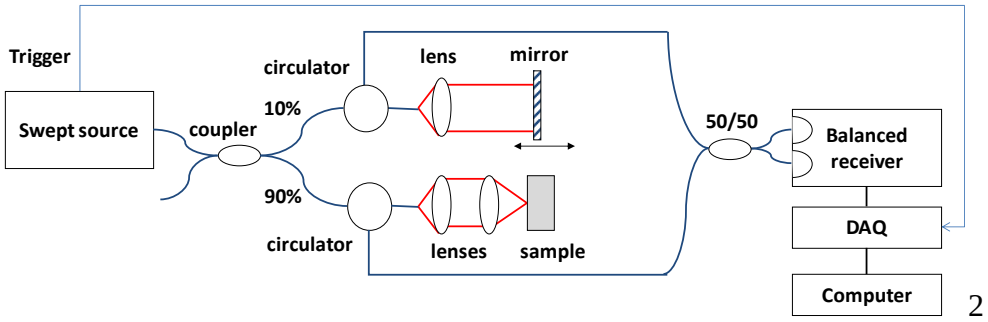

Figure 3.1 SSOCT configuration setup

Non-contact receptacle style collimators for singlemode fiber, which use an f=11mm aspheric lens and are optimized for 1300nm to 1550nm wavelengths, (OZ Optics,HPUCO -23A-1300/1550-S-11AS-SP), and an achromatic doublet lens in the sample arm, (Thorlabs,AC254-030-C,D=25.4, f=30.0mm, and f_b=22mm) are used for focusing. The reference arm is held constant. The sample arm contains a scanner for transverse scanning of the sample. Scanning is performed by a galvanometer (Cambridge Technology Inc, Moving Magnet Capacitive Position Detector Optical Scanner,Model 6230). The galvanometer is controlled by a servo driver (Cambridge Technology Inc, MicroMax 671 Driver Board), which provides excellent positioning repeatability, accuracy and stability in a compact single axis configuration. The reflected signals are directed to the detection arm to produce an interferometric signal containing information about the internal structure of the sample. A dual balanced detector (Thorlabs Model PDB120C) was used for detection. The dual balanced detector acts as a balanced receiver, subtracting the two optical input signals from each other and cancellating common mode noise. This allows small changes in the signal path to be visible over the interfering noise floor. A photograph of the SS-OCT system is shown in Fig. 3.2

Figure 3.2 A photograph of the Swept Source OCT System

3.3 Data Acquisition

Data acquisition is performed by a 14-bit data acquisition board (Ztec, ZT410) (for the measured signal) sampling at 40 Msamples/second, and the number of data points for each A-Scan is 2000. The A-Scan data acquisition start trigger for the digitizer was generated by the swept source. The triggering pulses which are needed for synchronization, are created by two National Instruments data acquisition boards, NI PCI 6115,and NI PCI 6014. The measured signals and triggering pulses are connected to the cards via an interface card (NI BNC-2110) with coaxial connectors. The data acquisition cards are controlled by a Labview program which handles the signal acquisition and storage. Fig. 3.3 shows the Labview user interface used for data acquisition.

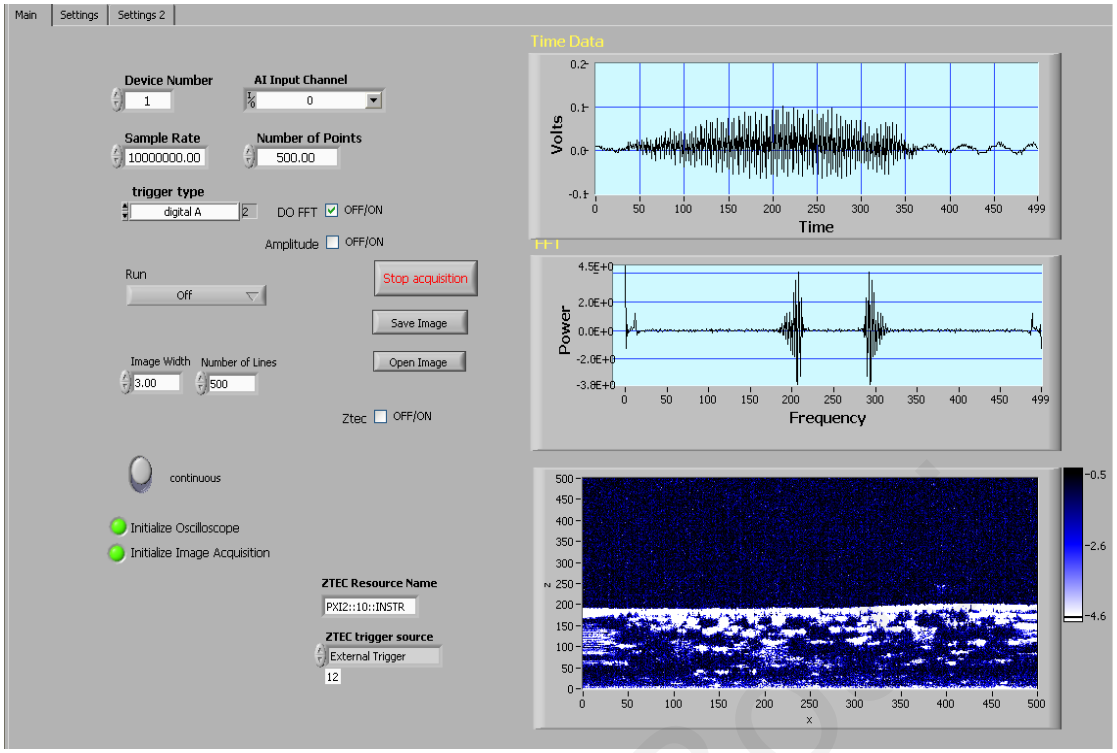

Figure 3.3 Labview user interface for data acquisition.

The data acquisition program operates as follows:

1. The Labview program is started, where parameters like the number of scans, sampling frequency, number of data points/scan, image width, and image depth are defined. The program runs on two modes, the oscilloscope mode and the image mode.

2. The trigger signal (TTL pulse) for each A-scan is created from the source. At every sweep of the source a TTL signal is created. The trigger signal from the source is slightly shifted with regards to the beginning of each sweep, so a second trigger pulse, which is shifted regarding to the first, is created to be synchronized with the beginning of each source sweep.

3. Upon arrival of each TTL pulse the DAQ acquires M samples. The number of samples in each A-scan is proportional to the imaging depth. With an A-scan rate of 20kHz, and a DAQ sampling rate of 40MHz, the maximum number of samples is 2000 points, which allows imaging of a one-sided depth of 3.9 mm.

4) For the image mode, the measurement program creates a transverse scanning start pulse, and forms a waveform which guides the servo driver of the galvanometer.

(a) The transverse scan pulse is used both as the trigger for the waveform which guides the galvanometer and also as the trigger for starting the image acquisition. In that manner, the transverse scanning is synchronized with the beginning of each image acquisition. The frequency of this pulse corresponds to the number of A-scans in the image. A-scans are taken so that the total amount of A-scans in an image covers the whole scanning range of the galvanometer scanner.

(b) For every transverse scan a sawtooth waveform is generated and passed to the servo-driver. This waveform ensures that the beam is scanned exactly the length required, at exactly the time it takes to collect the right number of A-scans.

5. If the user chooses to stop image acquisition, then the galvanometer is returned to its original position, and the program is stopped . The acquired signals can be saved in ASCII or binary format and used for data processing.

Fig.3.4 shows the flow diagram for data acquisition, and Fig.3.5 illustrates the synchronization signals in more details. Fig.3.6 shows the electrical connections between the various hardware components.

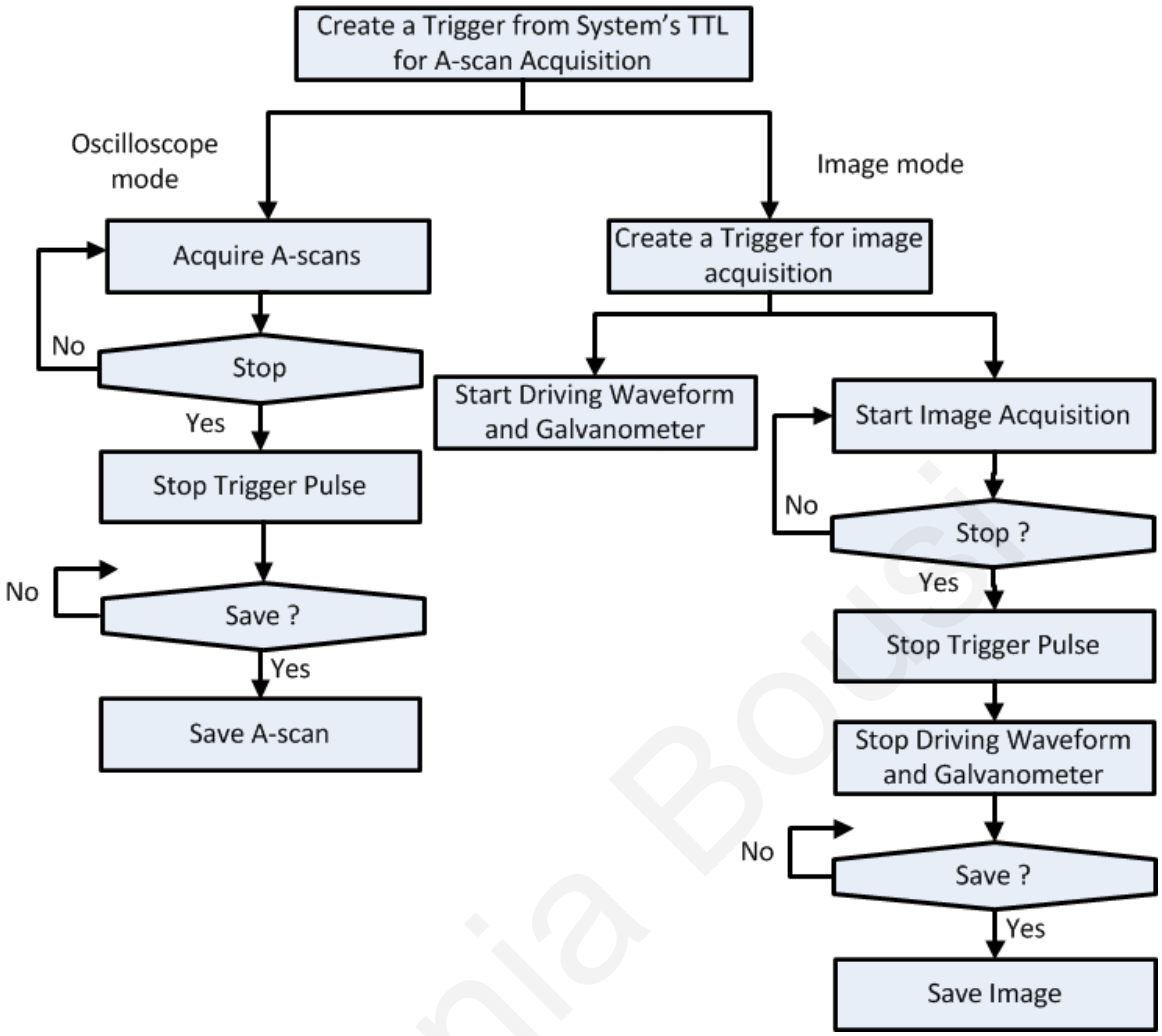

Figure 3.4 Flow diagram of data acquisition process

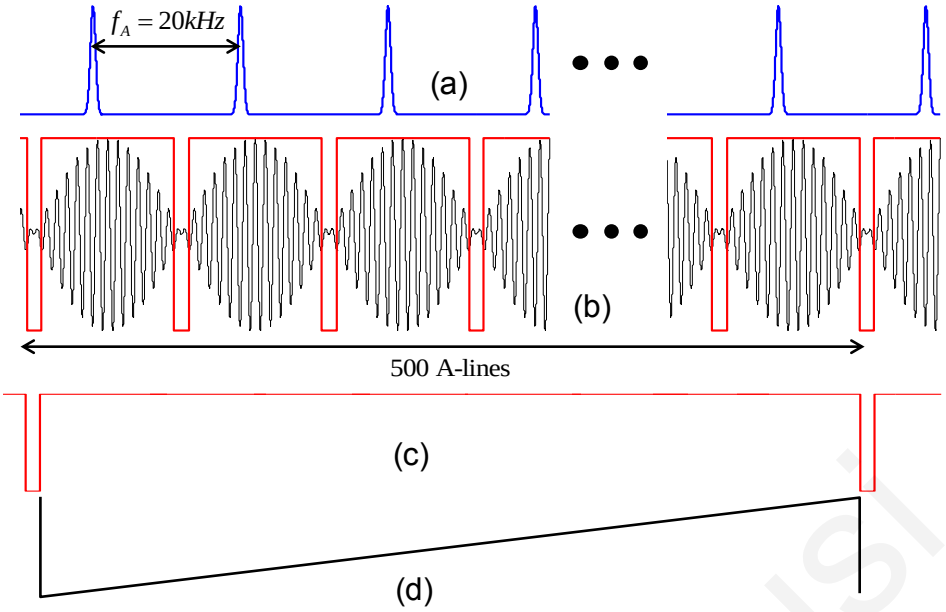

Figure 3.5 Synchronization diagram for data acquisition.(a) The trigger TTL pulse from the source for each A-scan acquisition.(b) (red) trigger pulse synchronized with the beginning of each sweep, (black) acquisition of A-scans with the DAQ. (c) Trigger signal for image acquisition and waveform generation for transversal scanning (image consists of 500 lines) . (d) Waveform for transversal scanning.

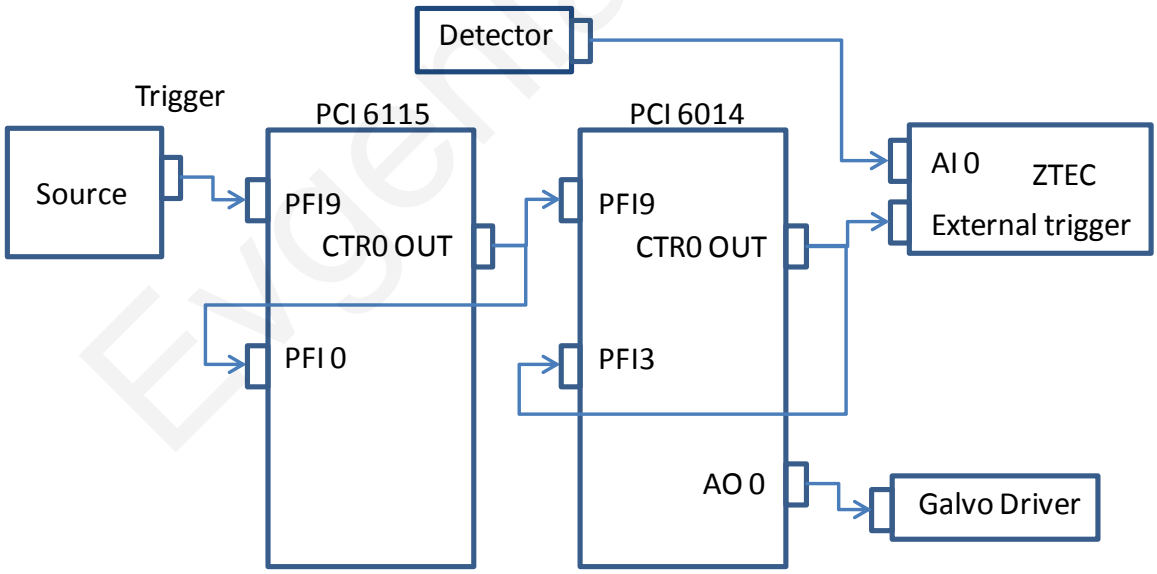

Figure 3.6 Electrical connection diagram

Three data acquisition boards (two National Instruments NI PCI 6115 and NI PCI 6014, and one ZTEC) are used in the system. The two National Instrument boards are used for the generation of synchronization pulses, and the ZTEC board is used for

acquiring the signal. Three counters from the NI boards, are used to generate the appropriate trigger signals: one counter to shift the trigger of the source so as to be synchronized with the beginning of each sweep and two counters to generate signals for the synchronization of the galvanometer with the image acquisition. The NI PCI 6115 card generates the shifted trigger signal at CTR0 out pin. This signal is also connecterd to the PFI0 pin of the same board. This pin is the digital trigger of the board, and can be used as the trigger for A-scan acquisition (oscilloscope mode).

The counter of NI PCI 6014 board, CTR0 OUT, is used as the trigger for the image acquisition. Its period corresponds to the number of A-scans in the image. This counter is connected to the PFI3 pin, which is the source of counter 1, and is used as the trigger for the generation of a clock signal to counter 1. This is used as a clock for the waveform generation at the analog aoutput (AO 0) pin of the board.

3.4 Digital signal and image processing

In a SS-OCT signal, several post processing steps must be performed on each spectrum prior to Fourier transformation. Those steps include reference light intensity background subtraction, and spectrum interpolation.

3.4.1 Background subtraction

A reference image can be acquired at the beginning of every image acquisition, by blocking the sample arm. This reference image consists of residual background signal from the reference light, which is a result of the wavelength-dependent splitting ratio of the 50/50 coupler, and imperfect symmetry of the balanced detectors. Subtracting the reference from the interference signal can account for source fluctuations between measurements and eliminate fixed-pattern artifacts at low frequencies (depths).

3.4.2 Interpolation to linear k-space

The Fourier-transform relationship between the time-domain fringe data and the Fourier-domain depth profile assumes a tuning source that sweeps linearly in k-space. Nonlinearity in the tuning curve of the laser results in chirping of the signal, and this variation in the characteristic frequency of a given reflection leads to resolution degradation in z-space. A solution to this image blurring problem is to sample the

detector signal in nonlinear time intervals to compensate for the frequency chirping of the source. Alternatively, the existing chirped signal can be numerically mapped to a uniform k-space by interpolation prior to Fourier transformaion. The method used in this work is k-space resampling by phase analysis [80],[81]. A description of the method is presented below.

The spectral interference signal of a SS-OCT system, measured with a plane mirror in the sample arm is given by:

$$\mathrm{I_m(t)} = \sqrt{I_r(t) I_s(t)} \cos\{2\pi\Delta\Phi\} \tag{1}$$

where

$$\Delta\Phi = 2\frac{L}{\lambda(t)} = \frac{2Lf(t)}{c} \tag{2}$$

Substituting Eq. 2 into Eq. 1, we have:

$$\mathrm{I_m(t)} = \sqrt{I_r(t) I_s(t)} \cos\{\frac{4\pi}{c} Lf(t)\} \tag{3}$$

where L denotes the path length difference between the two arms of the interferometer, I_r and I_s are the light intensities reflected from the reference and sample arm, respectively, c speed of light and $f(t)$ is the instantaneous source optical frequency. In this calibration method the instantaneous frequency $f(t)$ of Eq. 3 must be measured. Eq. 3 is Fourier transformed as:

$$\begin{aligned} F[I_m(t)] = F\{\sqrt{I_r(t) I_s(t)}\} \otimes \\ [F\left\{\exp(i\frac{4\pi}{c} z_0 f_2(t)\right\} \otimes \delta(\mu - \frac{2}{c} z_0 f_1) + \\ F\left\{\exp(-i\frac{4\pi}{c} z_0 f_2(t)\right\} \otimes \delta(\mu + \frac{2}{c} z_0 f_1)] \end{aligned} \tag{4}$$

where $F\{\cdot\}$ denotes the Fourier transform operator, $\otimes$ is the convolution operator, μ is the Fourier conjugate of t, and $f(t)$ is expanded as $f(t)=f_1 t + f_2(t)$. The convolved delta-functions of the first and second terms are responsible for their appearance at $\mu = \pm(2/c) z_0 f_1$. To measure the instantaneous phase, only the first term in Eq. 4 is needed. This term can be retrieved by Hilbert transformation of Eq. 3 which gives:

$$\mathrm{I_m(t)} = \sqrt{I_r(t) I_s(t)} \exp\{i\frac{4\pi}{c} Lf(t)\} \tag{5}$$

From this equation the corresponding measured unwrapped phase is given by the following equation:

$$\varphi_m(t_j) = \frac{4\pi L}{c} f_m(t_j) \tag{6}$$

where t_j is the time instant of the j-th sampling point and $\varphi_m(t_j)$ is the measured unwrapped phase of the j-th sampling point, which is equal to the phase of the Hilbert transform of Eq. 3. From Eq. 6 we see that the instantaneous source optical frequency is analogous to the measured unwrapped phase. In order to resample the data into wavenumber space, a functional relation $m(\varphi)$ between the sample number and φ has to be found. The relation $m(\varphi)$ is obtained by a polynomial fit to the retrieved phase. Next, the fractional indexes are easily found from the following relations:

$$m_i = m(\varphi_i) \tag{7}$$

$$\varphi_i = \phi_0 + \frac{\phi_{M-1} - \varphi_0}{M-1} i\,, \tag{8}$$

where M is number of samples in the spectral fringe signal. In the above equations values of the quantity φ are equidistant and so we can assume that they correspond to values of optical frequency and thus the values of wavenumber.

In the system developed here the unwrapped phase of the spectral fringes of the system with mirrors in both arms of the Michelson interferometer is measured. The optical path difference between the two arms is chosen to be large enough such that the image of the mirror and its complex conjugate do not overlap. The phase of the Hilbert transform of the spectral fringes provides the instantaneous phase.

Fig. 3.7 shows the results of the interpolation process at several depth positions. The blue curves represent the signal without interpolation whereas the red curve is the signal after interpolation. It is obvious that the interpolation process can suppress efficiently the depth dependent resolution decay. Fig. 3.7 also illustrates the depth dependent sensitivity. For this system the sensitivity roll-off is 6 dB at 3.2 mm.

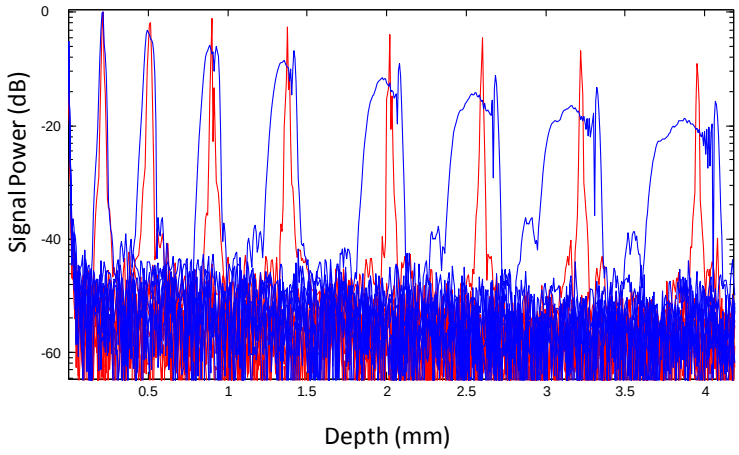

Figure 3.7 A-scans from a mirror obtained at different depths. Blue line are the A-scans without interpolation, and red line are the A-scans after interpolation.

3.5 System Characterization

3.5.1 Dynamic Range

The dynamic range of an OCT system is a measure which denotes the minimum detectable reflected optical power compared to a perfect reflector. The dynamic range of the system (sometimes referred to as "sensitivity") was measured to be 85 dB. This value was calculated as:

$$DR = 10\log\left[\frac{I_{max}{}^{2}}{\mathrm{var}(n)}\right] + 10\log(10^{OD}) \qquad (9)$$

where $I_{max}{}^{2}$ is the square of the peak A-scan amplitude (generated by a perfectly reflecting mirror), var(n) is the variance of the noise floor (measured with the sample arm blocked), and *OD* is the optical density of a neutral density filter. A 2 *OD* neutral density filter is placed in the sample arm to attenuate the power and prevent saturation. The value of 85 dB sensitivity is low for the light source used in this system. This may be due to the optical losses such as losses in the back-coupled light into the fiber interferometer, and losses in FC/APC attachments, remaining signal RIN, thermal noise of the detector, and circuit noise.

3.5.2 Imaging Range

Theoretically the maximum resolvable depth is given by Eq. 31 of Chapter 2 which is:

$$z_{\max} = \frac{\lambda_0^{\,2}}{4n(\Delta\lambda)}\mathrm{M}$$

This equation states that the imaging depth, for a given source bandwidth, is proportional to the the number of points (M) in the A-scan. With an A-scan rate of 20 kHz, and a DAQ sampling rate of 40MHz, the maximum number of points acquired during an A-scan is 2000. For M=2000, $\Delta\lambda$=110nm, λ_0=1310nm, the imaging depth is 7.8 mm in free space. Taking into account the mirror image, the usable depth becomes 3.9 mm. The experimental measurement of the one sided depth range as measured by reading the micrometer scale at the sample or reference arm translation stage is 4.2mm.

3.5.3 Sensitivity Roll –off

The sensitivity roll-off is a measure of the sensitivity drop of higher frequency interference signals or larger reference and sample arm distance mismatch, even if the reflectivity remains constant. This roll-off can be described as the one sided depth at which the sensitivity drops by one half or 6dB. Fig. 3.7 shows that a 6dB drop of the sensitivity occurs at 3.2 mm.

3.5.4 Axial Resolution

The theoretical axial resolution of the system is determined by the coherence length of the light source and is given by Eq. 19 of chapter 2. Given the characteristics of the light source used (λ_0=1310nm, and $\Delta\lambda$=93nm) the theoretical axial resolution is 8.3 μm. The experimental axial resolution is measured to be approximately 9.5 μm and is obtained by measuring the FWHM of an A-scan peak from a mirror. The difference of the experimental from the theoretical measurement of the resolution is due to different factors. First of all, the shape of the spectrum of the source is not perfectly Gaussian, resulting in reduced sensitivity and resolution. Another effect that limits axial resolution is a polarization mismatch between the interferometer arms, which introduces a phase difference and therefore a change in the shape of the coherence function and axial resolution respectively. The optical transmittance, the wavelength dependent loses of the fiber optics employed, the delivery system optics, and the detection system, including the electronics as well as the digitization and acquisition

of the interference signal, strongly influence the axial resolution as well as the sensitivity of the OCT system.

3.5.5 Lateral Resolution

The lateral resolution of the system depends on the delivery optics. For a Gaussian sample beam profile the lateral resolution is given by:

$$2w_0 = \sqrt{\frac{2b\lambda}{\pi}} \tag{10}$$

where b is the confocal parameter of the system and λ the center wavelength of the light source and $2w_0$ is the diameter of the focused beam at which the intensity falls by $1/e^2$ of the maximum intensity. The confocal parameter (b) is defined as twice the Rayleigh range, where the Rayleigh range is the distance from the minimum radius (w_0) to where the radius becomes $\sqrt{2w_0}$.

To calculate the lateral resolution of the system, the confocal parameter (b) is measured. A mirror is placed in the sample arm and the maximum intensity (which corresponds to the focus) is recorded. Afterwards the sample arm translation stage is moved up until the intensity drops to 0.69 of the maximum and the distance is measured with the micrometer of the translation stage. The same is repeated by moving the sample arm in the opposite direction and measuring the distance at which the intensity drops to 0.69 of the maximum. The sum of the two distances is the confocal parameter (b) of the system. In this thesis, the FWHM of the Gaussian defines the lateral resolution. This is related to the radius (w_0) by:

$$FWHM = w_0\sqrt{2\ln(2)}. \tag{11}$$

The measured lateral resolution of the system, given by Eq. 11 is 14 μm. The theoretical lateral resolution calculated from Eq. 29 of chapter 2 for d=1.54mm, f=22mm, and λ=1300μm, is $2w_0$=25.6μm, and the FWHM resolution given by Eq. 11 is 13.92μm which is consistent with the experimental measurement.

Chapter 4
Optical Coherence Tomography Axial Resolution Improvement by Step-frequency Encoding

4.1 Summary

In this chapter, a novel technique for axial resolution improvement of time domain optical coherence tomography (TDOCT) systems is presented. The technique is based on step-frequency encoding, using frequency shifting, of the OCT signal. A resolution improvement by a factor of ~ 7 is achieved without the need for a broader bandwidth light source. This method exploits a combination of two basic principles: the appearance of beating, when adding two signals of slightly different carrier frequencies, and the resolution improvement by deconvolution of the interferogram with an encoded autocorrelation function. In time domain OCT, step-frequency encoding can be implemented by performing two scans, with different carrier frequencies, and subsequently adding them to create the encoded signal. When the frequency steps are properly selected, deconvolution of the resulting interferogram, using appropriate kernels, results in a narrower resolution width.

4.2 Introduction

The axial resolution in OCT is inversely proportional to the spectral bandwidth of the light source, and is given by the relation:

$$\Delta z = 2\ln(2)\frac{\lambda^2}{\pi\Delta\lambda}$$

where λ is the center wavelength, and Δλ is the bandwidth of the light source. The most straightforward approach to improve the axial resolution is to use a light source with a broader spectral bandwidth. Superluminescent light sources offer a resolution which is limited to 10-15μm. A Kerr-lens mode-locked Ti:sapphire laser, Ti:sapphire pumped super-continuum generation, and thermal light sources were used to obtain 0.5-1 μm axial resolution in biological tissue [32][82][38][83][84]. Additional extracavity spectral broadening in highly nonlinear fibers allows for sub-micrometer (0.85μm) resolution OCT at 800 nm and sub-2-micrometer (1.4μm) resolution at 1.13 and 1.38 μm wavelength [85][35]. Simultaneous dual-band, ultra-high, resolution OCT imaging with an off-the-shelf all-fiber integrated supercontinuum (SC) source enables OCT imaging with 1.7 μm and 3.8 μm axial resolutions, at 840 nm and 1230 nm, respectively [86] . In a recent paper, the generation of ultrabroadband biphotons that span a bandwidth of ~ 300 nm with center wavelength λ_0 = 812 nm has also been reported [87]. Using these ultrabroadband biphotons in conjunction with semiconductor single-photon avalanche photodiodes (APDs), the narrowest axial resolution (0.85μm) was reported in quantum OCT (QOCT). However, there is a limit to the resolution improvement that can be achieved even by these state-of-the-art OCT systems. The inversely proportional, asymptotic, relationship between bandwidth and resolution implies that increasingly broader, often unattainable or unsustainable, bandwidths are required for marginal improvements in resolution. This is shown schematically in Fig. 4.1.

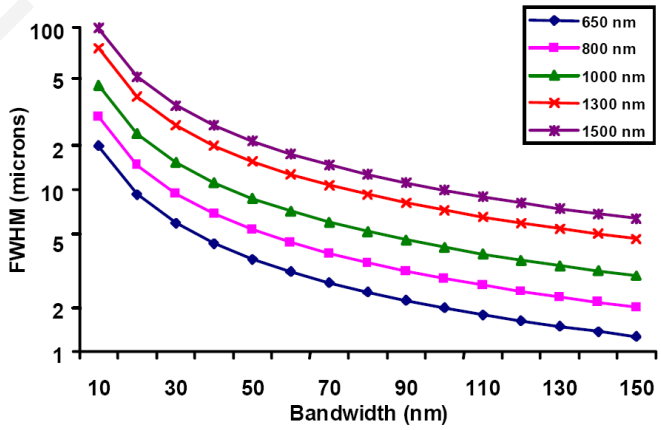

Figure 4.1 Axial resolution versus bandwidth illustrating the asymptotic relationship between axial resolution and bandwidth

Furthermore, there is an additional penalty of either a significant increase in system complexity and cost or loss of sensitivity and power attenuation as the source bandwidth is extended.

Resolution can also be improved using numerical processing techniques. The use of deconvolution techniques on OCT images was first reported in 1997 [73]. An increase in resolution by a factor of ~2 was obtained, as compared to the original interferogram. Promising results, using the CLEAN algorithm, were also reported in 1998 [88]. Recently, two-dimensional deconvolution methods, for deblurring, were shown to improve the quality of OCT images [89][10]. The maximum entropy method (MEM) was also shown to enhance the resolution in OCT [90]. Moreover, by digitally reshaping the source spectra to known modes, OCT resolution was improved by a few micrometers [91]. It was also shown, theoretically, that a chirped quasi-phase-matching nonlinear crystal structure can significantly enhance the axial resolution in QOCT by increasing the spectral width of the generated entangled photon pairs [92].

In this chapter, a simple technique that effectively improves the axial resolution of an OCT system, without the need of a broader bandwidth light source, is demonstrated. The technique is based on step-frequency encoding of the OCT interferogram. Signal encoding belongs to a group of methods used in radar, sonar, and ultrasound to augment the resolution as well as improve the SNR [93][94]. By linearly increasing, step by step, the frequency of successive pulses and adding them, the resolution can be significantly improved [93]. Since, in OCT, the detection is not based on pulse width and time-of-flight, the application of this technique has been appropriately modified. The proposed encoding scheme is based on the summation of scans with different carrier frequencies and deconvolution.

4.3 Methodology

The proposed method of resolution improvement is based on two basic principles: (i) the appearance of beating when adding two waves of slightly different frequencies, and (ii) the resolution improvement by deconvolution with an appropriately chosen kernel function.

4.3.1 Frequency Summation in Optical Coherence Tomography

The OCT signal, which results from the interference of two partially coherent light beams, can be expressed in terms of the source intensity, I_0, as

$$\mathrm{I} = k_1 R_R \mathrm{I}_0 + k_2 R_S I_0 + 2\sqrt{\left[k_1 R_R \mathrm{I}_0\right] \times \left[k_2 R_S I_0\right]}\,\mathrm{Re}[\gamma(\tau)] \qquad (1)$$

where $(k_1 + k_2) < 1$ represents the interferometer beam splitting ratio, R_S and R_R are the reflection coefficients from the sample and reference arm, and $\gamma(\tau)$ is the complex degree of coherence. The factor $\gamma(\tau)$ includes the interference envelope and carrier and depends on the reference arm scanning or time delay τ. Its recovery is of interest in OCT. The complex degree of coherence can be approximated by a Gaussian function expressed as

$$\gamma(\tau) = \exp\left[-\left(\frac{\pi \Delta f\, \tau}{2\sqrt{\ln 2}}\right)^2\right] \exp(-j 2\pi f_d \tau) \qquad (2)$$

where Δf is the spectral width of the source and f_d is the Doppler frequency. In Eq. 2, the Gaussian envelope is amplitude modulated by an optical carrier. The peak of this envelope represents the location of a reflector and/or a scatterer in the sample under test. Its amplitude depends on the reflectivity of the structure. The optical carrier is due to the Doppler shift resulting from scanning one arm of the interferometer, and the frequency of this carrier is controlled by the speed of scanning. The Doppler frequency is

$$f_d = \frac{2 v_{scanner}}{\lambda_0} \qquad (3)$$

where λ_0 is the center wavelength of the source, and $v_{scanner}$ is the scanning speed of the reference mirror.

In the case of a single scatterer and if $k_1 = k_2 = 0.5$, then the interference pattern can be written as:

$$I_{\text{interf}} = \sqrt{R_R R_S}\, I_0 \exp\left[-\left(\frac{\pi \Delta f\, \tau}{2\sqrt{\ln 2}}\right)^2\right] \cos(2\pi f_d \tau) \qquad (4)$$

By defining

$$S_0(t) = I_0 \exp\left[-\left(\frac{\pi \Delta f \tau}{2\sqrt{\ln 2}}\right)^2\right] \quad (5)$$

the interference pattern can be expressed as

$$I_{\text{interf}} = \sqrt{R_R R_S}\, S_0(t)\cos(2\pi f_d t) \quad (6)$$

4.3.1.1 Frequency Summation

Adding two A-Scans with two different but similar carrier frequencies, results in a beating pattern at each peak of the interferogram. For example if:

$$A_{i1}(t) = \sqrt{R_R R_S}\, S_0(t)\cos(2\pi f_1 t + \varphi_{i1}) \quad (7)$$

and

$$A_{i2}(t) = \sqrt{R_R R_S}\, S_0(t)\cos(2\pi f_2 t + \varphi_{i2}) \quad (8)$$

are two A-Scans from the same position of a single scatterer, *i* denotes the number of the A-Scan (e.g. the *i*-th A-Scan), and φ_{i1} and φ_{i2} are the initial phases of the A-Scans which can be different. The sum of the two A-Scans is:

$$A_i(t) = A_{i1}(t) + A_{i2}(t) = \sqrt{R_R R_S}\, 2S_0(t)\cos\left[\frac{2\pi(f_1+f_2)t + (\varphi_{i1}+\varphi_{i2})}{2}\right] * \cos\left[\frac{2\pi(f_1-f_2)t + (\varphi_{i1}-\varphi_{i2})}{2}\right] \quad (9)$$

If the frequencies are chosen correctly, the axial resolution can improve significantly. For example, if the frequencies are chosen such that the beating nodes appear at intervals corresponding to half the coherence length of the system, then the interferogram from a single reflector will have the appearance depicted in Fig. 4.2.

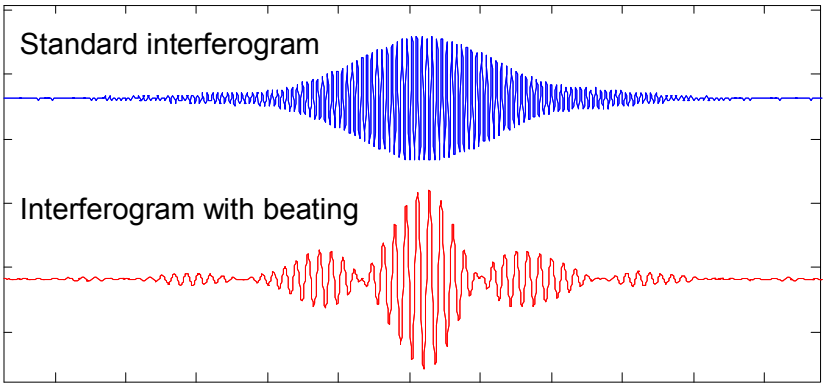

Figure 4.2 Beating of the interferogram of a single peak.

Filtering the carrier frequency $(f_1+f_2)/2$, results in a demodulated interferogram with beating frequency $(f_1-f_2)/2$:

$$A_i(t) = \sqrt{R_R R_S}\, 2S_0(t)\cos\left[\frac{2\pi(f_1 - f_2)t + (\varphi_{i1} - \varphi_{i2})}{2}\right] \qquad (10)$$

Eq. 10 implies that, if the initial phases from A-Scan to A-Scan are different, the beating patterns from A-Scan to A-Scan may be different. This will be further discussed in subsequent sections.

4.3.1.2 Discrete Reflectors

In the case of a sample consisting of discrete reflectors, the OCT interferograms at two frequencies f_1 and f_2 are given by:

$$A_{i1}(t) = \sum_{k=1}^{N} Rs_k h(t - t_k) \otimes S_0(t)\cos(2\pi f_1 t + \varphi_{i1}) \qquad (11)$$

$$A_{i2}(t) = \sum_{k=1}^{N} Rs_k h(t - t_k) \otimes S_0(t)\cos(2\pi f_2 t + \varphi_{i2}) \qquad (12)$$

where Rs_k are the reflection coefficients from different depths of the sample, $\otimes$ denotes the convolution operation, and $h(t)$ describes the actual locations of scattering sites within the sample.

The beating interferogram resulting from the addition of the two A-Scans is:

$$A_i(t) = A_{i1}(t) + A_{i2}(t) =$$
$$\sum_{k=1}^{N} Rs_k h(t-t_k) \otimes 2S_0(t) \cos\left[\frac{2\pi(f_1+f_2)t + (\varphi_{i1}+\varphi_{i2})}{2}\right] \cos\left[\frac{2\pi(f_1-f_2)t + \varphi_{i1}-\varphi_{i2})}{2}\right] \quad (13)$$

Filtering the carrier frequency $(f_1+f_2)/2$ results in an A-Scan with beating frequency $(f_1-f_2)/2$:

$$A_i(t) = \sum_{k=1}^{N} Rs_k h(t-t_k) \otimes 2S_0(t) \cos\left[\frac{2\pi(f_1-f_2)t + \varphi_{i1}-\varphi_{i2})}{2}\right] \quad (14)$$

Eq. 14 includes a phase term which can affect the beating pattern of the interferogram. The results, as well as remedies, of this term are discussed in sections 4.3.2 and 4.3.3.3.

4.3.2 Deconvolution of the OCT signal

The OCT interferometric signal is a cross correlation function between the actual locations and reflection coefficients of scattering sites within the sample and the source autocorrelation. Taking the Fourier transform of both sides of Eq. 14 and solving for the impulse response $h(t-t_k)$, one can theoretically recover the scatterer locations. This is the simplest deconvolution algorithm in image restoration, called inverse filtering, resulting in :

$$\mathcal{F}(A_i(t)) = \sum_{k=1}^{N} \mathcal{F}(Rs_k h(t-t_k)) \times \mathcal{F}(2S_0(t) \cos\left(\left[\frac{2\pi(f_1-f_2)t + (\varphi_{i1}-\varphi_{i2})}{2}\right]\right) \quad (15)$$

$$\mathcal{F}(R_{sk} h(t-t_k)) = R_{sk} H(\omega) e^{j\omega t_k} \quad (16)$$

Basic Fourier transform properties define that:

$$\cos(\omega_0 t) = \pi(\delta(\omega-\omega_0) + \delta(\omega+\omega_0)) \quad (17)$$

and

$$\cos(\omega_0(t-t_0)) = e^{-j\omega t_0}\pi(\delta(\omega-\omega_0)+\delta(\omega+\omega_0)) \qquad (18)$$

so

$$\mathcal{F}\left(2S_0(t)\cos\frac{2\pi(f_1-f_2)t+(\varphi_{i1}-\varphi_{i2})}{2}\right)=$$

$$\mathcal{F}\left(2S_0(t)\cos[\omega_0(t+\frac{\Delta\varphi_i}{\omega_0}]\right)=2S_0(\omega)\otimes\left[\pi e^{-j\omega\frac{\Delta\phi_i}{\omega_0}}(\delta(\omega-\omega_0)+\delta(\omega+\omega_0))\right]= \qquad (19)$$

$$2\pi e^{-j\omega\frac{\Delta\phi_i}{\omega_0}}\left[S_0(\omega-\omega_0)+S_0(\omega+\omega_0)\right]$$

where $\omega_0=\frac{2\pi(f_1-f_2)}{2}$, and $\Delta\varphi_i=\frac{\varphi_{i1}-\varphi_{i2}}{2}$. As a result, Eq. 16 and Eq. 19 give:

$$\mathcal{F}(A_i(t))=\sum_{k=1}^{N}Rs_kH(\omega)e^{j\omega t_k}2\pi e^{-j\omega\frac{\Delta\phi_i}{\omega_0}}\left[S_0(\omega-\omega_0)+S_0(\omega+\omega_0)\right] \quad (20)$$

By dividing with the Fourier transform of a kernel from a single peak, i.e the peak at the location t_m of the m-th A-scan:

$$A_m(\omega)=2\pi e^{-j\omega\frac{\Delta\phi_m}{\omega_0}}\left[S_0(\omega-\omega_0)+S_0(\omega+\omega_0)\right] \qquad (21)$$

and taking the inverse Fourier transform, we can extract the approximate reflectivity profile of the sample:

$$Rs_k\hat{H}(\omega)=\frac{\mathcal{F}(A(t))}{A_m(\omega)}=\sum_{k=1}^{N}H(\omega)e^{j\omega t_k}e^{j\omega(\frac{\Delta\varphi_i-\Delta\varphi_m}{\omega_0})} \qquad (22)$$

and

$$Rs_k\hat{h}(t)=h(t)=\sum_{k=1}^{N}h\left(t-t_k-\frac{\Delta\varphi_i-\Delta\varphi_m}{\omega_0}\right). \qquad (23)$$

Hence, theoretically, we can successfully extract the reflectivity profile albeit with a distance shift of $\frac{\Delta\varphi_i-\Delta\varphi_m}{\omega_0}$ from the real position of each scatterer. This shift is a

result of the different phases of the interferograms, which leads to different beating patterns from peak to peak and from A-Scan to A-Scan. The implications and remedies of this distance shift will be discussed in a section 4.3.3.3.

Eq. 22 is the simplest deconvolution algorithm in image restoration, called inverse filtering. Because deconvolution in real space is equivalent to division in Fourier space, the inverse filtering algorithm divides the Fourier transform of an image by the Fourier transform of the PSF. Although the calculation is rapid, the utility of this method is limited by noise amplification. During division in Fourier space, small noise variations are amplified by the division operation. The result is a trade-off between blur removal and noise gain. To avoid this trade-off a number of other algorithms have been developed for image restoration. These algorithms are the so-called "constrained iterative algorithms." They work in successive cycles and, also, apply constraints on possible solutions. These constraints not only help to minimize noise or other distortions but also increase the power to restore a blurred signal.

One such algorithm is the Lucy-Richardson algorithm [9] which is a technique widely used for restoring OCT images[10][89]. The algorithm is defined by[10]

$$f_{m+1}(x,y) = f_m(x,y)\left[h(-x,-y) * \frac{g(x,y)}{h(x,y) * f_m(x,y)} \right] \qquad (24)$$

where $f_m(x,y)$ is the estimate of the original image, $g(x,y)$ is the degraded image, $h(x,y)$ is the PSF, and m is the number of iterations. The reason for the popularity of this algorithm, which is based on a maximum likelihood estimation, is its ability to produce reconstructed images of good quality even in the presence of high noise levels [95]. The algorithm maximizes the likelihood that the resulting image, when convolved with the PSF, is an instance of the blurred image assuming Poisson noise statistics. Because it uses probabilistic error criteria, this algorithm can provide slightly better restoration than other classical techniques. Also, since it takes into account statistical fluctuations in the signal and suppresses iterations when values deviate in the vicinity of their original value, it reduces noise amplification[95]. The Lucy-Richardson algorithm is used in this work for deconvolution.

4.3.3 Step Frequency Encoding, Resolution Enhancement, and Limitations

The axial resolution of an OCT image can be significantly improved, when step frequency encoding is combined with deconvolution.

4.3.3.1 Axial Resolution Improvement with Step Frequency Encoding and Deconvolution

By adding two A-Scans at two different frequencies, beating will appear and the interferogram from a single reflector will have the appearance depicted in Fig. 4.2. Already there is an improvement in the full width half maximum (FWHM) of the central lobe and, therefore, the resolution. The resolution improvement results from the fact that the encoded central lobe is narrower than the equivalent envelope of a standard OCT scan. The degree of the improvement depends on the frequency steps. In the encoded case the FWHM of a peak is the width τ of the central lobe which can be calculated by:

$$\sin\left(2\pi(\frac{f_1-f_2}{2})(t+\tau)\right)=0.5\Rightarrow 2\pi(f_1-f_2)(t+\tau)=\frac{10\pi}{6} \qquad (25)$$

$$\sin\left(2\pi(\frac{f_1-f_2}{2})t\right)=0.5\Rightarrow 2\pi(f_1-f_2)t=\frac{2\pi}{6} \qquad (26)$$

When combined, Eq. (27) and (28) give:

$$2\pi(f_1-f_2)\tau=\frac{8\pi}{6}\Rightarrow\tau=\frac{2}{3(f_1-f_2)} \qquad (27)$$

After deconvolution an additional resolution improvement of a factor of ≥ 2 occurs which results in:

$$\tau=\frac{1}{3(f_1-f_2)} \qquad (28)$$

From the relation $x = v\tau$, where v is the velocity of the scanner, the improved resolution is at least

$$dx = \frac{v}{3(f_1 - f_2)} \tag{29}$$

The resolution improvement depends on the beating frequency and higher beating frequencies, resulting in narrower peak widths. However, increasing the frequency difference between steps is not without a penalty since the interferogram's sidelobes increase.

4.3.3.2 Sidelobe Amplitude

One of the important limitations of this technique is the appearance of sidelobes. The relative size of the sidelobes can be calculated assuming a Gaussian envelope for the interferogram, i.e.:

$$A(t) = A_c e^{-\left(\frac{\pi \Delta f t}{2\sqrt{\ln 2}}\right)^2} \tag{30}$$

where Δf is the spectral width of the source, and A_c is the peak amplitude. In the case of step frequency encoding of the pulse the period at which the sidelobes occur is $T = 1/(f_1\text{-}f_2)$, and the peak of each sidelobe occurs at T .Therefore the amplitude of the first and worst sidelobe is:

$$A_s = A_c e^{-\left(\frac{\pi \Delta f}{2(f_1 - f_2)\sqrt{\ln 2}}\right)^2} \tag{31}$$

From Eq. 31 we can see that, if the frequency steps are larger, the amplitude of the sidelobe A_s is larger. In addition there are more sidelobes in the range of a coherence length. Fig. 4.2 illustrates how the amplitude and number of sidelobes can increase with increasing frequency steps ($f_1\text{-}f_2$). In Fig. 4.3(a), the frequency difference is smaller (3kHz) than in Fig. 4.3(b) (6kHz). The increase in the number and amplitude of the sidelobes is evident in the latter case.

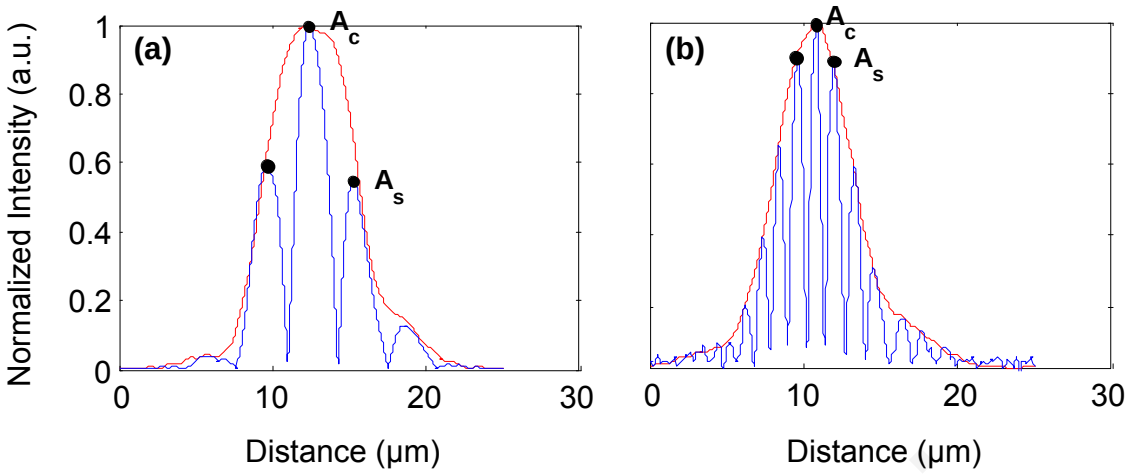

Figure 4.3 Dependence of sidelobes from frequency steps. (a) 3kHz frequency difference between steps. (b) 6kHz frequency difference between steps. Intensity scales are linear.

The sidelobe limitation is to a large extend remedied by deconvolution with appropriate kernels and further multiplying by the deconvolved envelope of the standard OCT signal. In the case of an encoding scheme similar to that of Fig. 4.3(a), where the sidelobes are at ~ 05-0.6 of the central lobe, a reduction of as much as 45 dB (typically) was achieved after deconvolution and multiplication. In an encoding scheme similar to that of Fig. 4.3(b) such a reduction would be more challenging, hence the tradeoff between resolution improvement and sidelobe intensity.

4.3.3.3 Location Shift

Since OCT does not detect the reflected replicas of a single pulse, as in ultrasound or radar, there is a fundamental problem. When externally modulating the light, as proposed in the following experimental section, each A-Scan can have a different phase from the next A-Scan, and each peak can have a different phase from the next peak in the same interferogram. This leads to different beating patterns from A-Scan to A-Scan and from peak to peak where the nodes of the beating can be at random locations relative to the center of the interferometric peak. The location shift from the real location of the scatterers, as is described by Eq. 23, is a result of the different phases of each interferogram which lead, after addition, to different beating patterns (Fig. 4.4).

The minimum shift from the real location occurs at a phase shift of zero (Fig. 4.4 (a)), whereas the maximum shift is at π/2 (Fig. 4.4 (b)). From the relation $\Delta\varphi = \omega_0 \Delta t$, where $\omega_0 = 2\pi(f_1 - f_2)/2$, the maximum location shift is:

$$\Delta t = \frac{\frac{\pi}{2}}{2\pi \frac{(f_1 - f_2)}{2}} = \frac{1}{2(f_1 - f_2)} \tag{32}$$

This can be converted to distance given the relation $\Delta x = v\Delta t$

$$\Delta x = \frac{v}{2(f_1 - f_2)} \tag{33}$$

where v is the velocity of the scanner. Therefore the maximum location shift is inversely proportional to the frequency difference of the two A-Scans. The bigger the frequency difference the smaller is the distance error.

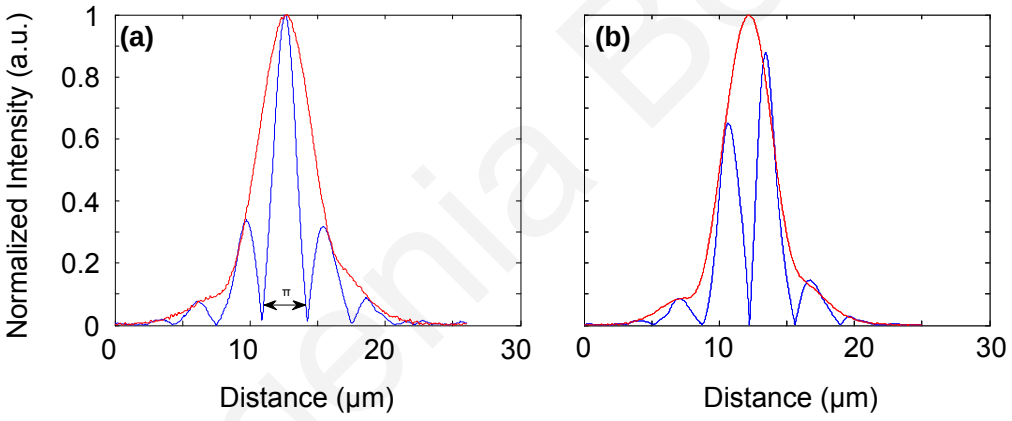

Figure 4.4 Different beating patterns as a result of different phases of interferograms.(a) zero distance shift corresponding to zero phase shift of the main lobe from the real position. (b), maximum distance shift corresponding to π/2 phase shift of the main lobe from the real position. Intensity scales are linear.

The problem of the location shift can be partly alleviated by performing deconvolution with several kernels corresponding to different beating pattern, and subsequently multiplying the results. It was noted experimentally that using three such kernels was adequate to reduce the positional variation. Even after multiple deconvolutions the uncertainty related to the initial phase of each A-Scan remains. An algorithm for motion correction was used to alleviate this problem.

The motion correction algorithm applied to the OCT images is a very simple correction algorithm which combines good performance with acceptable results. It is based on the alignment of the specular reflection of the top edge of the sample. For

each A-Scan, the position of the top edge in the image was determined using a pre-defined threshold and, subsequently, median filtered. A correction factor was calculated by interpolating between neighboring positions such that, when the A-Scan position is corrected by that factor, the corrugation artifact caused by motion is smoothed.

4.3.3.4. Design Trade-offs

The trade-off between sidelobe intensity and number, location shift error, and resolution improvement is obvious from Eq. 29, 31, 35. The greater the frequency difference of the A-Scans, the smaller the distance shift error,and the greater the resolution improvement. However, the number and intensity of sidelobes is also increased. A careful selection of frequency steps is necessary to obtain optimal results for resolution improvement while maintaining tolerable levels of sidelobe amplitude and distance shift error. From simulation and experimental data, it appears that an appropriate choice for the frequency steps is such that the beating pattern has a period of half the coherence length of the system. Such a value, results in a resolution improvement by a factor of 3 with a total improvement by a factor of ≥ 6 with subsequent deconvolution. In addition, the main sidelobe level is ~ 0.5 that of the main peak which can be sufficiently reduced by multiple deconvolutions to avoid significant detail degradation. If T is the time it takes for one coherence length to be scanned by the TD OCT system (T = coherence length / velocity of scanning), then the beating frequency must be $f_{beat} = (f_1 - f_2) = 2/T$. As with any design trade-offs, there values will highly depend on system design and imaging study specifics.

4.4 Experimental Method

Fig. 4.5 depicts the experimental setup of the time domain (TD) OCT system used in this study. It consisted of a superluminscent source (SLD) and a fiber optic-based Michelson interferometer. The SLD, operating at a centre wavelength $\lambda_0 \approx 1300$ nm and spectral FWHM of ~ 50 nm, resulted in an axial resolution of 13.5μm. The transverse resolution of the system was 16.5 μm, the power of light incident on the sample was 8mW, and the sensitivity of the system was measured to be 106 dB. The reference arm was scanned by translating a retro-reflector with a galvanometer at a velocity of 17.5mm/sec. The system employed two acousto-optic frequency shifters, (FS1 and FS2, 25 MHz, variable 5MHz bandwidth, 1st-order diffraction, from

Brimrose Inc.), one in the reference and one in the sample arm. The two frequency shifters were driven with a dual channel RF driver to produce a net frequency shift and added to the system a total insertion loss of 5 dB. The signal from the detector was then digitized using a 16-bit 1.2 MHz data acquisition board.

Encoded images were acquired by taking two A-Scans at each point, with f_1 =100kHz and f_2 =103kHz, and subsequently adding them, to produce a beating frequency of 3 kHz which corresponded to about half the coherence length for the giving reference arm scanning scheme. This beating frequency satisfied the requirements, discussed before, to achieve optimal results for resolution improvement while maintaining tolerable levels of location shift and sidelobe amplitude.

A reference sample (three microscope cover slips of ~ 170 μm thicknesses) was used to extract single peak interferograms subsequently used as kernels for the deconvolution (Fig. 4.6). Standard and encoded OCT images were collected, processed and compared.

To enhance the visibility of important structures, images should be displayed with high contrast resolution. The minimum and maximum values of the pixels, create a window. Displaying the full range of the window presents the information with very poor contrast. Shrinking the window increases contrast. Changing the center of the window, changes the brightness of the image. In this thesis, for display reasons, the minimum and maximum values for the window are entered manually and are determined in terms of percent of standard deviation from the mean value. By changing the minimum and maximum values of the window, the center of the window is updated automatically, and contrast and brightness can be adjusted appropriately.

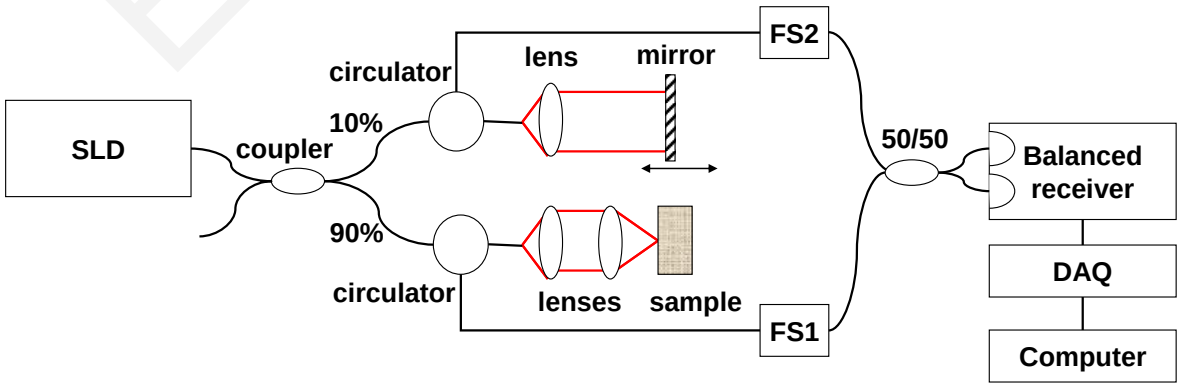

Figure 4.5 Configuration of the experimental time domain (TD) OCT system

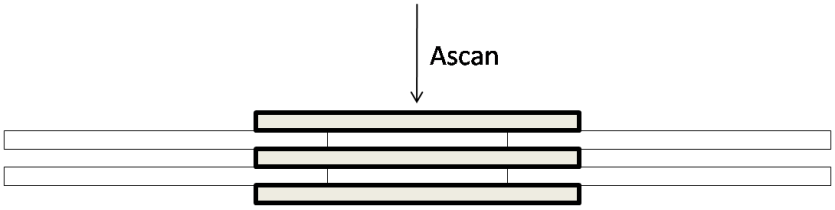

Figure 4.6 Sample, consisting of 3 microscope cover slips (~ 170 μm thickness, spaced at ~ 170 μm apart), used to collect the interferograms of 6 individual peaks from each A-Scan. They were subsequently used as kernels for the deconvolution.

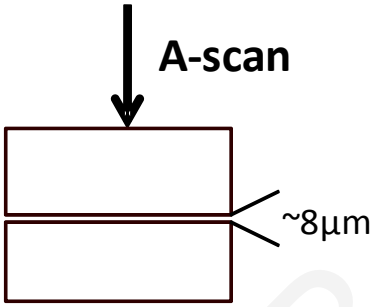

Figure 4.7 Sample consisting of two tightly adjacent microscope slides used to evaluate the resolving power of the proposed technique**.**

A limitation of the experimental approach described above is that the acquisition time is twice that of standard OCT, since two A-Scans are acquired at each point in the sample. This limitation can probably be addressed in the future by using more than one acousto-optic modulators in the reference arm. The processing time for an image of 39.064 KB is 35.034seconds in a 2.5GHz PC using Matlab 2008 and is the same with the processing time of the standard OCT image. The step that is the most computationally expensive is the deconvolution step for both modulated and standard OCT image. The processing time for a standard OCT image without performing deconvolution is 2.292921 seconds, and the processing steps are demodulation and display.

4.5. Results

The resolution of a system, as defined by Rayleigh, is its ability to discriminate adjacent structures in an image. In order to illustrate the improvement in OCT resolution, using the proposed method of encoding, images were acquired from two glass microscope slides tightened together (Fig.4.7). The two adjacent, inner, glass

surfaces, with an air gap of ~ 8 μm between them (measured from the encoded OCT A-Scans after processing) provided a suitable target for the evaluation of the system's axial resolution. The kernels used for deconvolution are shown in Fig. 4.8(a) and 4.8(b.) They were collected experimentally from the target described in Fig. 4.6. Fig. 4.*8(*a) shows the kernels used for the deconvolution of a standard OCT image whereas Fig. 4.8(b) shows the kernels for the deconvolution of the encoded image.

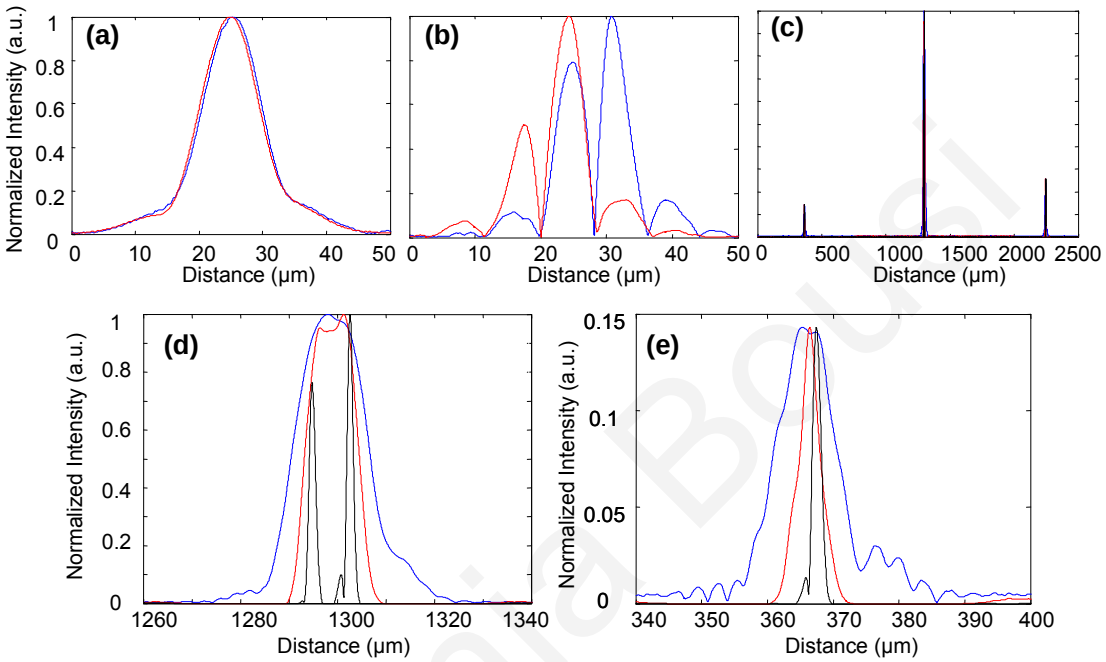

Figure 4.8 (a) Single peaks from demodulated standard OCT interferogram used as kernels for deconvolution. (b) Single peaks from demodulated encoded OCT interferogram used as kernels for deconvolution. (c) A-Scan from standard OCT (blue line), and deconvolution of demodulated A-Scans from standard (red line) and encoded OCT(black line) in one plot for comparison reasons. (d) Center peak of Fig. 4.8(c). (e) First peak of Fig. 4.8(c). y axis normalized, (a) and (b) normalized to 1, (d) and (e) normalized to the highest peak of (c). Intensity scales are linear.

Fig. 4.8(c-e) illustrates the results of the proposed method and provides a quantitative measure of the resolution improvement achieved. Fig. 4.8(c) is a plot of a single OCT A-Scan showing the reflections from the faces of the two glass microscope slides. The middle peak is the reflection from the two adjacent middle surfaces, a close-up of which is shown in Fig. 4.8(d). The blue line is a standard OCT scan (with no deconvolution), the red line is the standard OCT scan after deconvolution with the kernels of Fig. 4.8(a), and the black line is the encoded OCT scan after deconvolution with the kernels of Fig. 4.8(b). The two adjacent surfaces were not discernible using standard OCT and appeared as a single peak. Even when deconvolution was performed on the standard OCT signal the two peaks where still not clearly resolved.

With step-frequency encoding and deconvolution the two peaks are unmistakably separated.

The improvement in the axial resolution of the system was quantified by examining the reflections from one of the single surfaces, in this case the peak at 2250 μm, a close up of which is shown in Fig. 4.8(e). The standard OCT resolution was measured to be 13.5 μm. After deconvolution of the standard OCT interferogram, the resolution improved to 6 μm and, after applying step-frequency encoding and deconvolution, was further improved to 1.9 μm, approximately a seven-fold improvement. This is consistent with the theoretical analysis of the technique which predicted:

$$x = v\tau = v\frac{1}{3(f_1 - f_2)} = 1.94\mu m. \qquad (34)$$

The technique was also tested on a biological sample. Fig. 4.9(a) shows a small region (1.5x0.5 mm) of an onion image acquired with standard OCT. Fig. 4.9(b) shows the same region after deconvolution of the standard OCT image. Axial resolution improvement is evident. Fig. 4.9(c) is the onion image acquired with encoded OCT after deconvolution and Fig. 4.9(d) is the same image with the distance shift corrected using a simple motion correction algorithm. In this image, there is an improvement in resolution which results in the appearance of the characteristic onion double wall structures as evident from the zoomed regions of the same images in Fig. 4.10. The presence of the wall structure is also recognized in Fig. 4.10(e) which is a light microscopy image of onion cells. The distance between the cell membranes, measured from the encoded OCT images, was found to be between 8.0 and 8.4 μm, which is consistent with the literature (6-10 μm corresponding to the thickness of two cell walls.). This is a case of new information, revealed using the proposed technique, which would have been previously unavailable. The fact that this is indeed a feature of the sample and not an artifact, as might be suggested below when discussing Fig. 4.12 and 4.13, is further substantiated by the fact that the double line artifact produces lines at a distance of 3-4 μm (Fig. 4.12 & 4.13) and it is not present in other biological samples, such as those of lung (Fig.4.11.)

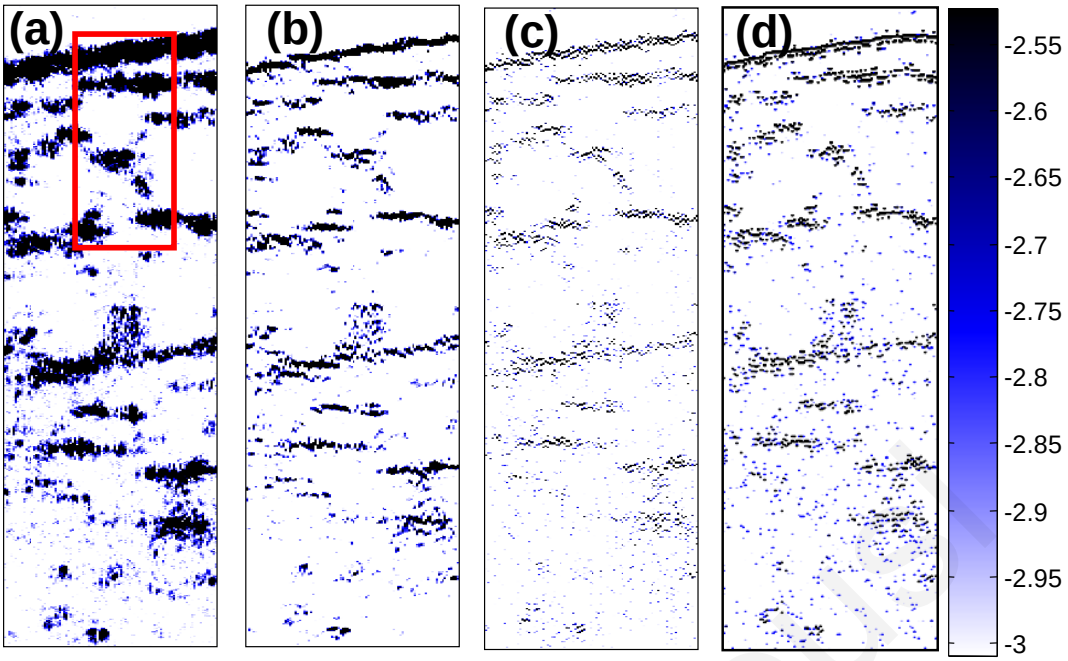

Figure 4.9 (a) Onion imaged with standard OCT, (b) after deconvolution of the standard OCT image, (c) onion imaged with encoded OCT after deconvolution and (d) onion image with encoded OCT after deconvolution and motion correction. (Image size: 1.5mm x 0.5 mm). The area in the red rectangle appears in Fig. 4.10. Intensity scales are log.

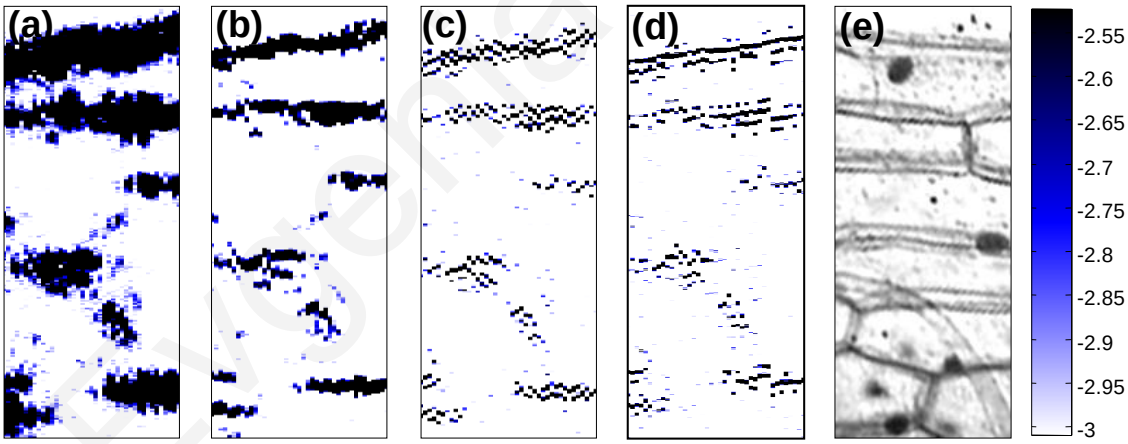

Figure 4.10 (a) Onion imaged with standard OCT, (b) after deconvolution of the standard OCT image, (c) onion imaged with encoded OCT after deconvolution., (d) onion image with encoded OCT after deconvolution and motion correction and (e) Light microscopy image of onion cells. (Image size: 0,5mm x 0,2 mm). Intensity scales are log.

Rabbit lung parenchyma was also imaged, *ex vivo*, to further demonstrate the applicability of the proposed technique to biological samples. The tissue was harvested immediately post termination and preserved in phosphate buffered saline at 4 ^{o}C. Imaging was performed within about half an hour after harvesting. The zoomed

images in Fig. 4.11 (d, e, and f) illustrate how the additional resolution improvement revealed small alveoli which in standard OCT appeared as highly backreflecting dark areas. *In vivo* imaging of tissue samples was not performed due to the speed limitations of this system. However, given the effect of this method on resolution and speckle, there is no reason to believe that it would not be applicable to *in vivo* tissue imaging.

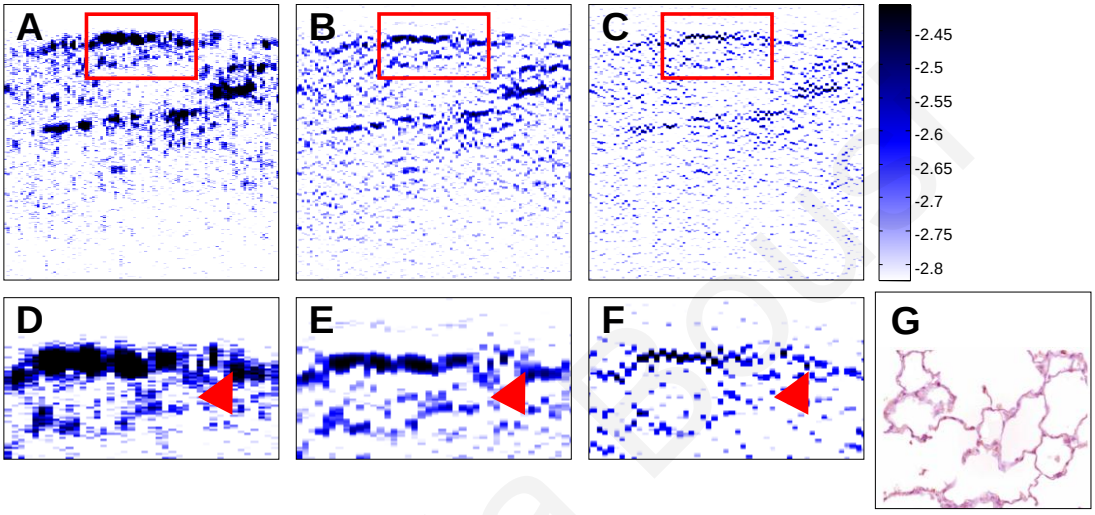

Figure 4.11 (a) Rabbit lung parenchyma imaged *ex vivo* with standard OCT, (b) after deconvolution of the standard OCT image, and (c) imaged with encoded OCT after deconvolution. (Image size: 0,5mm x 0,5 mm). (d – f) Details of images a-c, where small alveoli are indicated by the arrow. (e) Light microscopy image of a section of lung parenchyma from an unrelated site included for reference purposes. Intensity scales are log.

The proposed method is heavily depended on deconvolution. As a result, the effect of the method on speckle might be a concern. This effect was also investigated experimentally based on images consisting entirely of speckle. These images were acquired from samples consisting of polysterine microspheres (2 μm diameter) embed in acrylamide gel in a concentration such that each imaging voxel included ~10 spheres. These samples were prepared based on the technique described in the literature [96]. The results, shown in Fig. 4.12 and Fig. 4.13, indicate that neither the Lucy-Richardson deconvolution nor the step-frequency encoding and deconvolution significantly affect the amplitude of the speckle. However, they result in a progressively finer texture.

Fig. 4.12 and 4.13 also illustrate a possible artifact of the proposed technique which must be seriously considered when interpreting the improved OCT images. Highly

intense, specular, reflections, such as those present at the top surface of flat, highly reflective samples, can be mistakenly identified as a double layer. This is a result of the increased intensity of the sidelobes of the actual source, which in the case of the source used here, is not perfectly Gaussian (see blue line in Fig. 4.13.) Fortunately, this artifact is not present in biological tissues, such as the example of the lung images shown in Fig. 4.11.

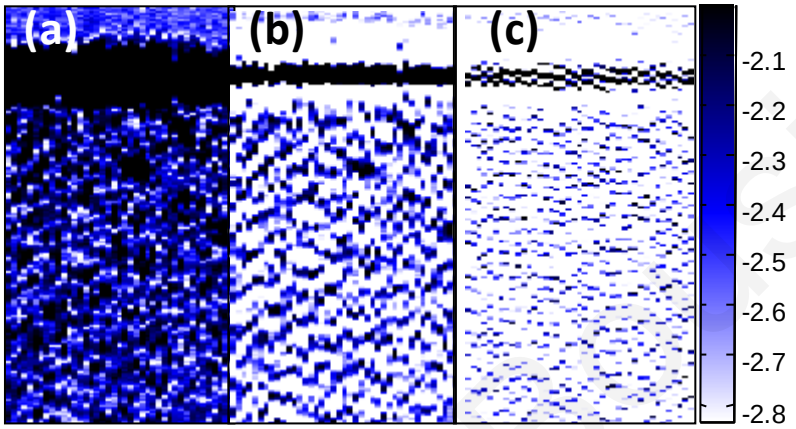

Figure 4.12 Speckle images from (a) standard OCT, (b) deconvolution of standard OCT, and (c) step-frequency encoded and deconvoluted OCT. The images are displayed using the same contrast and brightness scale for comparison purposes. Each image is 1.5x0.8 mm. Intensity scales are log.

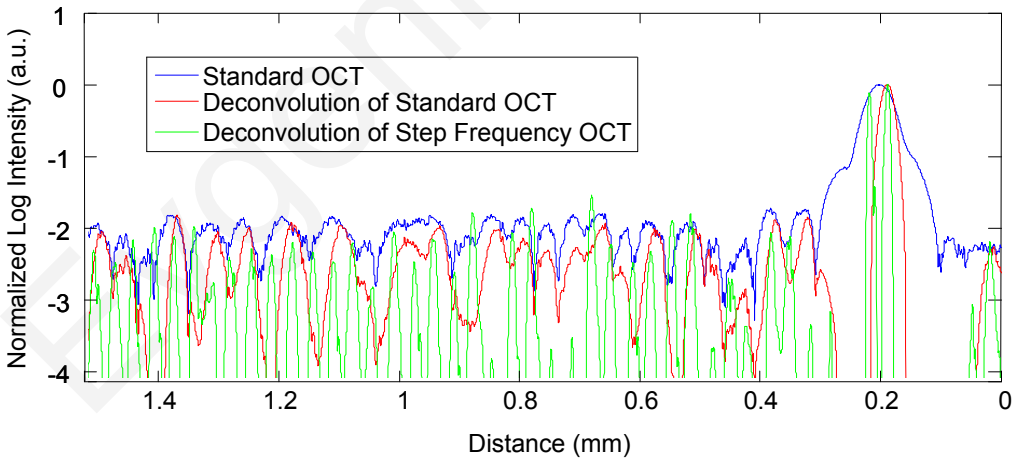

Figure 4.13 Single OCT A-Scans from the images of Fig. 9: standard OCT (blue), deconvoluted standard OCT (red), and encoded and deconvoluted OCT (green) signals. Specular reflections appear at the surface of the sample (at 0.2 mm).

4.6 Conclusion

By encoding the OCT interferogram and subsequently demodulating and deconvolving, significant axial resolution improvement was achieved without the

need of a broader bandwidth light source. The resolution improved significantly in this case by a factor of ~7. By choosing appropriately the frequency steps, it is expected that the technique can be applied for any OCT source (different resolutions, wavelengths, dynamic range) with the same performance. Also it is expected that the method will have the same performance if we increase the imaging speed or digital resolution. However, an increased imaging speed and digital resolution, results in standard OCT images with better quality and resolution.

Recently, cost-effective, broad-bandwidth, advanced SLD light sources have become available that approach the image resolutions achieved by femtosecond lasers. These light sources are multiplexed SLDs consisting of two or three spectrally displaced SLDs that are combined to synthesize a broad-bandwidth spectrum. Multiplexed SLD light sources have the disadvantage of spectrally modulated emission spectra that produce sidelobes in the coherence function or axial point spread function, thus resulting in image artifacts. On the positive side, multiplexed SLD light sources are much lower cost and more robust than femtosecond lasers, and they promise to enable wider availability of ultrahigh-resolution OCT. However, with step frequency encoding we can achieve better results, in image resolution and quality, with the use of only one SLD source. This means than the cost of the OCT system, is significantly reduced, while the performance is image resolution is improved.

Despite the limitations of this very preliminary implementation of step-frequency encoding, it is evident that this technique has the potential to dramatically enhance the resolution of OCT systems. In addition, different forms of encoding can be implemented, both in the time and Fourier domain, which will not suffer from the limitations uncovered in these experiments.

Chapter 5
Axial Resolution Improvement by Modulated Deconvolution in Fourier Domain Optical Coherence Tomography

5.1 Summary

In this chapter, a novel technique for axial resolution improvement in Fourier domain optical coherence tomography (FDOCT) is presented. The technique is based on the deconvolution of modulated OCT signals. In FDOCT, the real part of the Fourier transform of the interferogram is modulated by a frequency which depends on the position of the interferogram in *k* space. A slight numerical *k* shift, results in a different modulation frequency. By adding two shifted signals, beating can appear in the A-scan. When the amount of shifting is appropriately selected, deconvolution of the resulting depth profile, using suitable modulated kernels, yields a narrower resolution width. A resolution improvement by a factor of ~ 7 can be achieved without the need for a broader bandwidth light source.

5.2 Introduction

In this work, a novel technique that effectively improves the axial resolution of Fourier Domain OCT (FDOCT), without the need to use a light source with a broader bandwidth, is demonstrated. The technique is based on the modulation and subsequent deconvolution of the interferometric OCT signal, a concept adapted to the Fourier domain but bearing some similarities to the method previously demonstrated in Time domain OCT (TDOCT) . The basis of this concept is the summation of more than one A-scans with different carrier frequencies and their subsequent deconvolution with appropriate kernels. This represents a method of achieving super-resolution by oversampling with both A-scans collected at the same sample location. However, the additional information which appears in the form of beating permits modulated deconvolution which significantly increases the resolution of the system. In FDOCT the real part of Fourier transform of each interferogram is modulated by a frequency which depends on the position of the interferogram in the *k* space. If a signal is slightly shifted numerically, the frequency of the real part of the Fourier transforms changes. By adding two shifted interferograms, beating will appear in the A-scans. If the carrier frequencies are appropriately selected, the resulting interferogram will have a narrower width. Subsequent deconvolution, with suitable kernels, provides significant resolution improvement in FDOCT.

5.3. Methodology

The method of resolution improvement, proposed in this paper is based on two principles: (i) the appearance of beating after the addition of two waves of similar but slightly different carrier frequencies, and (ii) the resolution improvement of the OCT images by deconvolution with a set of appropriately chosen kernel functions.

5.3.1 Frequency Summation

In FDOCT the acquired signal from a single scatterer, e.g. a mirror, at position r_0 is:

$$S_{is}(k) = \left[S(k)\cos(2\pi k r_0)\right] \otimes \delta(k - k_x) \qquad (1)$$

where $S(k)$ is the spectrum of the laser source, r_0 is the location of the scatterer, and k_x is the center location of the interferometric signal in the acquisition window which spans from $k_1$to k_N. The real part of the Fourier transform of Eq.1 is:

$$Real\left\{\mathcal{F}\left\{S_{is}(k)\right\}\right\} = R_{is}(r) = \left[R_{ii}(r) \otimes \delta(r - r_0)\right]\cos(2\pi k_x r) \quad (2)$$

where R_{is} is the cross correlation of the source, and R_{ii} is the autocorrelation function. Eq. 2, implies that the real part of the Fourier transform is modulated by a sinusoidal, whose frequency depends on the k position of the interferometric signal, and the period of that sinusoidal is $1/k_x$.

If an interferogram is numerically shifted slightly, the period of the modulation changes. Adding two shifted interferograms, can cause a beating pattern to appear, if the amount of shift is appropriately selected. For example, consider

$$\mathrm{A}_{i1}(\mathrm{r})=\mathrm{Real}\left\{\mathcal{F}\left\{S_{is}(k)\right\}\right\} = R_{is}(r) = \left[R_{ii}(r) \otimes \delta(r - r_0)\right]\cos(2\pi k_{x1} r + \varphi_{i1}) \quad (3)$$

and

$$\mathrm{A}_{i2}(\mathrm{r})=\mathrm{Real}\left\{\mathcal{F}\left\{S_{is}(k)\right\}\right\} = R_{is}(r) = \left[R_{ii}(r) \otimes \delta(r - r_0)\right]\cos(2\pi k_{x2} r + \varphi_{i2}) \quad (4)$$

that are two A-scans from shifted interferograms corresponding to the same single scatterer, where i denotes the number of the A-scan in the image, and $\varphi_{i1,}$ and φ_{i2}, are the initial phases of the real part of the A-scans which are the same for all A-scans, unlike the time domain where each A-scan has a different initial phase. This leads to a quantization of scatterer positions, as we will describe analytically in section 5.3.5. The sum of the two A-scans is:

$$A_i(r) = A_{i1}(r) + A_{i2}(r) = \left[R_{ii}(r) \otimes \delta(r - r_0)\right]\cos\left[\frac{2\pi r(k_{x1} + k_{x2}) + (\varphi_{i1} + \varphi_{i2})}{2}\right]\cos\left[\frac{2\pi r(k_{x1} - k_{x2}) + (\varphi_{i1} - \varphi_{i2})}{2}\right] \quad (5)$$

Filtering the carrier frequency $(k_{x1}+k_{x2})/2$ in Eq. 5, results in a demodulated A-scan with a beating frequency $(k_{x1}-k_{x2})/2$:

$$A_i(r) = \left[R_{ii}(r) \otimes \delta(r - r_0)\right]\cos\left[\frac{2\pi(k_{x1} - k_{x2})r + (\varphi_{i1} - \varphi_{i2})}{2}\right] \quad (6)$$

Fig. 5.1 illustrates the basic principle behind modulated deconvolution. Fig. 5.1 (a) is the acquired backscattered signal from a sample consisting of seven distinct reflections. Fig. 5.1 (b) is an interferogram from the same point but shifted in relation to the first. Characteristic beating patterns appear at each peak after summation of the two interferograms and Fourier transform. They are particularly evident when comparing a single peak from standard and modulated FDOCT in Fig. 5.1 (d).

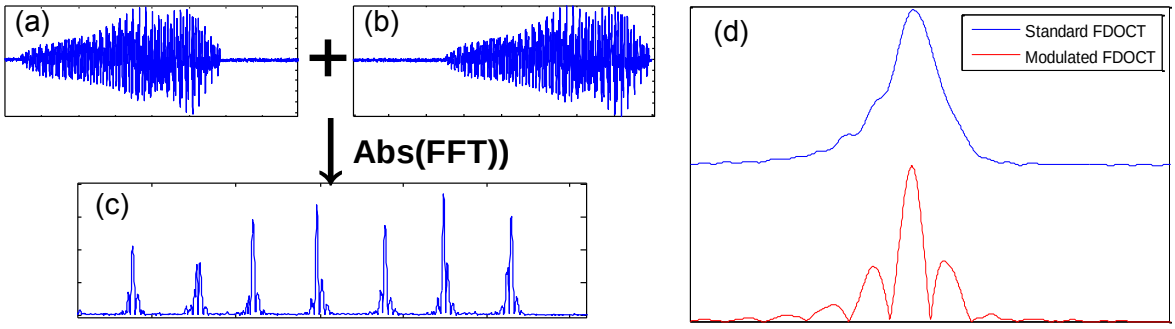

Figure 5.1 (a) Backscattered signal from a sample consisting of seven peaks, (b) signal from the same point shifted in relation to the first, (c) characteristic beating patterns at each peak after summation of two A-scans and FFT, and (d) a single peak from standard FDOCT and modulated FDOCT for comparison.

5.3.2 Selection of Shift Amount

In order to achieve an axial resolution improvement by a factor of greater than two, which is achieved by conventional deconvolution, it is important to choose the amount of shift such that the beating pattern is clearly evident within a coherence length of the source. Therefore, the beating period must be

$$T_{beat} < \frac{l_c}{2} \Rightarrow \frac{1}{(k_{x1} - k_{x2})} < \frac{l_c}{2} \tag{7}$$

where l_c is the axial resolution of the system. If δ_k is the sampling interval of the signal and $\delta_k = \Delta k/N$, where Δk is the spectral width of the interferogram and N the number of points in the spectral width, then the necessary shift, in number of points, is

$$n = \frac{k_{x1} - k_{x2}}{\delta_k} = \frac{1}{\delta_k T_{beat}} \Rightarrow n > \frac{2}{\delta_k l_c} \tag{8}$$

5.3.3 Multiple Discrete Reflectors

In the case of a sample consisting of multiple discrete reflectors, the real part of the depth reflectivity profiles of two shifted A-scans are

$$A_{i1}(r) = \sum_{k=1}^{N} Rs_k \left[h(r - r_k) \otimes R_{ii}(r) \right] \cos(2\pi k_{x1} r + \varphi_{i1}) \tag{9}$$

$$A_{i2}(r) = \sum_{k=1}^{N} Rs_k \left[h(r - r_k) \otimes R_{ii}(r) \right] \cos(2\pi k_{x2} r + \varphi_{i2}) \tag{10}$$

where Rs_k is the reflection coefficients of the k^{th} scatterer, $\otimes$ denotes the convolution operation, and $h(r)$ describes the actual locations of the scattering sites within the sample. Eq. 9 and Eq. 10 are directly related to Eq. 11 and Eq. 12 of the previous chapter which describe the A-scans of a time domain OCT system.

The beating interferogram resulting from the addition of the two A-scans is:

$$A_i(r) = A_{i1}(r) + A_{i2}(r) =$$

$$\sum_{k=1}^{N} Rs_k \left[h(r-r_k) \otimes R_{ii}(r)\right] \cos\left[\frac{2\pi r(k_{x1}+k_{x2}) + (\varphi_{i1}+\varphi_{i2})}{2}\right] \cos\left[\frac{2\pi r(k_{x1}-k_{x2}) + (\varphi_{i1}-\varphi_{i2})}{2}\right] \quad (11)$$

Filtering the carrier frequency $(k_{x1}+k_{x2})/2$ results in a demodulated interferogram with a beating frequency $(k_{x1}-k_{x2})/2$:

$$A_i(r) = \sum_{k=1}^{N} Rs_k \left[h(r-r_k) \otimes R_{ii}(r)\right] \cos\left[\frac{2\pi r(k_{x1}-k_{x2}) + (\varphi_{i1}-\varphi_{i2})}{2}\right] \quad (12)$$

Eq. 12 is analogous to Eq. 14 of the previous chapter which describes an A-scan with beating in a time domain OCT signal. From Eq. 12 we can see that the reflectivity profile can be successfully extracted with a single deconvolution with the modulated source autocorrelation function.

One additional consideration is the performance of the technique in highly scattering samples and in the presence of speckle. The formulation of Eq. 9 and Eq. 10 does not include any assumptions regarding the location of the scatterers (r_k) or the distance between scatterers ($\Delta r = r_{k+1} - r_k$) and, therefore, also applies to cases where Δr is less than the resolution of the system. The envelope of the resulting speckle will not correspond to the source autocorrelation (R_{ii}) but will still be modulated. The process of deconvolution or modulated deconvolution will not have any effect on the speckle amplitude but will result in progressively finer structure. This is particularly evident in Fig. 5.12 and is consistent with the results for time domain OCT in the previous chapter.

5.3.4 Quantization of Position

The modulation method described previously leads to a quantization of position. When modulating with the proposed scheme, the modulation (which is a beating frequency) will be applied to the whole A-scan. This beating frequency will have the

same phase for all A-scans. The phase of the beating $(\varphi_{i1}-\varphi_{i2})/2$ depends only on the position along the interferogram, and is constant from A-scan to A-scan. This means that when two scatterers are very close together, their peaks will be modulated such that the nodes of the beating appear at the same positions for both scatterers. This is shown schematically in Fig. 5.2 (a) and Fig. 5.2 (b). Fig. 5.2 (a) shows the beating frequency (black line) and two closely spaced scatterers (red and blue line) from two adjacent A-scans. When those two A-scans are multiplied with the beating frequency they result in the beating patterns shown in Fig. 5.2 (b) (red and blue line). After deconvolution, the two scatterers of Fig. 5.2 (b) will appear at the same location. This results in scatterers of adjacent A-scans, that are spaced as close as the width of one beat, to appear at the same location. This phenomenon was termed "quantization of position". It appears as an artifact in the image and is particularly evident in angled edges which appear stepped.

To solve this quantization problem, the beating frequency from A-scan to A-scan is changed slightly by shifting the second interferogram by $n+\Delta n$ pixels, in relation to the first, where Δn is a random small number. The result of this operation is shown in Fig. 5.3 (a) and (b). In Fig. 5.3 (a), the red and blue lines are the beating frequencies and the scatterers of two adjacent A-scans. In Fig 5.3 (a) the two beating frequencies now have an imperceptible difference from each other, which can be visualized as a phase difference. Fig. 5.3 (b) (red and blue lines) shows the beating patterns, for the two adjacent A-scans, which results from the multiplication of each A-scans with the corresponding beating frequency. In this case, after deconvolution, the two scatterers can be resolved. However, each modulated A-scan will now have a different phase from the next A-scan, which will be random, and lead to a location shift from the real position of each scetterer. This is a limitation also present in the time domain as described in the previous chapter.

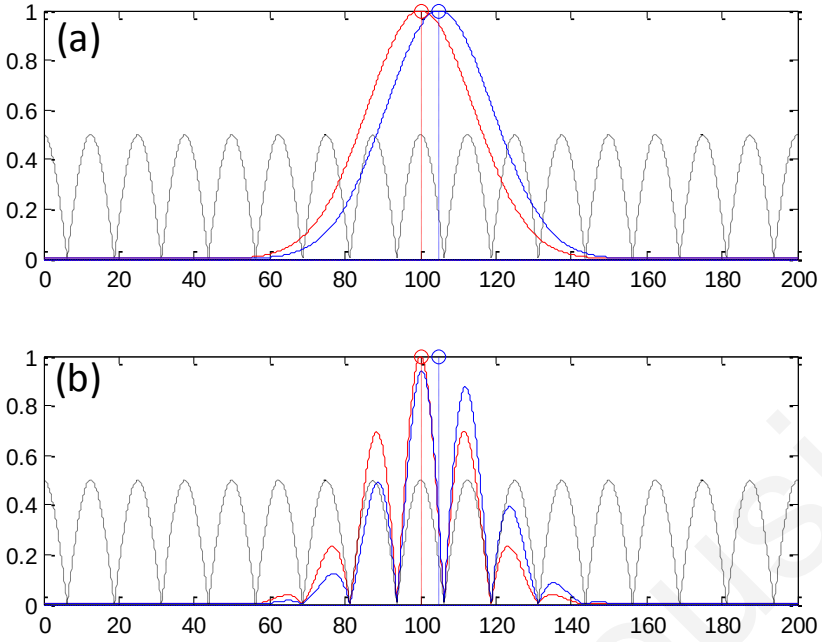

Figure 5.2 (a) black line: Beating frequency which is constant for all A-scans. Blue and red line: two adjacent A-scans. (b) black line: Beating frequency which is constant for all A-scans. Blue and red line: two modulated adjacent A-scans after multiplication with the beating frequency. After deconvolution the two scatterers cannot be resolved

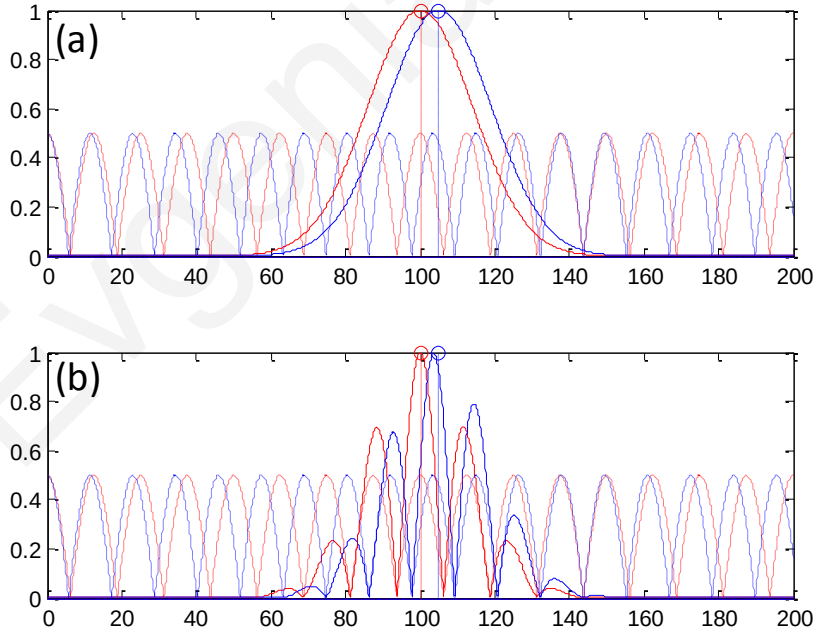

Figure 5.3 (a) blue and red line: Beating frequencies (which are different) and two adjacent A-scans. (b) blue and red line: two modulated adjacent A-scans after multiplication with their corresponding beating frequencies. After deconvolution the two scatterers can be resolved.

5.3.4 Modulated Deconvolution, Resolution Enhancement, and Limitations

The axial resolution of an OCT image can be significantly improved, when modulated A-scans are deconvolved with appropriate kernel functions as also shown in the previous chapter. The equation of modulated deconvolution is derived from Eq. 23 of Chapter 4 (for TDOCT) and, for the case of an FDOCT A-scan, is:

$$Rs_k \hat{h}(r) = h(r) = \sum_{k=1}^{N} h\left(r - r_k - \frac{\Delta\varphi_i - \Delta\varphi_m}{\omega_0} \right) \qquad (13)$$

where $\Delta\varphi_i=\varphi_{i1}-\varphi_{i2}$ is the phase of the i-th modulated A-scan, $\Delta\varphi_m = \varphi_{m1}-\varphi_{m2}$ is the phase of the m-th modulated A-scan from where the single peak, used as kernel for deconvolution is taken and $\omega_0 = 2\pi\frac{(k_{x1}-k_{x2})}{2}$. The factor $\frac{\Delta\varphi_i - \Delta\varphi_m}{\omega_0}$ is the distance shift from the real position of each scatterer.

The Lucy-Richardson algorithm was used for the deconvolution operation in this work. The advantages of this algorithm have been described in Chapter 4.

5.3.4.1 Axial Resolution Improvement with Modulated Deconvolution

By adding two interferograms, from the same sample location and shifted in *k* space, beating will appear in the real part of the Fourier transform and the A-scan will have the appearance depicted in Fig 5.1. As shown, there is already an improvement in the full width half maximum (FWHM) of the central lobe and, therefore, the resolution. The resolution improvement results from the fact that the modulated central lobe is narrower than the equivalent envelope of a standard OCT scan. The degree of the improvement depends on the modulation frequency and, therefore, the shift amount. The FWHM is the width ζ of the central lobe which can be calculated by combining

$$\sin\left(2\pi(\frac{k_{x1}-k_{x2}}{2})(r+\zeta) \right) = 0.5 \Rightarrow 2\pi(k_{x1}-k_{x2})(r+\zeta) = \frac{10\pi}{6} \qquad (14)$$

$$\sin\left(2\pi(\frac{k_{x1}-k_{x2}}{2})r \right) = 0.5 \Rightarrow 2\pi(k_{x1}-k_{x2})r = \frac{2\pi}{6} \qquad (15)$$

which gives:

$$\zeta = \frac{2}{3(k_{x1} - k_{x2})} \tag{16}$$

Deconvolution contributes an additional resolution improvement of a factor of ≥ 2 which results in:

$$\zeta = \frac{1}{3(k_{x1} - k_{x2})} = \frac{1}{3\delta_k n} \tag{17}$$

where δ_k is the sampling interval and n is the shift in number of points. Eq. 17 is equivalent to the Eq. 29 of Chapter 4.

The resolution improvement depends on the beating period since smaller beating periods result in narrower peak widths. Unfortunately the number and amplitude of the sidelobes also increase at the same time.

5.3.4.2 Sidelobe amplitude and location shift

The appearance of sidelobes is an important limitation of this technique. The relative amplitude of the first sidelobe, which is the most severe case in terms of amplitude, is analytically calculated, for the time domain OCT, in Chapter 4 as described by Eq. 31. For the case of fourier domain OCT signal, the sidelobe amplitude is:

$$A_s = A_c e^{-\left(\frac{\pi\Delta k}{2(k_{x1} - k_{x2})\sqrt{\ln 2}}\right)^2} = A_c e^{-\left(\frac{\pi\Delta k}{2\delta_k * n\sqrt{\ln 2}}\right)^2} \tag{18}$$

where Δk is the spectral width of the source, and A_c is the peak amplitude . Eq 18 clearly illustrates that if the shift amount is larger and, therefore, the beating period is smaller, the amplitude of the first sidelobe (A_s) is larger.

Another limitation of the technique is a location shift from peak to peak in the A-scan. As shown earlier, there are differences in phase between A-scans. This leads to different beating patterns at different peak locations resulting in beating nodes at random locations relative to the center of the interferometric peak (Fig.5.4). This introduces a shift in the location of the central lobe. The maximum location error can be derived from the Eq 34 in Chapter 4. For the case of Fourier Domain OCT, the maximum error is:

$$\zeta = \frac{1}{2(k_{x1} - k_{x2})} = \frac{1}{2\delta k * n} \tag{19}$$

which implies that the maximum location shift is inversely proportional to the amount of shift between the two interferograms. The bigger the amount of shift the smaller is the distance error.

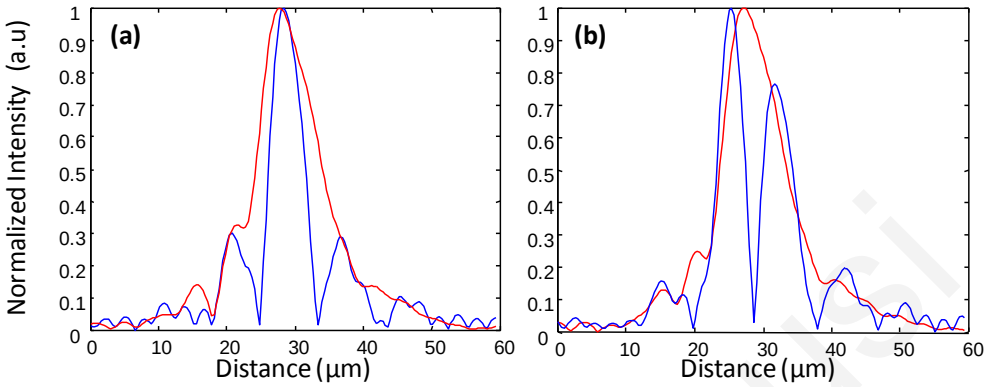

Figure 5.4 Two different beating patterns resulting from two different scatterer locations of Figure 1(c). (a) zero distance shift of the main lobe from the real position. (b), maximum distance shift of the main lobe from the real position. Intensity scales are linear.

As explained above, and illustrated in Fig. 5.4, the location shift and sidelobe amplitude are a direct result of the different beating patterns at different locations. If the signal is deconvolved using as a kernel the beating pattern of Fig.5.4 (a), at locations similar to Fig. 5.4 (b) there will be maximum distance shift and sidelobe amplitude. However, if the beating pattern of Fig. 5.4 (b) is used, the opposite will occur; i.e. the shift and sidelobes will be worse at locations similar to Fig. 5.4(a). If both kernels are used, in successive deconvolutions, and the results are combined by multiplication, then the effect of distance shift and sidelobe amplitude can be significantly reduced. It was noted experimentally that using three such kernels is adequate to minimize these issues. However, even after multiple deconvolutions, some uncertainty, related to the initial phases of each interferogram remains.

5.3.4.3. Design Trade-offs

The tradeoff between sidelobe intensity and number, location shift error, and resolution improvement is obvious from the above discussion. The greater the amount of shift between the interferograms, the smaller the distance shift error and the greater the resolution improvement. However, the number and intensity of sidelobes also increases. A careful selection of shift is necessary to obtain optimal results for resolution improvement while maintaining the sidelobe amplitude and location shift

error within tolerated limits. From simulations and experimental data, it appears that an appropriate choice for the amount of shift is such that the beating pattern has a period of half the coherence length of the system. Such a value, results in a resolution improvement of ~7 and a main sidelobe amplitude 20 dB below the main peak after deconvolution. The sidelobe amplitude is further reduced to 45 dB below the main with the use of three appropriate kernels. As with any design trade-offs, the values chosen will highly depend on system design and imaging study specifics.

5.4. Experimental Method

Fig. 5.5 shows the swept source OCT (SS-OCT) system used in this study. The swept light source (Santec Corporation, Japan) had a 1310 nm center wavelength, 110 nm Scan Range, and 20-kHz scan rate. 90% of the output power was coupled into the sample arm and the remaining 10% into the reference arm. Two circulators were used, in both the reference and sample arms, to redirect the back-reflected light to a 2×2 fiber coupler (50/50 split ratio) for dual balanced detection. The sample arm was scanned by tilting a mirror with a galvanometer. The dynamic range of the system was 85 dB. In the detection arm, the signal collected by the photodetectors was digitized using a 14-bit data acquisition board sampling at 40 M samples/second. The number of data points for each interferogram was 2000. The data acquisition start trigger for the digitizer was generated by the swept source. The depth encoded signal was calculated from the detected fringe signal by zero padding by a factor of 4 (increasing the number of points from 2000 to 8000), k-space resampling and Fast Fourier Transform (FFT). The sampling interval after zero padding and *k* space interpolation was δ_κ = 75.95. The number of pixels we shift the interferogram by is 3000. This value was chosen based on the trade-off discussion of section 5.3.4.3 to provide the best possible results. These values also define the predicted resolution and error. The image range depth was 3.9 mm.

The processing time for an image of size 7,814KB is 33.315338 seconds, and 34.645785 on a 2.5GHz PC using Matlab 2008, for a standard and a modulated OCT image respectively after deconvolution. The most computationally expensive steps are the deconvolution and the FFT steps for both standard and modulated images. The small time difference in the processing of the modulated OCT image is due to shifting and addition of A-Scans step. The time to process a standard OCT image of the same

size but without performing deconvolution is 6.272285 seconds and processing steps include interpolation, 2^{16} point FFT, filtering and display.

Images were acquired with continuous lateral scanning and oversampling in the lateral direction. Since adjacent A-scans were located at less than half the resolution apart, neighboring A-scans were considered to be identical. For every pair, one of them was shifted numerically by an appropriate amount. Beating appeared at each peak after adding the two and taking the real part of the FFT. In order to avoid filtering of the high frequency $(k_{x1}+k_{x2})/2$ in Eq. 13, the absolute value of the FFT of the sum of two interferograms can be taken directly. This ensures a demodulated A-scan with beating at each peak with a beating frequency $(k_{x1}-k_{x2})$. A limitation of this experimental approach is that the acquisition time is twice that of standard OCT, since two A-scans are acquired at each point in the sample.

A reference sample, consisting of three microscope cover slips of ~ 170 μm thickness spaced at ~ 170 μm distance (Fig. 5.6) was used to extract single peak interferograms subsequently used as kernels for the deconvolution. Of the resulting six peaks, three are chosen as kernels based on signal strength (i.e. the reflections with the strongest intensity are selected.) Although it is not obvious that these kernels are the optimum for this procedure, they are adequate to provide acceptable results as explained in Section 5.3.4.3.

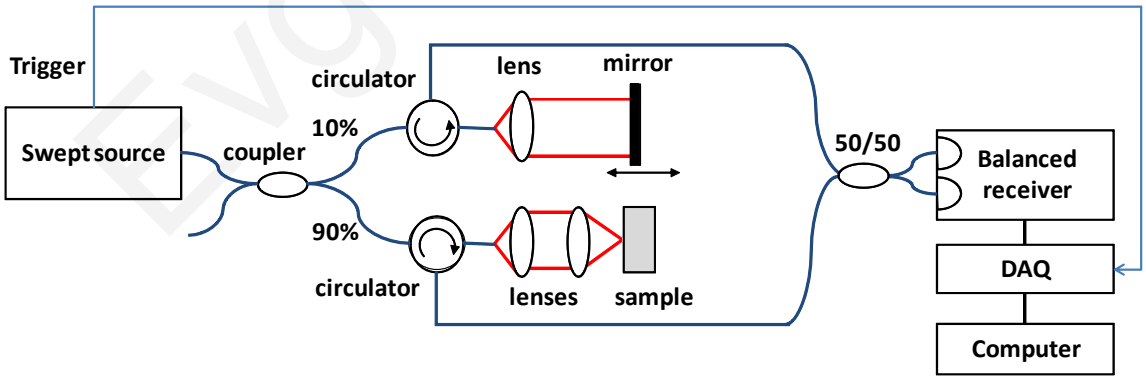

Figure 5.5 Configuration of the experimental swept source OCT system

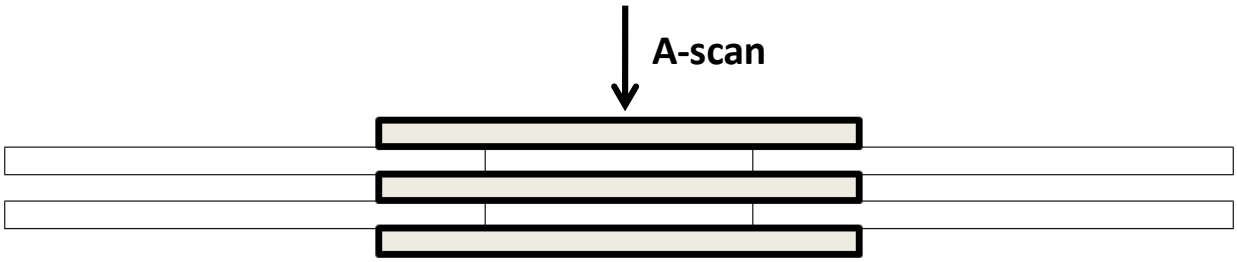

Figure 5.6 Sample, consisting of three microscope cover slips (~ 170 μm thickness, spaced at ~ 170 μm apart), used to collect the interferograms of 6 individual peaks from each A-scan.

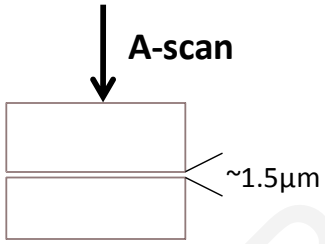

Figure 5.7 Sample consisting of two tightly adjacent microscope slides used to evaluate the resolving power of the proposed technique**.**

5.5 Results

The resolution of a system, as defined by Rayleigh, is its ability to discriminate adjacent structures in an image. In order to demonstrate the improvement in OCT resolution, using the proposed method of modulation, images were acquired from two glass microscope slides tightened together (Fig. 5.7). The two adjacent, inner, glass surfaces, with an air gap of ~ 1.5 μm between them (measured from the modulated OCT A-scans after processing) provided a suitable target for the evaluation of the system's axial resolution. The kernels used for deconvolution are shown in Fig. 5.8(a) and 5.8(b.) They were collected experimentally from the target described in Fig. 5.6. Fig. 5.8(a) shows the kernels used for the deconvolution of a standard OCT image whereas Fig. 5.8(b) shows the kernels for the deconvolution of the modulated image.

Fig. 5.8(c-h) illustrate the results of the proposed method and provide a quantitative measure of the resolution improvement achieved. Fig. 5.8(c) is a plot of a single OCT A-scan showing the reflections from the faces of the two glass microscope slides. The middle peak is the reflection from the two adjacent middle surfaces, a close-up of

which is shown in Fig. 5.8(e). The blue line is a standard OCT scan (with no deconvolution), the red line is the standard OCT scan after deconvolution with the kernels of Fig. 5.8(a), and the black line is the modulated OCT scan after deconvolution with the kernels of Fig. 5.8(b). The two adjacent surfaces were not discernible using standard OCT and appeared as a single peak. Even when deconvolution was performed on the standard OCT signal the two peaks were still not clearly resolved. With modulation and deconvolution the two peaks are unmistakably separated.

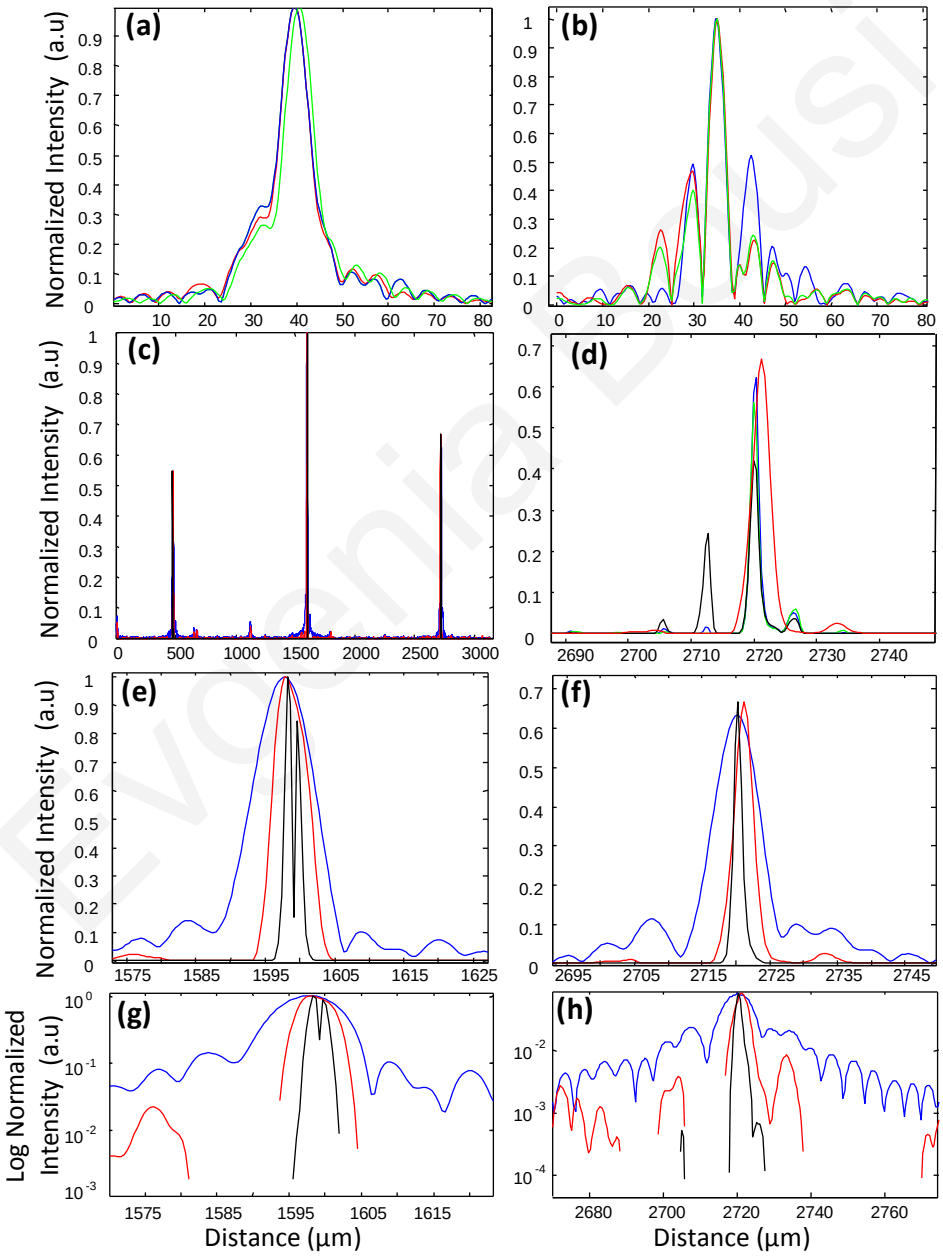

Figure 5.8 Single peaks from (a) a standard OCT interferogram and (b) a modulated OCT interferogram used as kernels for deconvolution. (c) A-scan from standard OCT (blue line), and deconvolution of demodulated A-scans from standard (red line) and modulated OCT (black line) in one

plot for comparison reasons. (d) Intermediate modulated deconvolution results for the first peak of Fig. 5.8(c). (e) and (g) Center peak of Fig. 5.8(c). (f) and (h) Last peak of Fig. 5.8(c). The y axis is normalized to 1 for (a) and (b) and normalized to the highest peak of (c) for (e) and (f).

The improvement in the axial resolution of the system was quantified by examining the reflections from one of the single surfaces, in this case the peak at 2720 μm, a close up of which is shown in Fig. 5.8(f). The standard OCT resolution was measured to be 9.5 μm. After deconvolution of the standard OCT interferogram, the resolution improved to 4.2 μm and, after applying modulated deconvolution, was further improved to 1.4 μm, approximately a seven-fold improvement. This is consistent with the value predicted from the theory. The improvement is further verified by the clear separation (satisfying the Rayleigh criterion of resolution) of the two peaks in Fig. 5.8(e) which are at a distance of ~1.5 μm as estimated from that figure.

The technique was also tested on biological samples. Fig. 5.9(a) shows a small region (0.82 mm x 0.96 mm) of an onion image acquired with standard OCT. Fig. 5.9(b) shows the same region after deconvolution of the standard OCT image. Axial resolution improvement is evident. Fig. 5.9(c) is the onion image after modulated deconvolution. In this image, there is an improvement in resolution which results in the appearance of the characteristic onion double wall structures as evident from the zoomed regions of the same images in Fig. 5.10. The presence of the wall structure is also recognized in Fig. 5.10(d) which is a light microscopy image of onion cells. The distance between the cell membranes, measured from the modulated OCT images, was found to be between 6.8 and 8.2 μm, which is consistent with the literature (6-10 μm corresponding to the thickness of two cell walls.). This is a case of new information, revealed using the proposed technique, which would have been previously unavailable.

Rabbit lung parenchyma was also imaged, *ex vivo*, to further demonstrate the applicability of the proposed technique to biological samples. The tissue was harvested immediately post termination and preserved in phosphate buffered saline at 4 ^{o}C. Imaging was performed within about half an hour after harvesting. The zoomed images in Fig. 5.11 (d, e, and f) illustrate how the additional resolution improvement revealed small alveoli which in standard OCT appeared as highly backreflecting dark areas.

In vivo images of skin were also processed with the proposed algorithm in order to demonstrate the applicability and effects of the technique on highly scattering biological tissues (Fig 5.12). The fine tubular structure of the sweat duct is clearly visible after modulated deconvolution (Fig. 5.12, marked with d). In addition, the effect of the methodology on speckle is also evident (Fig.5.12, marked with s.) As expected from theory and prior work in time domain OCT, the speckle amplitude is not affected but its texture has become considerably finer.

To enhance the visibility of important structures, images should be displayed with high contrast resolution. The minimum and maximum values of the pixels, create a window. Displaying the full range of the window presents the information with very poor contrast. Shrinking the window increases contrast. Changing the center of the window, changes the brightness of the image. In this thesis, for display reasons, the minimum and maximum values for the window are entered manually and are determined in terms of percent of standard deviation from the mean value. By changing the minimum and maximum values of the window, the center of the window is updated automatically, and contrast and brightness can be adjusted appropriately.

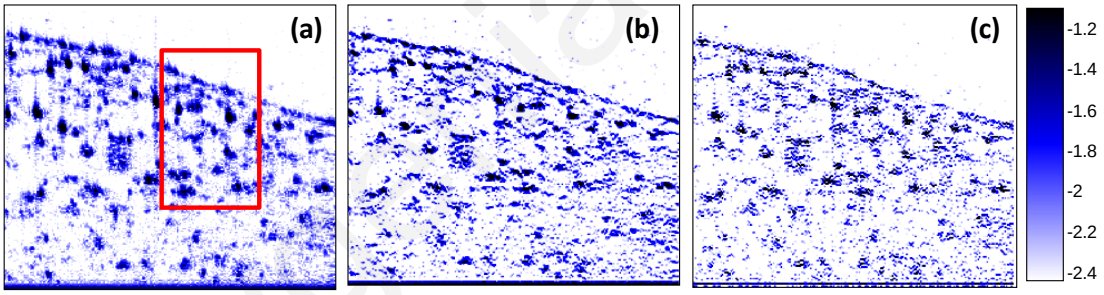

Figure 5.9 (a) Standard OCT image of an onion. (b) Same image after deconvolution. (c) Same data after modulated deconvolution. (Image size: 1.15 mm x 1.35 mm). The area in the red rectangle appears in Fig. 5.10. Intensity scales are normalized log.

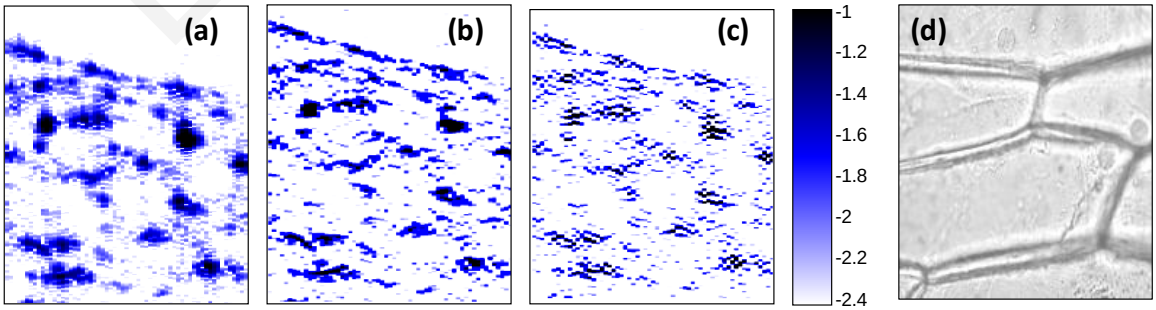

Figure 5.10 (a) Standard OCT image of an onion. (b) Same image after deconvolution. (c) Same data after modulated deconvolution. (d) Light microscopy image of onion cells. (Image size: 0.65 mm x 0.40 mm). Intensity scales are normalized log.

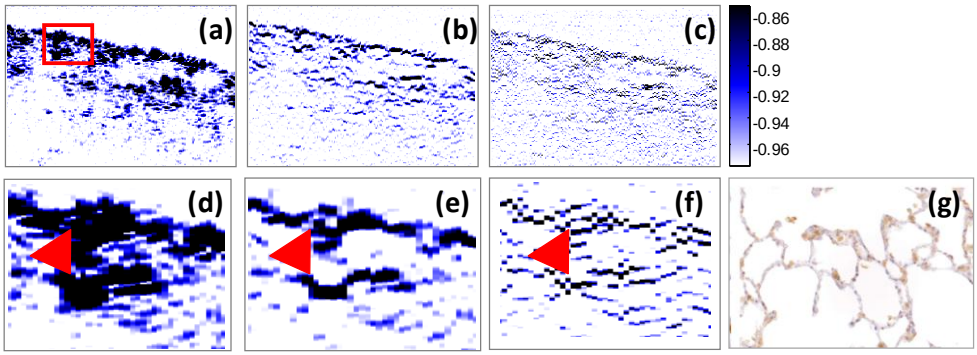

Figure 5.11 (a) Rabbit lung parenchyma imaged *ex vivo* with standard OCT. (b) Same image after deconvolution. (c) Same data after modulated deconvolution. (Image size: 1.2 mm x 0.83 mm). (d – f) Details of images (a)-(c), where small alveoli are indicated by the arrow. (g) Light microscopy image of a section of lung parenchyma from an unrelated site included for reference purposes. Intensity scales are normalized log.

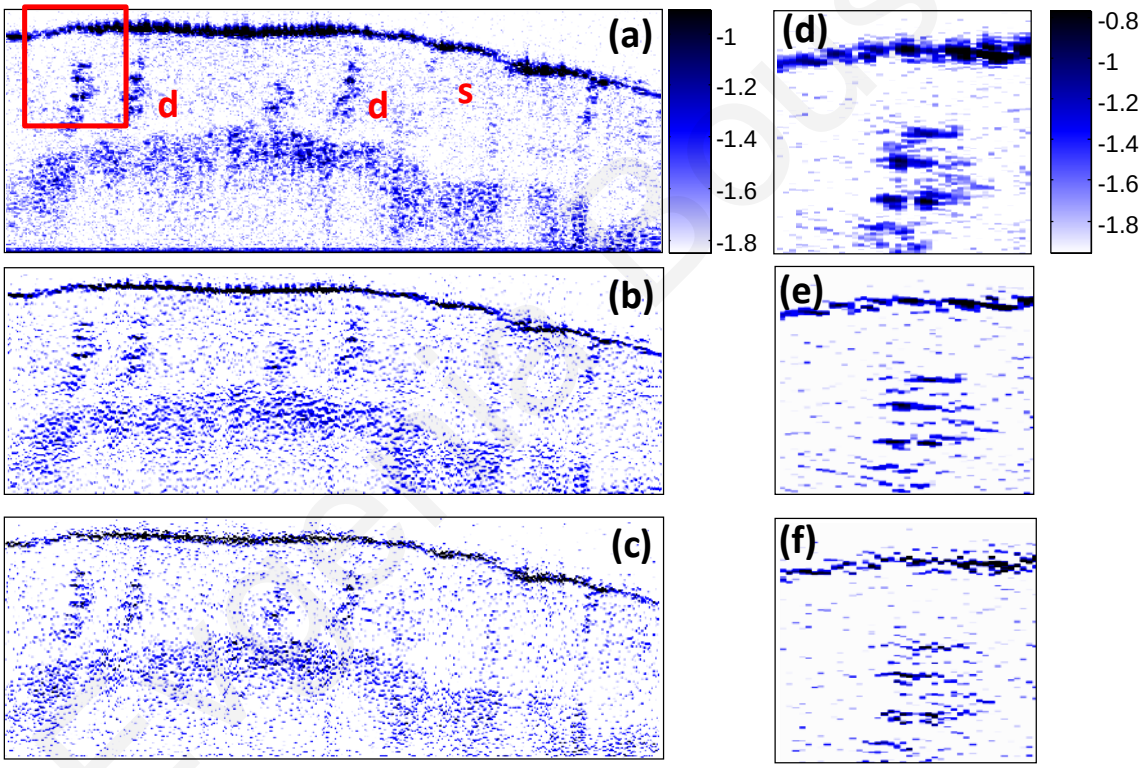

Figure 5.12 (a) *In vivo*, standard OCT, image of skin (finger tip). (Image size: 1.15 mm x 2.7 mm). (b) Close up of the region marked with the rectangle in (a). (c) Same section after deconvolution of the standard OCT image. (d) Same data after modulated deconvolution. The area of the sweat duct (marked with d) clearly exhibits characteristic tubular structure. Areas of speckle are also indicated (marked with s). Intensity scales are normalized log.

To quantitatively assess the image quality in Fig. 5.9, the Signal to Noise Ratio (SNR) and Contrast to Noise Ratio (CNR) were calculated.

$$SNR = 20 * \log_{10}\left\{\frac{I_{max}}{\sigma_b}\right\}, \qquad (20)$$

where I_{max} is the maximum value in the processed image, and σ_b is the standard deviation of the noise in the background. The CNR measures the contrast between a feature of interest and background noise. In the m-th region of interest (ROI), the CNR is defined as:

$$CNR = 10\log_{10}\left\{\frac{\mu_m - \mu_b}{\sqrt{\sigma_m^2 + \sigma_b^2}}\right\}, \qquad (21)$$

where μ_m and σ^2_m denote the mean value and variance of the m-th ROI, respectively, and μ_b and σ^2_b denote the mean value and variance of the background region, respectively. The results are summarized in Table 1.

Applying Lucy-Richardson deconvolution improves the SNR of the image both in the case of regular deconvolution (Fig. 5.7 (b)) and of modulated deconvolution (Fig. 5.7 (c)). This is a result of the property of the Lucy-Richardson algorithm to deblur the intensity of an image therefore concentrating the power near the strong scatterering centers. This finding is consistent with the literature [97]. However, the CNR of the image decreases from 7.86 to 6.93 for the regular deconvolution and to 7.14 for the modulated deconvolution. In both cases, deconvolution decreases the CNR. However, the reduction is less severe for the case of the modulated deconvolution. These results are also consistent with the literature [97].

Table 5.1 Quantitative assessment of SNR and CNR of images in Fig 5.7.

	Figure 6 (a)	*Figure 6 (b)*	*Figure 6 (c)*
SNR(dB)	77.19	77.83	80.21
CNR(dB)	7.86	6.93	7.14

5.6. Conclusion

This chapter demonstrates the application of modulated deconvolution in Fourier domain OCT to achieve superior resolution without the need of a broader bandwidth light source. The resolution improved significantly, in this case by a factor of ~7. By chosing appropriately the shift amount, it is expected that the technique can be applied

for any OCT source(different resolutions, wavelengths, dynamic range) with the same performance. It is also expected that the method will have the same performance if we increase the imaging speed or digital resolution. However an increased imaging speed and digital resolution, results in standard OCT images with better quality and resolution.

Despite the limitations of this very preliminary implementation of modulated deconvolution, it is evident that this technique has the potential to dramatically enhance the resolution of OCT systems. In addition, different forms of encoding can be implemented in the future which will not suffer from the limitations uncovered in these experiments.

Chapter 6
Lateral Resolution Improvement using Oversampling

6.1 Summary

A novel method for lateral resolution improvement of optical coherence tomography (OCT) images, which is independent of the focusing of the delivery optics and the depth of field, is presented in this chapter. This method was inspired by radar range oversampling techniques. It is based on the lateral oversampling of the image and the estimation of the locations of the multiple scatterers which contribute to the signal. The information in the oversampled images is used to estimate the locations of multiple scatterers assuming each contributes a weighted portion to the detected signal, the weight determined by the location of the scatterer and the point spread function (PSF) of the system. *A priori* knowledge of the PSF is not required since there are methods to effectively estimate it from the image. Results of such an approach on laterally oversampled OCT images have shown that it is possible to achieve a ~ 4-fold lateral resolution improvement. Such improvement can be significant, especially in cases where the numerical aperture (NA) of the delivery optics is limited, such as, for example, in the case of ophthalmic imaging where the optics of the eye itself limits the lateral resolution.

6.2 Introduction

In OCT the lateral resolution is fundamentally limited by the focusing of the delivery optics. A high lateral resolution and a wide depth of field (DOF) are mutually exclusive, and this imposes significant limitations. Although a higher effective numerical aperture (NA) enhances the lateral resolution, it limits the DOF which is inversely proportional to the square of the effective NA of the optical system. This limitation becomes even more pronounced in the case of ophthalmic OCT imaging where the delivery of the sample beam is constrained by the optics of the eye. Furthermore, the lateral resolution of OCT systems is not constant. Only a very small range around the focal plane exhibits the desired lateral resolution of the system, and the OCT image in the out-of-focus range is blurred laterally. Adaptive optics [98] or axicon lenses [99] have been used to improve lateral resolution over large scanning depths . It is inevitable however to suffer from aberrations when using AO. Dynamic focus [37] and focus tracking [100] in the sample arm have also been employed. However, special hardware is required which limits the scanning speed and its application in real-time.

A different approach for achieving uniform lateral resolution is the use of inverse scattering [101][102] algorithms. Interferometric synthetic aperture microscopy (ISAM) can achieve depth independent resolution throughout a volume where the focus is fixed at one depth [103]. The disadvantage of this method is the decrease in SNR away from the focus. A two-dimensional numerical method was developed to alleviate the compromise between the lateral resolution and wide depth measurement range in optical coherence tomography (OCT) [104]. However his method is extremely sensitive to the phase stability of the measurements, particularly when *in vivo* imaging is involved and the sample movement is unavoidable.

Deconvolution methods have also been used for lateral resolution improvement by a factor of ~ 2. A non iterative numerical method for laterally superresolving OCT images using a depth dependent PSF was developed [105]. In addition, Gaussian beam deconvolution for lateral resolution improvement have been employed [89][10]. Wiener and Lucy-Richardson OCT image restoration algorithms were implemented and compared to show that Lucy-Richardson algorithms have a better performance [10]. Those deconvolution methods require that the PSF of the system is known. A

new method which proposes an automatic point spread function estimation to deconvolve OCT images was developed, and is based on the discontinuity of information entropy [106].

In this chapter, we present a method for lateral resolution improvement which is independent of the focusing conditions and the depth of field, and is based on lateral oversampling and estimation of the weighted contributions of multiple scatterers. These methods are inspired from radar range oversampling techniques [107]. In such methods, the images are oversampled and the information is used to estimate the locations of multiple scatterers assuming each contributes a weighted portion to the detected signal. *A priori* knowledge of the PSF is not required since it can be estimated from the image. Results from the implementation of methods on laterally oversampled OCT images have shown that it is possible to achieve lateral resolution improvement greater than that achieved with deconvolution.

6.3 Theory

In an OCT system, the output image can be considered as the input image convolved with the PSF of the system. If the input of the system is an infinitely small object then the output will be the lateral PSF of the system. The lateral PSF of an OCT system can be approximated by:

$$h(x,y) = \exp(-2\frac{x^2+y^2}{w^2(z)}) \qquad (1)$$

where w(z) is the beam waist size which is depth dependent and is given by the following equation:

$$w(z) = w_0\sqrt{1+(\frac{z}{z_0})^2} \qquad (2)$$

where w_0 is the beam west radius, which is the minimum beam radius obtained at the focus(z=0), measured between the $1/e^2$ irradiance points (full width at e^{-2} maximum of the intensity), and z is the axial coordinate where $z=z_0$ at the boundary of the confocal region. This means that a laser beam that is focused to a small spot will spread out quickly as it moves away from the focus, while a large-diameter laser beam can stay roughly the same size over a very long distance.

The lateral resolution is determined by the optics of the imaging device, and is equal to the diameter of the focused beam at its narrowest spot:

$$\Delta x = 2w_0 = \frac{4}{\pi}\frac{\lambda_0}{NA} \tag{3}$$

where *NA* is the numerical aperture of the focusing lens, and λ_0 is the center wavelength of the source. High lateral resolution can be obtained by using a large NA and focusing the beam to a small spot size. The lateral resolution is also related to the Rayleigh range *b* which is a measure of the depth of focus, that is:

$$b = \frac{\pi \Delta x^2}{2\lambda} \tag{4}$$

The Rayleigh range is the distance from the focal plane to the point where the light beam diameter has increased by a factor of $\sqrt{2}$. The resolution and depth of focus are shown schematically in Fig. 6.1.

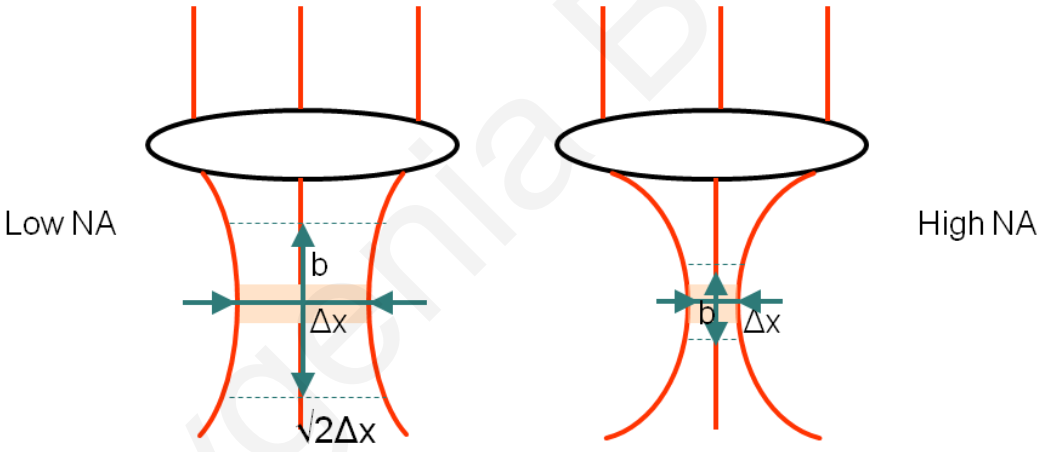

Figure 6.1 Resolution and depth of focus for a high numerical aperture and a low numerical aperture lens.

Given the above relationship it is obvious that improving the lateral resolution produces a decrease in the depth of focus, leading to a significant tradeoff in the design of OCT imaging devices.

6.4. Methodology

If the lateral resolution of an OCT system is Δx then according to the Nyquist sampling theorem the transverse direction is completely determined if the sampling

rate is $\geq 1/(2\Delta x)$. In that case the distance between the centers of two adjacent resolution volumes will be Δx. If the lateral direction is oversampled with a sampling rate of $(L/(2*\Delta x))$, then adjacent resolution volumes overlap and are shifted by $\Delta x/L$. In that way, signals from successive volumes will be correlated in range due to the region shared by adjacent resolution volumes. This is shown schematically in Fig. 6.2 for L= 3.

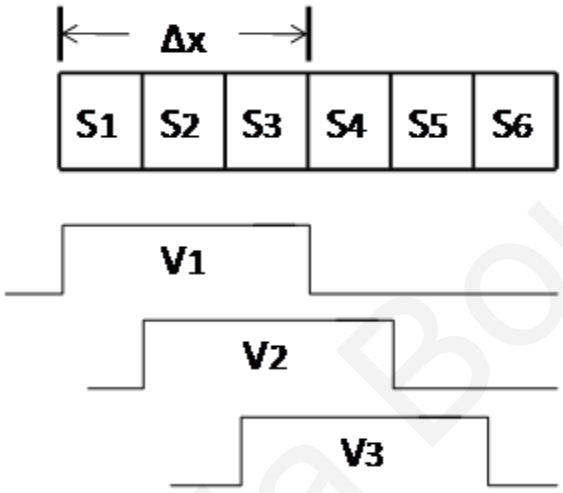

Figure 6.2 A schematic diagram of L=3 lateral oversampling. Each oversampled signal Vi(t) consists of independent signals from L subvolumes (S_i to S_{L+i-1}) **[107]**

We can further assume that in a resolution volume of width Δx there exist L "subvolumes". Each subvolume has a size of $\Delta x/L$. Each OCT resolution volume signal $V_i(t)$, with width Δx, is a weighted contribution of those L independent signals ($S_i(t)$ to ($S_{L+i-1}(t)$), with the weights determined by the PSF of the system. The weighted matrix between high spatial resolution signals and oversampled signals can be represented by the following matrix notation:

$$V(t) = AS(t) \tag{5}$$

where $V(t) = [V_1(t) \;\; V_2(t) \ldots V_L(t)]^T$ is a column vector of oversampling signals from L successively spaced resolution volumes, $S(t) = [S_1(t) \;\; S_2(t) \ldots S_{2L-1}(t)]^T$ is a vector of independent signals (scatterers) at 2L-1 subvolumes within the range covered by L consecutive resolution volumes and the superscript T is the transpose. Moreover,

$A=[a_1\ a_2\ \ ...\ \ a_{2L-1}]$ is a matrix of point spread functions (PSFs) and has a size of $L(2L-1)$, where a_i is a column vector of size L specifying the weights at the i-th subvolume to produce oversampled signals in $V(t)$. In this work, the value of each element in $\boldsymbol{A}$ is assumed to be known.

A simplified ideal, case of Eq. 5 is illustrated in Fig. 6.2, where a rectangular PSF, and an oversampling factor L=3 are considered. Thus, the point spread function has a rectangular shape, and oversampled signals can be represented in the following form:

$$\begin{bmatrix} V_1(t) \\ V_2(t) \\ V_3(t) \end{bmatrix} = \begin{bmatrix} 1 & 1 & 1 & 0 & 0 \\ 0 & 1 & 1 & 1 & 0 \\ 0 & 0 & 1 & 1 & 1 \end{bmatrix} \begin{bmatrix} S_1(t) & S_2(t) & S_3(t) & S_4(t) & S_5(t) \end{bmatrix}^T \tag{6}$$

Each oversampled signal is simply a summation of equally weighted independent signals at those subvolumes contained in one resolution volume. For example, $V_1(t) = S_1(t) + S_2(t) + S_3(t)$. For the case that we have a Gaussian PSF and an oversampling factor of 3 Fig. 6.2 is translated to Fig. 6.3.

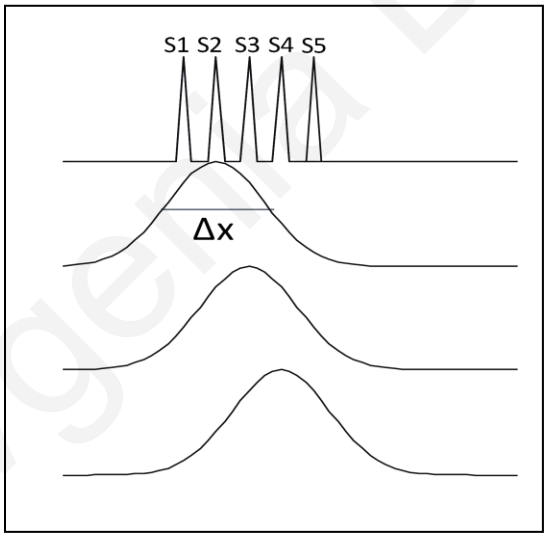

Figure 6.3 A schematic diagram of L=3 lateral oversampling and a Gaussian PSF. Each oversampled signal $V_i(t)$ consists of independent signals from L subvolumes (S_i *to* S_{L+i-1}).

Also, Eq. 6 for Gaussian PSF and oversampling L takes the form of:

$$\begin{bmatrix} V_1 \\ V_2 \\ V_3 \\ \vdots \\ V_L \end{bmatrix} = \begin{bmatrix} a_1 \ ... \ a_{L-1} \ 0 \ ... \ 000 \\ 0\,a_1 \ ... \ a_{L-1} \ 0 \ ... \ 00 \\ 00\,a_1 \ ... \ a_{L-1} \ 0 \ ... \ 0 \\ ..... \\ 0.....a_1 \ ... \ a_{L-1} \end{bmatrix} \begin{bmatrix} S_1 & S_2 & S_3 & \dots & S_{2L-1} \end{bmatrix}^T \tag{7}$$

The sub-resolution volumes S_i can be extracted by direct solution of Eq. 5, that is by multiplication with the inverse of matrix $\boldsymbol{A}$, $S(t) = A^{-1}V(t)$.

6.4.1 Resolution Enhancement using Capon's Method.

Although solving Eq. 5 seems to give an adequate solution to this inverse problem, the method is very sensitive to noise (noise amplification) as will be shown later during the experimental evaluation of this method. A better way to solve this inverse problem and reconstruct the finer resolution signal S_i is to find the optimum weighting for the signal V_i. The Capon method is a simple method which can be used to find the appropriate weight function. This technique was extensively studied in the literature [12],[108] especially as a high-resolution spectral estimation method. The Capon method for spectral estimation is described first, followed by its adaptation to OCT lateral resolution enhancement.

6.4.1.1 Capon Spectral Estimation.

The Capon spectral estimation method is generally a filterbank approach and is a problem of filter design with some specific constraints. The constraints of the Capon method are that the signal at the specific frequency ω is passed unchanged (the gain is unit) and that the output power of the overall frequency domain is minimized. Appropriate choise of these constraints ensures that the Capon filter is actually a matched filter [109],[110].

Let

$$g^H = [g_0 \quad g_1 \quad \cdots \quad g_M] \tag{8}$$

be a finite impulse response (FIR) filter, where ^{H} denotes conjugate transpose. If $x(n)$ is the data row sequence, then the output of the filter at time (n) is given by:

$$y(n) = \sum_{m=0}^{M} g_m x(n-m) = [g_0 \quad g_1 \quad \cdots \quad g_M][x_n \quad x_{n-1} \quad \cdots \quad x_{n-M}]^H \tag{9}$$

If $\boldsymbol{R}$ is the covariance matrix of the data vector $x(n)$:

$$R = E\{x(n)x^H(n)\}, \tag{10}$$

where E is the expectation operator, then the power of the filter output is given by:

$$E\{|y(n)|^2\} = g^H R g \tag{11}$$

The filter frequency response is given by:

$$H(\omega) = \sum_{m-0}^{M} g_m e^{-i\omega m} = g^H a(\omega) \tag{12}$$

where $a(\omega)$ is the steering vector and is :

$$a(\omega) = [1 \quad e^{-i\omega} \quad ... \quad e^{-iM\omega}]^T, \tag{13}$$

and *T* denotes the transpose. The Capon method uses a bandpass filter satisfying:

$$g = \arg\min_g g^H R g, \text{ subject to } g^H a(\omega) = 1$$

Mathematically this is equivalent to minimizing the following cost function:

$$F = g^H R g + \mu[1 - g^H a(\omega)], \tag{14}$$

where μ is a Lagrange multiplier. The minimization of this equation leads to the following solution:

$$g = \frac{R^{-1} a(\omega)}{a(\omega)^H R^{-1} a(\omega)}. \tag{15}$$

6.4.1.2 Adaptation of Capon to Laterally Oversampled OCT.

The oversampled OCT signal, including noise, can be expressed as:

$$V = AS + N \tag{16}$$

where $V = [V_1 \; V_2 \; \ldots V_L]^T$ is the oversampled signal, $S = [S_1 \; S_2 \; \ldots S_{2L-1}]^T$ is the independent high resolution signal, and N is the noise vector. $A=[a_1 \; a_2 \; \ldots a_{2L-1}]$ is a matrix of range wheigting functions (PSFs) and has a size of L(2L-1), where a_i is a column vector of size L specifying the weights at the i-th subvolume to produce oversampling signals V_i.

If $W=[w_1 \; w_2 \; \ldots w_{2L-1}]$ is a matrix of weighted filters with a size of L(2L-1), and each of its columns is the corresponding weighted function, and $X=[X_1 \; X_2 \; \ldots X_{2L-1}]$ is the output of the weighted filter, the following expression is obtained:

$$X_i = w_i V = w_i AS + w_i N = w_i a_1 S_1 + \ldots + w_i \alpha_i S_i + \ldots + w_i a_{2L-1} S_{2L-1} + \sum_{i=1}^{2L-1} w_i N_i$$

(17)

Obviously if the initial high resolution signal Si could be perfectly reconstructed, $w_i a_i$ should be equal to unity while the other terms should be minimum.

These constrain conditions of the capon method can be written as follows:

$$\text{Min}(P) = \min\left(w_i^H R_v w_i\right) \text{ subject to } w_i a_i = 1$$

(18)

Using a Lagrange cost function, the wheighted fiunctions can be easily obtained as follows:

$$w_i = \frac{R_V^{-1} a_i}{a_i^H R_V^{-1} a_i}$$

(19)

where $R_V = E\{VV^H\}$ is the autocorrelation matrix of oversampled signals and each element is: $R_{Vij} = V_i V_j^H$, which is the cross correlation function of the *i*-th and *j*-th oversampled signal.

6.4.2 PSF Estimation

The point-spread function (PSF), could be directly observed with measurement of an infinitesimally small object. However this is experimentally challenging. The PSF can also be extracted from the image using optimization techniques. In this work, the PSF of the system is estimated using the blind deconvolution algorithm.

The blind deconvolution algorithm can be used effectively when no information about the distortion (blurring and noise) of an image is known. The algorithm restores the image and estimates PSF simultaneously. The Richardson-Lucy algorithm is used iteratively. The algorithm is based on maximizing the likelihood of the resulting image being an instance of the original image, *I*, under Poisson statistics. In the case of blind deconvolution the PSF is re-estimated at each iteration. So

$$O^{n+1}(x,y) = \left[\frac{I}{(P * O^n)} * \overline{P} \right](x,y) O^n(x,y) \quad (20)$$

$$P^{n+1}(x,y) = \left[\frac{I}{(P^n * O^n)} * \overline{O^n} \right](x,y) P^n(x,y) \quad (21)$$

Where O^{n+1} and O^n are the current and previous estimate of the desired image, P is the PSF, $P^{n+1}$and P^n are the current and previous estimate of the PSF and $\overline{P}$ and $\overline{O^n}$ are the complex conjugate of P and O^n. I is the original blurred image. The algorithm starts with some estimate for both P and O, and, by constraining these, tries to obtain the original image. The constrains of the algorithm are positivity and stability for both the image and the PSF.

6.5 Experimental Results

The experimental evaluation of the methods described above was performed on OCT images from a phantom of microspheres with an oversampling factor of 28(The lateral resolution of the system was 14μm and 2000 A-scans were taken at a step of 0.5μm). Furthermore, images from skin, with the same oversampling factor were acquired and processed to show the effect of the methods on a biological sample with speckle. Both the two methods, the inverse matrix solution, and weighting method, were applied to images and the results are compared to the original image and to the image after deconvolution.

To enhance the visibility of important structures, images should be displayed with high contrast resolution. The minimum and maximum values of the pixels create a window. Displaying the full range of the window presents the information with very poor contrast. Shrinking the window increases contrast. Changing the center of the window, changes the brightness of the image. In this thesis, for display reasons, the minimum and maximum values for the window are entered manually and are determined in terms of percent of standard deviation from the mean value. By changing the minimum and maximum values of the window, the center of the window is updated automatically, and contrast and brightness can be adjusted appropriately.

The PSF of the system was estimated using blind deconvolution from one depth of the image and the same PSF was used for the whole image. This is adequate for the case of low NA imaging as in the current system. However for high NA lenses, the PSF must be estimated for each depth of the sample. The PSFs from three different depths, as estimated with the blind deconvolution algorithm along with the image that was processed are shown in Fig. 6.4.

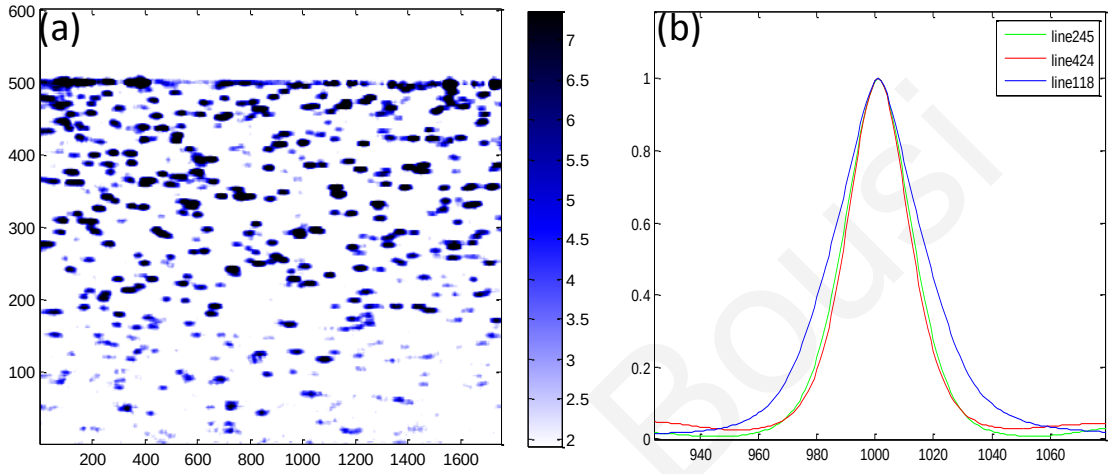

Figure 6.4 (a) The image to be processed. (b) PSFs estimated with the blind deconvolution algorithm from 3 different depths of (a).

6.5.1 Inverse Matrix Solution

Images from a phantom of 6μm microspheres embedded in acrylamide gel, were acquired with an oversampling factor of 28. Subsequently they were processed as described in section 6.4. The matrix A was created using the estimated PSF at line 424(at depth ~300μm below the surface), and the high resolution image was obtained by direct solution of Eq. 5:

$$S(t) = A^{-1}V(t) \tag{22}$$

The results of the inverse matrix solution problem are shown in Fig. 6.5. The comparison of the images reveals that the resolution after processing is improved. However there is significant noise amplification. In order to reduce the noise, filtering must be performed on the images, which in turn reduces the resolution. Another characteristic of this method is that when the SNR of the original image is high, the resolution improvement increases, while when the SNR of the original image is low,

the resolution improvement is limited. This happens because when the SNR of the original image is low, the PSF cannot be estimated accurately, and this leads to a resolution degradation. The FWHM of one peak which corresponds to a microsphere can be measured to quantify the resolution improvement.

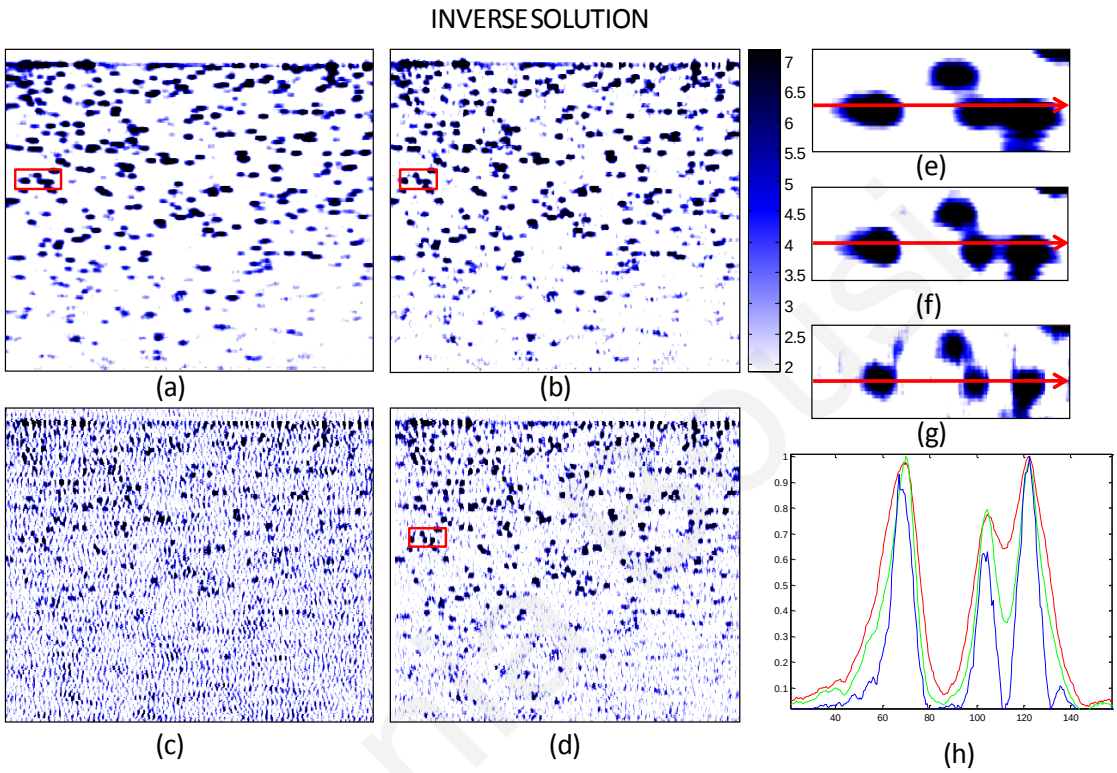

Figure 6.5 (a) Standard OCT image. (b) Deconvolution of Standard OCT image. (c) Inverse solution of OCT image without filtering. (d) Inverse solution of regular OCT image with filtering. (e) Zoomed region of the area in the red rectangle of (a). (f) Zoomed region of the area in the red rectangle of (b). (g) Zoomed region of the area in the red rectangle of (d). (h) The line in the position indicated by the arrow (Red line: Standard OCT. Green line: Deconvoluted OCT. Blue line: Inverse solution)

For standard OCT the FWHM of one peak, taken from a single sphere, is 17.85 μm, for deconvoluted OCT, while the FWHM of the peak from the same sphere is 12.85, and for inverse matrix solution with filtering, the FWHM of the same peak becomes 9.38μm. The resolution can be finer if less filtering is performed on the final image but there will be significantly more noise in the image.

The FWHM of the signal from a peak is the lateral PSF of the system plus the PSF of the sphere. For quantification purposes, considering that the lateral resolution of the system is 14μm as measured with the method described in Chapter 3, then the width of the sphere, at the location of measurement of FWHM, is 17.85-14=3.85μm. By

subtracting from each measurment the PSF of the sphere, the PSF of the system can be estimated and the resolution improvement quantified. Table 2 summarizes the results including the SNR of the images.

Table 6.1 Measurments of PSFs for Standard, Deconvoluted and Inverse Solution OCT images, as well as SNR for Standard, Deconvoluted, and Inverse Solution OCT images**.**

	PSF(μm)	**SNR(no filter)(dB)**	**SNR(filter)(dB)**
Standard OCT	17.85-3.85=14	55.2950	
Deconvoluted OCT	12.85-3.85=9	54.4244	
Inverse Solution	9.38-6=5.53	43.7960	45.6386

The resolution is improved by almost a factor of 2.53 with the inverse solution method. This is a slightly better result than deconvolution where the resolution improves by a factor of 1.55. The main limitation of the inverse solution method is that it is very sensitive to noise and the performance of the method degrades when the original image has low SNR. The computational time for an image of 31.251KB is 20.908199 seconds on a 2.5GHz PC using Matlab 2008 for the inverse matrix solution and 5.433288 seconds for a standard OCT image. This means that the computational time for the inverse matrix solution is approximately 3.8 times greater than for the standard OCT. For the inverse solution the most computational step is the calculation of an inverse matrix, while the standard OCT processing steps are interpolation, filtering, 2^{13} point FFT and display. The processing time for the deconvoluted standard OCT image is 11.661384 seconds.

6.5.2 Weighting Method.

The weighting method was applied to the same oversampled images as before. This method was implement in three different ways.

6.5.2.1 Method 1

In the first method, for each line at a time and repeating for all lines, the value of each sub-resolution volume (pixel) was estimated based on the weights calculated from the

values in a 56 pixel (28μm) neighbourhood around the center pixel. From Fig. 6.6, it is obvious that the weighting method provides excellent results and no noise amplification after processing. This is shown in Table 3 where the SNR of the images is also measured.

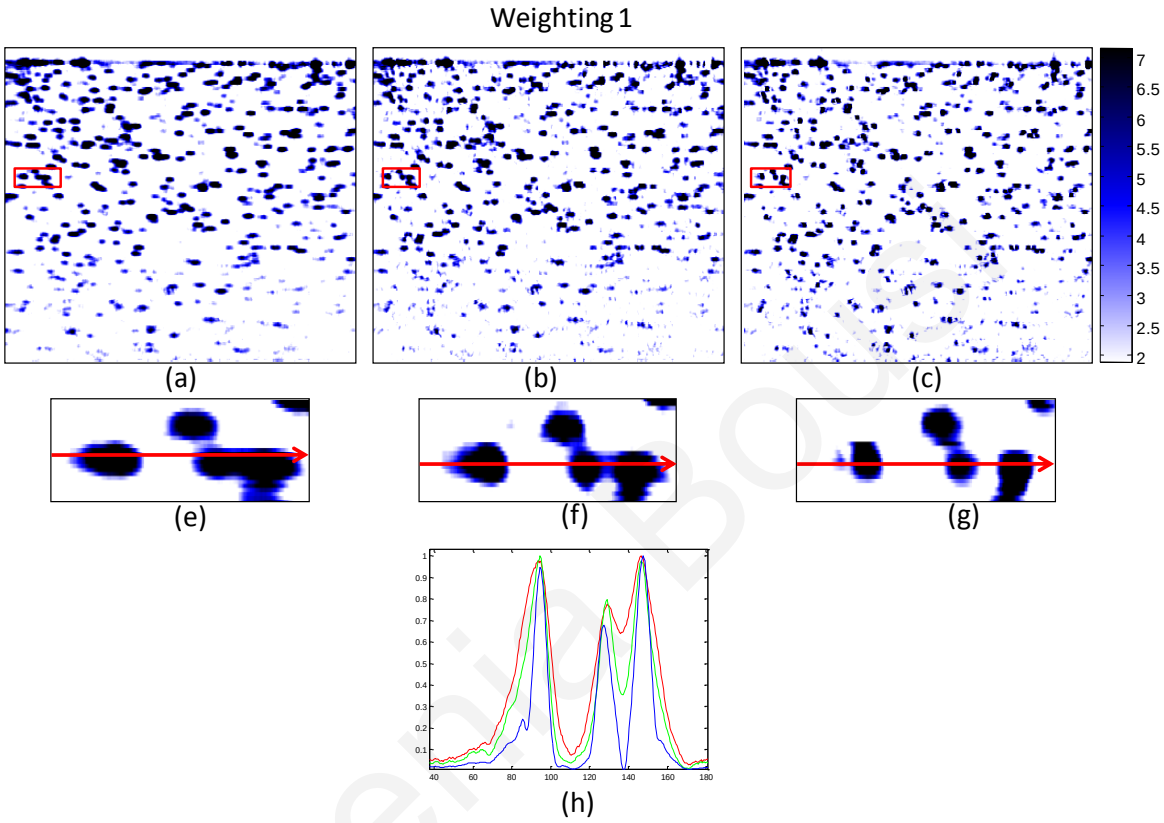

Figure 6.6 (a) the Standard OCT image. (b) The deconvoluted OCT image with the estimated PSF. (c) The OCT image after applying the weighting method. (e) Zoomed region of the area in the red rectangle of (a). (f) Zoomed region of the area in the red rectangle of (b). (g) Zoomed region of the area in the red rectangle of (c). (h) The line in the position indicated by the arrow (Red line: Standard OCT. Green line: Deconvoluted OCT. Blue line: Weighting method 1)

Table 6.2 Measurements of PSFs for Standard OCT, Deconvoluted OCT and Weighting method, as well as SNR for Standard OCT, Deconvoluted OCT, and Weighting method.

	PSF(μm)	**SNR(dB)**
Standard OCT	17.85-3.85=14	55.2950
Deconvoluted OCT	12.85-3.85=9	54.4244
Weighting method	7.6-3.85=3.75	55.6106

Using this method, the resolution was improved by a factor of 3.73. This is a significant improvement compared to deconvolution where the resolution improves by a factor of 1.55. The SNR, after applying the weighting method, is not decreased, so the method does not amplify the noise. However, the resolution improvement using this method is also SNR dependent. This method depends highly on the estimated PSF, and bad estimation, which occurs when the original signal has low SNR, leads to limited resolution improvement.

This method is computationally complex: it takes 1362.615188 seconds to process a 31.251KB image on a 2.5GHz PC using Matlab 2008. This time is approximately 252 times greater than that of a standard OCT image (5.4335288sec). The most computationally intensive step here is the calculation of several inverse matrixes for each line of the image. The processing time for the deconvoluted standard OCT image is 11.661384 seconds.

6.5.2.2 Method 2

In the second method, for each line at a time and for all lines the weights for all sub-volumes were calculated and used to estimate the values of each pixel. The results are shown in the Fig. 6.7 below. Table 4 summarizes the results as in Section 6.5.2.1.

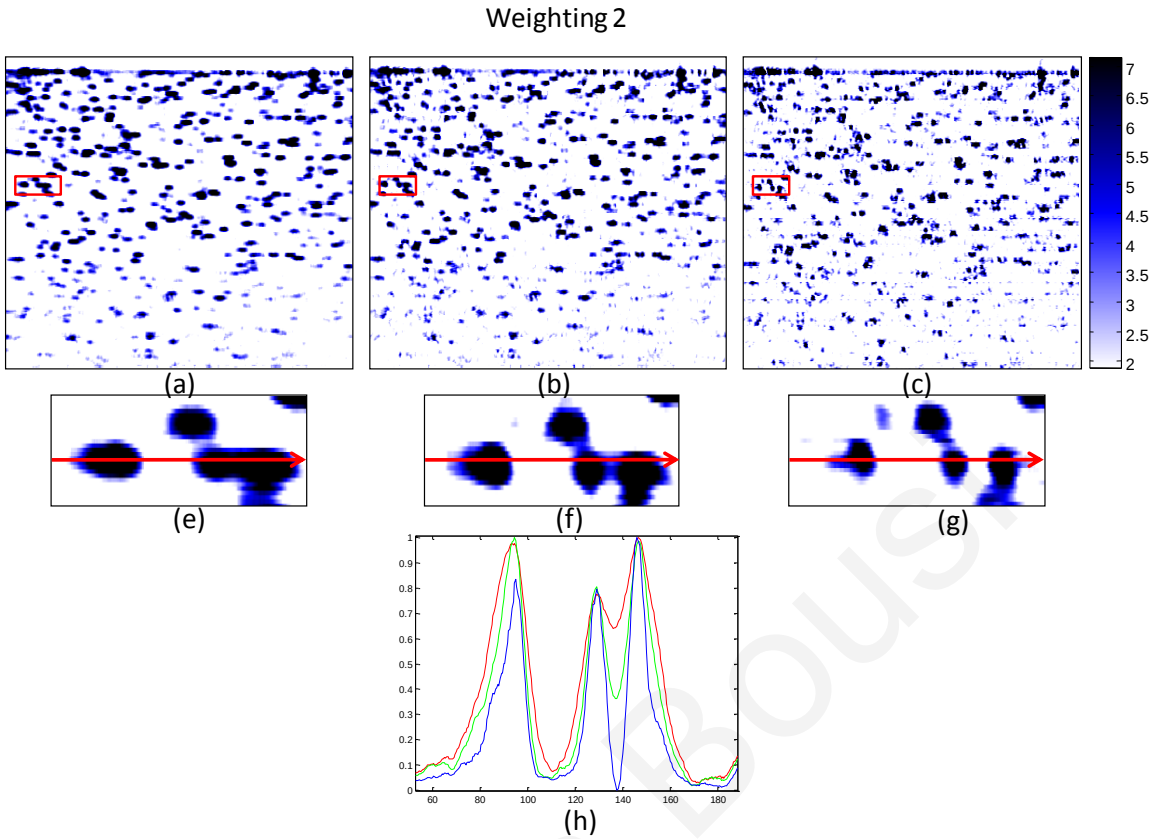

Figure 6.7 (a) the Standard OCT image. (b) The deconvoluted OCT image with the estimated PSF. (c) The OCT image after applying the weighting method. (e) Zoomed region of the area in the red rectangle of (a). (f) Zoomed region of the area in the red rectangle of (b). (g) Zoomed region of the area in the red rectangle of (c). (h) The line in the position indicated by the arrow (Red line: Standard OCT. Green line: Deconvoluted OCT. Blue line: Weighting method 2)

Table 6.3 Measurments of PSFs for Standard OCT, Deconvoluted OCT and Weighting method, as well as SNR for Standard OCT, Deconvoluted OCT, and Weighting method.

	PSF(µm)	**SNR(dB)**
Standard OCT	17.85-3.85=14	55.2950
Deconvoluted OCT	12.85-3.85=9	54.4244
Weighting method	8-3.85=4.15	48.4261

The quantification of results was performed as before and shows (Table 4) that the resolution was improved by a factor of 3.37. This is again a better result compared to

deconvolution where the resolution improved by a factor of almost 1.55. In addition the SNR after the weighting method decreases in this case. This method is the more computationally complex. It takes 8022.512083 seconds to process a 31.251KB image on a 2.5GHz PC using Matlab 2008. This time is approximately 1476 times greater than that of a standard OCT image (5.4335288sec). The most computationally intensive step here is the calculation of an inverse matrix of 2000x2000 data points for each line of the image. The processing time for the deconvolved standard OCT image is 11.661384 seconds.

This method also provides significant resolution improvement. However, the SNR of the image is less that for Method 1. Again, the resolution improvement using this method is also SNR dependent. This method depends highly on the estimated PSF, and bad estimation, which occurs when the original signal has low SNR, leads to limited resolution improvement.

6.5.2.3 Method 3

In the third version of this method, the weights of all pixels for one line are computed and the same weights are used for all lines. The results are shown in Fig. 6.8 below. The quantification of results was performed as before. From Fig. 6.8 and the quantification of Table 5 it is clear that there is significant resolution improvement (2.82x) compared to deconvolution (1.55x). In addition the SNR is not affected in this case. As before, the resolution improvement is SNR dependent. Since the method depends highly on the estimated PSF, bad PSF estimation, which occurs when the original signal has low SNR, leads to limited resolution improvement.

This method is less computationally complex, than the previous two. It requires 30.447060 sec to process a 31.251KB image on a 2.5GHz PC using Matlab 2008. This time is approximately 5.6 times greater than that of a standard OCT image (5.4335288sec). The most computationally intensive step also here is the calculation of an inverse matrix, which is calculated only one time, for this method. This is the reason for this low computational complexity. The processing time for the deconvoluted standard OCT image is 11.661384 seconds.

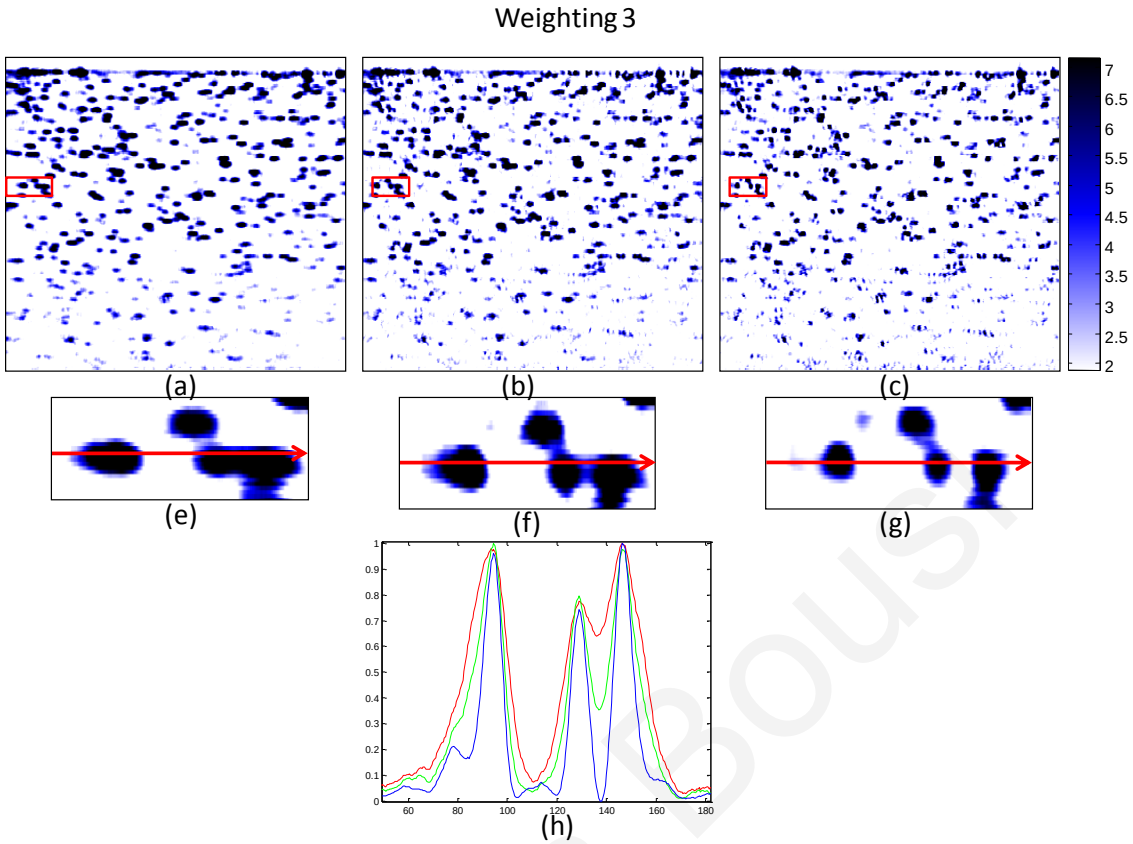

Figure 6.8 (a) the Standard OCT image. (b) The deconvoluted OCT image with the estimated PSF. (c) The OCT image after applying the weighting method. (e) Zoomed region of the area in the red rectangle of (a). (f) Zoomed region of the area in the red rectangle of (b). (g) Zoomed region of the area in the red rectangle of (c). (h) The line in the position indicated by the arrow (Red line: Standard OCT. Green line: Deconvoluted OCT. Blue line: Weighting method 3)).

Table 6.4 Measurments of PSFs for Standard OCT, Deconvoluted OCT and Weighting method, as well as SNR for Standard OCT, Deconvoluted OCT, and Weighting method.

	PSF(μm)	**SNR(dB)**
Standard OCT	17.85-3.85=14	55.2950
Deconvoluted OCT	12.85-3.85=9	54.4244
Weighting method	8.8-3.85=4,95	55.3519

The algorithm was also tested on skin images with the weighting method 1 with the first realization to see the performance of the method on speckle data. The results are shown in Fig. 6.9 below.

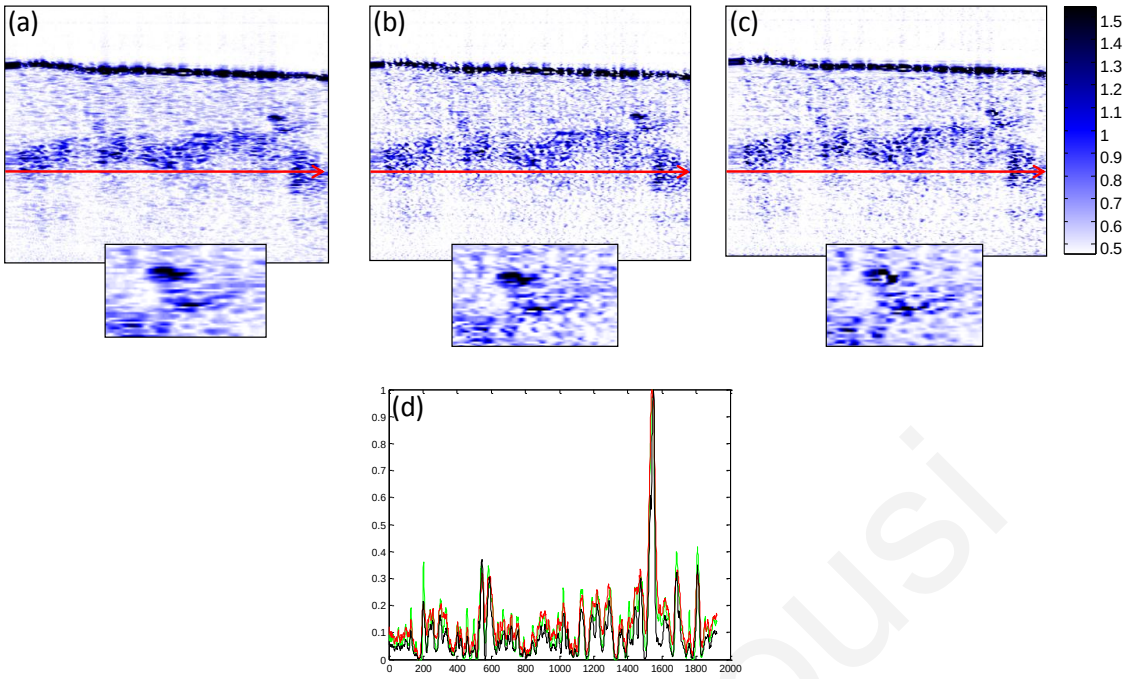

Figure 6.9 (a) Standard OCT image, (b) Deconvoluted OCT image with the estimated PSF. (c) The same image after applying the weighting method. (d) The line at the position indicated by the arrow (Red line: Standard OCT, Green line: deconvoluted OCT, black line: weighting method).

Fig. 6.9 illustrates the resolution improvement also indicating that the speckle is not affected by the method.

6.6 Conclusion

In this chapter, a novel technique is presented for improving the lateral resolution of oversampled OCT images by a factor of as much as 3.73. The improvement is independent of the optics used and the depth of field. Initially the inverse matrix solution is applied to oversampled images. With this method the resolution can be improved significantly but the method suffers from noise amplification, so there is a tradeoff between noise and resolution improvement. By applying the weighting method this tradeoff is alleviated and the resolution improved without noise amplification. Applying the weighting algorithm to overlapped and shifted by one sub-volume regions of the signal, where each region contains L signals (L=oversampling), the resolution improves by a factor of 3.73, and the SNR is not affected. Applying the weighting algorithm for all the signal and computing the weights for each line, the resolution is improved by a factor of 3.37 but there is also a

decrease of the SNR. Finally applying Capon's method to all the signal but computing the weights only one time and applying the same weights for all lines, the resolution improves by a factor of 2.82 and the SNR is not affected. It should be noted that all the methods have better performance compared to deconvolution and that the performance decreases with low SNR. This happens because all methods are highly dependent on the PSF, which is estimated with more accuracy when the original signal has high SNR.

It is expected that all those techniques will perform the same for any OCT source (different resolutions, wavelengths). Also, it is expected that the method will have the same performance if we increase the imaging speed or digital resolution. However an increased imaging speed and digital resolution, results in standard OCT images with better quality and resolution. Also these, methods will perform better if the dynamic range of the OCT system is increased.

In conclusion, the proposed techniques can provide a tool for improving the lateral resolution of any type of OCT device and sample, including ophthalmic imaging systems where the lateral resolution is limited by the optics of the eye itself. As usual, there is a price to pay for the benefits that are obtained. In this case, the price is paid in terms of increased computational complexity, and acquisition time. Oversampling with an oversampling factor of L requires about L times longer acquisition time and L times more computations than without oversampling. Also the computation of a matrix inverse is computationally costly for OCT images. However the weighting method with the third approach requires only one computation of an inverse matrix. Given the progress in current technology, both in OCT imaging speed and GPU-based computational speed, implementation of such techniques is feasible for real time imaging and could provide considerable diagnostic advantages as a result of the significant resolution improvement.

Chapter 7
Conclusion and Future work

7.1 Conclusion

Improvement of the resolution of OCT systems can lead to significant increase in the diagnostic capabilities of the technology. However, such improvements usually come at the cost of complexity, speed, and/or signal quality. In this thesis, novel techniques are presented for improvement of both the axial and lateral resolution without the need for new hardware or a significant limitation of the performance of the system.

The axial resolution of time domain and frequency domain OCT systems can be improved by modulating the PSF of the system and performing deconvolution. The techniques for PSF modulation in both domains were implemented, and an axial resolution improvement by a factor of ~7 was observed when modulation was combined with deconvolution. This resolution enchancment can be achieved without the need of a broader bandwidth light source, and can be applied to any OCT system, providing an opportunity for cellular and sub-cellular imaging.

A technique for lateral resolution improvement, which is based on the lateral oversampling of OCT images, was also implemented. The information in the oversampled images was used to estimate the locations of multiple scatterers, assuming each contributes a weighted portion to the detected signal. These weights depend on the location of the scatterer and the point spread function (PSF) of the system and were estimated using Capon's method. This technique can improve the lateral resolution by a factor of 3.7 independently from the focusing optics. As a result the proposed technique can provide a tool for improving the lateral resolution of any

type of OCT device, including ophthalmic imaging systems where the lateral resolution is limited by the optics of the eye itself.

The techniques developed in this thesis can improve significantly the axial and lateral resolution of OCT systems without the need of further increasing the bandwidth of the light source or restricting the depth of focus. The improvement achieved can surpass the existing state-of-art, as they can be implemented for any OCT system, further increasing the resolution, without any noticeable adverse effect on the system's cost and performance. Furthermore, with these methods we can achieve the same resolution as state of the art OCT systems, but using a significantly lower cost light source.

Current numerical processing techniques for resolution enhancement in OCT include deconvolution techniques, and techniques for digitally reshaping the source spectra to known modes. In addition interferometric synthetic aperture microscopy (ISAM) can achieve depth independent lateral resolution throughout a volume where the focus is fixed at one depth [103]. All of these methods can achieve a resolution improvement by a factor of no more than two and a decrease in SNR away from the focus is observed for the ISAM method. The methods used in this thesis can improve the resolution by a factor of much greater than two, while the SNR is not decreased.

In addition, even the highest axial and transverse resolution that might be achieved in the future may not enable visualization of certain morphological features if the contrast is insufficient. So for clinical applications further improvements are needed. Techniques for contrast enhancement should be implemented to differentiate cellular and subcellular features and provide better diagnosis. The difference in tissue scattering and absorption provides structural contrast for OCT. Typical OCT systems measure the distribution of backscattered or reflected light intensity. As is well known from microscopy, intensity based imaging frequently suffers from a poor image contrast, making direct tissue differentiation difficult. Some tissues can change other properties of the light, such as its polarization state, its spectrum, or its phase. Similar to microscopy, these phenomena can be used to enhance image contrast in OCT, and to also obtain quantitative measurements. Image contrast can be enhanced by the use of polarization sensitive OCT, phase contrast OCT, or by using spectroscopic OCT. In addition to these endogenous contrast mechanisms, exogenous contrast agents are being developed for OCT, such as engineered microspheres. These microspheres can

be targeted to cell receptors and change the optical scattering or absorption characteristics in selected regions, providing molecular specific contrast [111]. Moreover by choosing appropriately the center wavelength and bandwidth of the light source used for OCT, the resolution and contrast, as well as penetration may be optimized according to the imaging procedure and medical application.

The best developed clinical OCT applications are those focusing on ophthalmic, cardiovascular, and gastrointestinal imaging. In addition, applications in areas such as neurology, gynecology (for the diagnosis of ovarian cancer) and urology (for the diagnosis of prostate cancer) are advancing rapidly. Increasing resolutions to cellular and subcellular level are important for the diagnosis of early neoplasias as well as other applications. Tissue contrast, the ability to differentiate morphology and image quality are highly dependent on the specific structures being imaged. Given that cancer is a highly heterogeneous disease, characterized by a spectrum of morphologic changes, we expect that the viability of OCT will be highly dependent on the details of the specific clinical application.

A clinical trial of OCT is applied in the gastrointestinal tract [112]. Patients with Barrett's esophagus, a condition of cellular metaplasia that can progress to esophageal adenocarcinoma, typically undergo regular endoscopic surveillance and biopsy to monitor for dysplastic changes. A number of studies have been conducted to determine the feasibility of using OCT imaging to identify suspicious lesions, including a recent blind clinical trial that showed an accuracy of 78% for the OCT detection of dysplasia in patients with Barrett's esophagus [113]. Improvements in system resolution can increase the accuracy of this OCT application, making it a strong candidate for future clinical adoption.

More research remains to be done and numerous clinical studies must be performed to determine in which clinical situations OCT can play a role. However, the unique capabilities of OCT imaging suggest that it has the potential to significantly impact the diagnosis and clinical management of many diseases and improve patient prognosis. In addition, OCT can be a powerful research tool for applications in many areas, including developmental biology, where non-destructive, serial imaging, on the same samples can offer new insights and significant cost and time advantages. For all the cases, the ability to image at cellular and sub-cellular resolution will not only

enhance the spectrum of pathology that can be imaged, but also improve sensitivity and specificity.

7.2 Future Work

In the future, methods to improve the performance of the techniques, described in this thesis, will be investigated. For example, methods for side-lobe reduction can be developed as well as new encoding schemes which will not suffer from the limitations described.

Advanced motion corrections techniques which are used to correct motion artefacts in OCT, due to movement of the sample during scanning, can also be implemented to avoid the problem of distance shift faced in this thesis. Image quality can be also improved by the use of these algorithms.

In addition, Capon's method for lateral resolution can be applied also for axial resolution improvement by oversampling in a time domain OCT system. This method cannot be applied in a frequency domain OCT system since increasing the number of samples in the Fourier domain, increases the range and A-Scan oversampling cannot be achieved. However, Capon's method, instead of FFT, can be applied to an A-Scan for spectral estimation as it is shown to result in better resolution.

Other techniques can also be investigated. For example, the MUSIC algorithm can be applied to Fourier domain interferograms to estimate the frequency content with higher resolution than the FFT Also, pupil-plane phase masks also can be designed to completely reshape the spatial light intensity distribution providing super-resolution in the axial or transverse directions.

The visualization scheme is very important for cellular and sub-cellular level imaging, and further image analysis, which is needed, to extract features, and quantify objects and patterns in image data and obtain answers to meaningful biological questions. In this thesis a simple method to display the images is used, which is based on thresholding the minimum and maximum intensity values in the image. However better visualization algorithms can be employed in the future to enhance the contrast resolution of the images and provide the best presentation for visualization of different image features.

7.3 Contributions of the Thesis

The main contribution of this thesis is the development of a new framework for axial and lateral resolution improvement of OCT systems. These methods are inexpensive and easy to implement, providing the potential of cellular and sub-cellular imaging and improved diagnostic capabilities. In particular, the original contributions of this work can be summarized as follows:

1. The theoretical framework for axial resolution improvement of time domain OCT systems has been developed. The methodology depends on modulation, summation, and deconvolution in the time domain.
2. Experimental verification of the above method has been provided. The improvement was approximately a factor of 7 and does not require a broader bandwidth light source.
3. The theoretical framework for axial resolution improvement of Fourier domain OCT systems has been developed. The methodology is the Fourier equivalent of the time domain technique where shifting, summation, and deconvolution can lead to improved resolution.
4. Experimental verification of the above method has been provided. The improvement was also approximately a factor of 7 and does not require a broader bandwidth light source as well.
5. Inverse solution and Capon's method were adapted to OCT data and used to improve the lateral resolution by a factor of 3.7 (compared to 1.55 for deconvolution). The improvement was independent of the focusing optics and the depth of focus was not restricted. This is particularly important for systems where the lateral resolution is limited, such as ophthalmic imaging systems where the resolution is limited by the optics of the eye itself.

Bibliography

[1] D. Huang, E. A. Swanson, C. P. Lin, J. S. Schuman, W. G. Stinson, W. Chang, M. R. Hee, T. Flotte, K. Gregory, C. A. Puliafito, and A. Et, "Optical Coherence Tomography," *Science*, vol. 254, no. 5035, pp. 1178–1181, Nov. 1991.

[2] A. F. Fercher, C. K. Hitzenberger, W. Drexler, G. Kamp, and H. Sattmann, "In vivo optical coherence tomography," *Am. J. Ophthalmol.*, vol. 116, no. 1, pp. 113–114, Jul. 1993.

[3] E. A. Swanson, J. A. Izatt, M. R. Hee, D. Huang, C. P. Lin, J. S. Schuman, C. A. Puliafito, and J. G. Fujimoto, "In vivo retinal imaging by optical coherence tomography," *Opt. Lett.*, vol. 18, no. 21, pp. 1864–1866, Nov. 1993.

[4] J. G. Fujimoto, "Optical coherence tomography for ultrahigh resolution in vivo imaging," *Nature Biotechnology*, vol. 21, no. 11, pp. 1361–1367, 2003.

[5] J. G. Fujimoto, M. E. Brezinski, G. J. Tearney, S. A. Boppart, B. Bouma, M. R. Hee, J. F. Southern, and E. A. Swanson, "Optical biopsy and imaging using optical coherence tomography," *Nature Medicine*, vol. 1, no. 9, pp. 970–972, Sep. 1995.

[6] A. F. Fercher, W. Drexler, C. K. Hitzenberger, and T. Lasser, "Optical coherence tomography - principles and applications," *Reports on Progress in Physics*, vol. 66, no. 2, pp. 239–303, Feb. 2003.

[7] P. A. JANSSON, R. H. HUNT, and E. K. PLYLER, "Resolution Enhancement of Spectra," *J. Opt. Soc. Am.*, vol. 60, no. 5, pp. 596–599, May 1970.

[8] A. N. Tikhonov and V. I. Arsenin, *Solutions of ill-posed problems*. Winston, 1977.

[9] L. B. Lucy, "An iterative technique for the rectification of observed distributions," *The Astronomical Journal*, vol. 79, p. 745, Jun. 1974.

[10] Y. Liu, Y. Liang, G. Mu, and X. Zhu, "Deconvolution methods for image deblurring in optical coherence tomography," *J. Opt. Soc. Am. A*, vol. 26, no. 1, pp. 72–77, Jan. 2009.

[11] R. Schmidt, "Multiple emitter location and signal parameter estimation," *IEEE Transactions on Antennas and Propagation*, vol. 34, no. 3, pp. 276 – 280, Mar. 1986.

[12] J. Capon, "High-resolution frequency-wavenumber spectrum analysis," *Proceedings of the IEEE*, vol. 57, no. 8, pp. 1408 – 1418, Aug. 1969.

[13] B. Bouma, G. J. Tearney, S. A. Boppart, M. R. Hee, M. E. Brezinski, and J. G. Fujimoto, "High-resolution optical coherence tomographic imaging using a mode-locked Ti:Al2O3 laser source," *Opt. Lett.*, vol. 20, no. 13, pp. 1486–1488, Jul. 1995.

[14] B. E. Bouma, G. J. Tearney, I. P. Bilinsky, B. Golubovic, and J. G. Fujimoto, "Self-phase-modulated Kerr-lens mode-locked Cr:forsterite laser source for optical coherence tomography," *Opt. Lett.*, vol. 21, no. 22, pp. 1839–1841, Nov. 1996.

[15] J. G. Fujimoto, C. Pitris, S. A. Boppart, and M. E. Brezinski, "Optical Coherence Tomography: An Emerging Technology for Biomedical Imaging and Optical Biopsy," *Neoplasia*, vol. 2, no. 1–2, pp. 9–25, Jan. 2000.

[16] M. E. Brezinski, G. J. Tearney, B. E. Bouma, J. A. Izatt, M. R. Hee, E. A. Swanson, J. F. Southern, and J. G. Fujimoto, "Optical coherence tomography for

optical biopsy. Properties and demonstration of vascular pathology," *Circulation*, vol. 93, no. 6, pp. 1206–1213, Mar. 1996.
[17] G. J. Tearney, M. E. Brezinski, B. E. Bouma, S. A. Boppart, C. Pitris, J. F. Southern, and J. G. Fujimoto, "In Vivo Endoscopic Optical Biopsy with Optical Coherence Tomography," *Science*, vol. 276, no. 5321, pp. 2037–2039, Jun. 1997.
[18] Fujimoto, J. G. 2002. Optical Coherence Tomography: Introduction (Chapter 1) In Handbook of Optical Coherence Tomography. ed. B. E. Bouma and G. J. Tearney. New York, USA.: Marcel Dekker, Inc., .
[19] R. C. Youngquist, S. Carr, and D. E. N. Davies, "Optical coherence-domain reflectometry: a new optical evaluation technique," *Opt. Lett.*, vol. 12, no. 3, pp. 158–160, Mar. 1987.
[20] R. P. N. H. H. Gilgen, "Submillimeter optical reflectometry," *Lightwave Technology, Journal of*, no. 8, pp. 1225 – 1233, 1989.
[21] A. F. Fercher, K. Mengedoht, and W. Werner, "Eye-length measurement by interferometry with partially coherent light," *Opt. Lett.*, vol. 13, no. 3, pp. 186–188, Mar. 1988.
[22] C. K. Hitzenberger, "Optical measurement of the axial eye length by laser Doppler interferometry," *Invest. Ophthalmol. Vis. Sci.*, vol. 32, no. 3, pp. 616–624, Mar. 1991.
[23] D. Huang, J. Wang, C. P. Lin, C. A. Puliafito, and J. G. Fujimoto, "Micron-resolution ranging of cornea anterior chamber by optical reflectometry," *Lasers Surg Med*, vol. 11, no. 5, pp. 419–425, 1991.
[24] C. K. Hitzenberger, "Measurement of corneal thickness by low-coherence interferometry," *Appl. Opt.*, vol. 31, no. 31, pp. 6637–6642, Nov. 1992.
[25] X. Clivaz, F. Marquis-Weible, R. P. Salathe, R. P. Novak, and H. H. Gilgen, "High-resolution reflectometry in biological tissues," *Opt. Lett.*, vol. 17, no. 1, pp. 4–6, Jan. 1992.
[26] J. M. Schmitt, A. Knuttel, and R. F. Bonner, "Measurement of optical properties of biological tissues by low-coherence reflectometry," *Appl. Opt.*, vol. 32, no. 30, pp. 6032–6042, Oct. 1993.
[27] G. J. Tearney, B. E. Bouma, and J. G. Fujimoto, "High-speed phase- and group-delay scanning with a grating-based phase control delay line," *Opt. Lett.*, vol. 22, no. 23, pp. 1811–1813, Dec. 1997.
[28] A. Rollins, S. Yazdanfar, M. Kulkarni, R. Ung-Arunyawee, and J. Izatt, "In vivo video rate optical coherence tomography," *Opt. Express*, vol. 3, no. 6, pp. 219–229, 1998.
[29] P. Herz, Y. Chen, A. Aguirre, J. Fujimoto, H. Mashimo, J. Schmitt, A. Koski, J. Goodnow, and C. Petersen, "Ultrahigh resolution optical biopsy with endoscopic optical coherence tomography," *Opt. Express*, vol. 12, no. 15, pp. 3532–3542, Jul. 2004.
[30] M. R. Hee, C. A. Puliafito, C. Wong, J. S. Duker, E. Reichel, B. Rutledge, J. S. Schuman, E. A. Swanson, and J. G. Fujimoto, "Quantitative assessment of macular edema with optical coherence tomography," *Arch. Ophthalmol.*, vol. 113, no. 8, pp. 1019–1029, Aug. 1995.
[31] S. A. Boppart, B. E. Bouma, C. Pitris, J. F. Southern, M. E. Brezinski, and J. G. Fujimoto, "In vivo cellular optical coherence tomography imaging," *Nature Medicine*, vol. 4, no. 7, pp. 861–865, Jul. 1998.

[32] W. Drexler, U. Morgner, F. X. Kartner, C. Pitris, S. A. Boppart, X. D. Li, E. P. Ippen, and J. G. Fujimoto, "In vivo ultrahigh-resolution optical coherence tomography," *Opt. Lett.*, vol. 24, no. 17, pp. 1221–1223, 1999.
[33] W. Drexler, U. Morgner, R. K. Ghanta, F. X. Kärtner, J. S. Schuman, and J. G. Fujimoto, "Ultrahigh-resolution ophthalmic optical coherence tomography," *Nat Med*, vol. 7, no. 4, pp. 502–507, Apr. 2001.
[34] I. Hartl, X. D. Li, C. Chudoba, R. K. Ghanta, T. H. Ko, J. G. Fujimoto, J. K. Ranka, and R. S. Windeler, "Ultrahigh-resolution optical coherence tomography using continuum generation in an air?silica microstructure optical fiber," *Opt. Lett.*, vol. 26, no. 9, pp. 608–610, May 2001.
[35] K. Bizheva, B. Povazay, B. Hermann, H. Sattmann, W. Drexler, M. Mei, R. Holzwarth, T. Hoelzenbein, V. Wacheck, and H. Pehamberger, "Compact, broad-bandwidth fiber laser for sub-2-microm axial resolution optical coherence tomography in the 1300-nm wavelength region," *Opt Lett*, vol. 28, no. 9, pp. 707–709, May 2003.
[36] S. Bourquin, A. Aguirre, I. Hartl, P. Hsiung, T. Ko, J. Fujimoto, T. Birks, W. Wadsworth, U. Bunting, and D. Kopf, "Ultrahigh resolution real time OCT imaging using a compact femtosecond Nd:Glass laser and nonlinear fiber," *Opt. Express*, vol. 11, no. 24, pp. 3290–3297, Dec. 2003.
[37] Y. Wang, Y. Zhao, J. S. Nelson, Z. Chen, and R. S. Windeler, "Ultrahigh-resolution optical coherence tomography by broadband continuum generation from a photonic crystal fiber," *Opt. Lett.*, vol. 28, no. 3, pp. 182–184, Feb. 2003.
[38] W. Drexler, "Ultrahigh-resolution optical coherence tomography," *Journal of Biomedical Optics*, vol. 9, no. 1, pp. 47–74, 2004.
[39] J. A. Izatt, M. R. Hee, G. M. Owen, E. A. Swanson, and J. G. Fujimoto, "Optical coherence microscopy in scattering media," *Opt. Lett.*, vol. 19, no. 8, pp. 590–592, Apr. 1994.
[40] J. A. Izatt, H.-W. Wang, M. Kulkarni, M. I. Canto, and M. V. Sivak, "Optical coherence microscopy in gastrointestinal tissues," in *Lasers and Electro-Optics, 1996. CLEO '96., Summaries of papers presented at the Conference on*, 1996, pp. 56 –57.
[41] A. D. Aguirre, P. Hsiung, T. H. Ko, I. Hartl, and J. G. Fujimoto, "High-resolution optical coherence microscopy for high-speed, in vivo cellular imaging," *Opt. Lett.*, vol. 28, no. 21, pp. 2064–2066, Nov. 2003.
[42] M. Choma, M. Sarunic, C. Yang, and J. Izatt, "Sensitivity advantage of swept source and Fourier domain optical coherence tomography," *Opt. Express*, vol. 11, no. 18, pp. 2183–2189, 2003.
[43] J. F. de Boer, B. Cense, B. H. Park, M. C. Pierce, G. J. Tearney, and B. E. Bouma, "Improved signal-to-noise ratio in spectral-domain compared with time-domain optical coherence tomography," *Opt. Lett.*, vol. 28, no. 21, pp. 2067–2069, Nov. 2003.
[44] R. Leitgeb, C. Hitzenberger, and A. Fercher, "Performance of fourier domain vs. time domain optical coherence tomography," *Opt. Express*, vol. 11, no. 8, pp. 889–894, Apr. 2003.
[45] A. F. Fercher, C. K. Hitzenberger, G. Kamp, and S. Y. El-Zaiat, "Measurement of intraocular distances by backscattering spectral interferometry," *Optics Communications*, vol. 117, no. 1–2, pp. 43–48, May 1995.
[46] M. Wojtkowski, R. Leitgeb, A. Kowalczyk, T. Bajraszewski, and A. F. Fercher, "In vivo human retinal imaging by Fourier domain optical coherence tomography," *J Biomed Opt*, vol. 7, no. 3, pp. 457–463, Jul. 2002.

[47] S. Yun, G. Tearney, B. Bouma, B. Park, and J. de Boer, "High-speed spectral-domain optical coherence tomography at 1.3 ?m wavelength," *Opt. Express*, vol. 11, no. 26, pp. 3598–3604, Dec. 2003.
[48] B. Cense, N. Nassif, T. Chen, M. Pierce, S.-H. Yun, B. Park, B. Bouma, G. Tearney, and J. de Boer, "Ultrahigh-resolution high-speed retinal imaging using spectral-domain optical coherence tomography," *Opt. Express*, vol. 12, no. 11, pp. 2435–2447, May 2004.
[49] N. Nassif, B. Cense, B. Hyle Park, S. H. Yun, T. C. Chen, B. E. Bouma, G. J. Tearney, and J. F. de Boer, "In vivo human retinal imaging by ultrahigh-speed spectral domain optical coherence tomography," *Opt. Lett.*, vol. 29, no. 5, pp. 480–482, Mar. 2004.
[50] M. Wojtkowski, V. J. Srinivasan, T. H. Ko, J. G. Fujimoto, A. Kowalczyk, and J. S. Duker, "Ultrahigh-resolution, high-speed, Fourier domain optical coherence tomography and methods for dispersion compensation," *Optics Express*, vol. 12, no. 11, p. 2404, 2004.
[51] S. Makita, T. Fabritius, and Y. Yasuno, "Full-range, high-speed, high-resolution 1-?m spectral-domain optical coherence tomography using BM-scan for volumetric imaging of the human posterior eye," *Opt. Express*, vol. 16, no. 12, pp. 8406–8420, Jun. 2008.
[52] Y. Zhang, B. Cense, J. Rha, R. S. Jonnal, W. Gao, R. J. Zawadzki, J. S. Werner, S. Jones, S. Olivier, and D. T. Miller, "High-speed volumetric imaging of cone photoreceptors with adaptive optics spectral-domain optical coherence tomography," *Opt Express*, vol. 14, no. 10, pp. 4380–4394, May 2006.
[53] B. Potsaid, I. Gorczynska, V. J. Srinivasan, Y. Chen, J. Jiang, A. Cable, and J. G. Fujimoto, "Ultrahigh speed Spectral / Fourierdomain OCT ophthalmic imaging at70,000 to 312,500 axial scans per second," *Opt. Express*, vol. 16, no. 19, pp. 15149–15169, 2008.
[54] M. Wojtkowski, V. Srinivasan, J. G. Fujimoto, T. Ko, J. S. Schuman, A. Kowalczyk, and J. S. Duker, "Three-dimensional retinal imaging with high-speed ultrahigh-resolution optical coherence tomography," *Ophthalmology*, vol. 112, no. 10, pp. 1734–1746, Oct. 2005.
[55] V. J. Srinivasan, M. Wojtkowski, A. J. Witkin, J. S. Duker, T. H. Ko, M. Carvalho, J. S. Schuman, A. Kowalczyk, and J. G. Fujimoto, "High-Definition and 3-dimensional Imaging of Macular Pathologies with High-speed Ultrahigh-Resolution Optical Coherence Tomography," *Ophthalmology*, vol. 113, no. 11, pp. 2054.e1–2054.14, Nov. 2006.
[56] M. Ruggeri, H. Wehbe, S. Jiao, G. Gregori, M. E. Jockovich, A. Hackam, Y. Duan, and C. A. Puliafito, "In vivo three-dimensional high-resolution imaging of rodent retina with spectral-domain optical coherence tomography," *Invest. Ophthalmol. Vis. Sci.*, vol. 48, no. 4, pp. 1808–1814, Apr. 2007.
[57] G. Vizzeri, M. Balasubramanian, C. Bowd, R. N. Weinreb, F. A. Medeiros, and L. M. Zangwill, "Spectral domain-optical coherence tomography to detect localized retinal nerve fiber layer defects in glaucomatous eyes," *Opt. Express*, vol. 17, no. 5, pp. 4004–4018, Mar. 2009.
[58] S. R. Chinn, E. A. Swanson, and J. G. Fujimoto, "Optical coherence tomography using a frequency-tunable optical source," *Opt. Lett.*, vol. 22, no. 5, pp. 340–342, Mar. 1997.
[59] B. Golubovic, B. E. Bouma, G. J. Tearney, and J. G. Fujimoto, "Optical frequency-domain reflectometry using rapid wavelength tuning of a Cr4+:forsterite laser," *Opt. Lett.*, vol. 22, no. 22, pp. 1704–1706, Nov. 1997.

[60] W. Y. Oh, S. H. Yun, B. J. Vakoc, G. J. Tearney, and B. E. Bouma, "Ultrahigh-speed optical frequency domain imaging and application to laser ablation monitoring," *Applied Physics Letters*, vol. 88, no. 10, pp. 103902–103902–3, Mar. 2006.
[61] M. E. Brezinski, *Optical Coherence Tomography: Principles and Applications*, 1st ed. Academic Press, 2006.
[62] S. Yun, G. Tearney, J. de Boer, N. Iftimia, and B. Bouma, "High-speed optical frequency-domain imaging," *Opt. Express*, vol. 11, no. 22, pp. 2953–2963, Nov. 2003.
[63] D. C. Adler, R. Huber, and J. G. Fujimoto, "Phase-sensitive optical coherence tomography at up to 370,000 lines per second using buffered Fourier domain mode-locked lasers," *Opt. Lett.*, vol. 32, no. 6, pp. 626–628, Mar. 2007.
[64] R. Huber, M. Wojtkowski, and J. G. Fujimoto, "Fourier Domain Mode Locking (FDML): A new laser operating regime and applications for optical coherence tomography," *Opt. Express*, vol. 14, no. 8, pp. 3225–3237, Apr. 2006.
[65] S. H. Yun, G. J. Tearney, B. J. Vakoc, M. Shishkov, W. Y. Oh, A. E. Desjardins, M. J. Suter, R. C. Chan, J. A. Evans, I.-K. Jang, N. S. Nishioka, J. F. de Boer, and B. E. Bouma, "Comprehensive volumetric optical microscopy in vivo," *Nature Medicine*, vol. 12, no. 12, pp. 1429–1433, Nov. 2006.
[66] D. C. Adler, Y. Chen, R. Huber, J. Schmitt, J. Connolly, and J. G. Fujimoto, "Three-dimensional endomicroscopy using optical coherence tomography," *Nature Photonics*, vol. 1, no. 12, pp. 709–716, 2007.
[67] D. C. Adler, C. Zhou, T.-H. Tsai, J. Schmitt, Q. Huang, H. Mashimo, and J. G. Fujimoto, "Three-dimensional endomicroscopy of the human colon using optical coherence tomography," *Opt. Express*, vol. 17, no. 2, pp. 784–796, Jan. 2009.
[68] M.-T. Tsai, H.-C. Lee, C.-W. Lu, Y.-M. Wang, C.-K. Lee, C. C. Yang, and C.-P. Chiang, "Delineation of an oral cancer lesion with swept-source optical coherence tomography," *J Biomed Opt*, vol. 13, no. 4, p. 044012, Aug. 2008.
[69] Y. Pan, R. Birngruber, J. Rosperich, and R. Engelhardt, "Low-coherence optical tomography in turbid tissue: theoretical analysis," *Appl. Opt.*, vol. 34, no. 28, pp. 6564–6574, Oct. 1995.
[70] J. M. Schmitt, "Optical coherence tomography (OCT): a review," *Selected Topics in Quantum Electronics, IEEE Journal of*, vol. 5, no. 4, pp. 1205 –1215, Aug. 1999.
[71] R. K. Wang, "Resolution improved optical coherence-gated tomography for imaging through biological tissues," *Journal of Modern Optics*, vol. 46, no. 13, pp. 1905–1912, 1999.
[72] C. Akcay, P. Parrein, and J. P. Rolland, "Estimation of Longitudinal Resolution in Optical Coherence Imaging," *Appl. Opt.*, vol. 41, no. 25, pp. 5256–5262, 2002.
[73] M. D. Kulkarni, C. W. Thomas, and J. A. Izatt, "Image enhancement in optical coherence tomography using deconvolution," *Electronics Letters*, vol. 33, no. 16, pp. 1365 –1367, Jul. 1997.
[74] K. M. Yung, S. L. Lee, and J. M. Schmitt, "Phase-Domain Processing of Optical Coherence Tomography Images," *Journal of Biomedical Optics*, vol. 4, no. 1, p. 125, 1999.
[75] Fujimoto, J. G. 2002. Alternative OCT Techniques(Chapter 13) In Handbook of Optical Coherence Tomography. ed. C.K.Hitzenberger and A. F. Fercher. New York, USA.: Marcel Dekker, Inc., .

[76] M. E. Brezinski and J. G. Fujimoto, "Optical coherence tomography: high-resolution imaging in nontransparent tissue," *Selected Topics in Quantum Electronics, IEEE Journal of*, vol. 5, no. 4, pp. 1185 –1192, Aug. 1999.
[77] W. Drexler, C. K. Hitzenberger, A. Baumgartner, O. Findl, H. Sattmann, and A. F. Fercher, "Investigation of dispersion effects in ocular media by multiple wavelength partial coherence interferometry," *Exp. Eye Res.*, vol. 66, no. 1, pp. 25–33, Jan. 1998.
[78] C. K. Hitzenberger, A. Baumgartner, W. Drexler, and A. F. Fercher, "Dispersion Effects in Partial Coherence Interferometry: Implications for Intraocular Ranging," *Journal of Biomedical Optics*, vol. 4, no. 1, p. 144, 1999.
[79] *Optical Coherence Tomography: Technology and Applications*. Springer, 2008.
[80] M. Gora, K. Karnowski, M. Szkulmowski, B. J. Kaluzny, R. Huber, A. Kowalczyk, and M. Wojtkowski, "Ultra high-speed swept source OCT imaging of the anterior segment of human eye at 200 kHz with adjustable imaging range," *Opt. Express*, vol. 17, no. 17, pp. 14880–14894, 2009.
[81] Y. Yasuno, V. D. Madjarova, S. Makita, M. Akiba, A. Morosawa, C. Chong, T. Sakai, K.-P. Chan, M. Itoh, and T. Yatagai, "Three-dimensional and high-speed swept-source optical coherence tomography for in vivo investigation of human anterior eye segments," *Opt. Express*, vol. 13, no. 26, pp. 10652–10664, Dec. 2005.
[82] B. Povazay, K. Bizheva, A. Unterhuber, B. Hermann, H. Sattmann, A. F. Fercher, W. Drexler, A. Apolonski, W. J. Wadsworth, J. C. Knight, P. S. J. Russell, M. Vetterlein, and E. Scherzer, "Submicrometer axial resolution optical coherence tomography," *Opt. Lett.*, vol. 27, no. 20, pp. 1800–1802, Oct. 2002.
[83] A. Dubois, G. Moneron, K. Grieve, and A. C. Boccara, "Three-dimensional cellular-level imaging using full-field optical coherence tomography," *Phys Med Biol*, vol. 49, no. 7, pp. 1227–1234, Apr. 2004.
[84] A. Wax, C. Yang, and J. A. Izatt, "Fourier-domain low-coherence interferometry for light-scattering spectroscopy," *Opt. Lett.*, vol. 28, no. 14, pp. 1230–1232, Jul. 2003.
[85] A. Unterhuber, B. Povazay, K. Bizheva, B. Hermann, H. Sattmann, A. Stingl, T. Le, M. Seefeld, R. Menzel, M. Preusser, H. Budka, C. Schubert, H. Reitsamer, P. K. Ahnelt, J. E. Morgan, A. Cowey, and W. Drexler, "Advances in broad bandwidth light sources for ultrahigh resolution optical coherence tomography," *Phys Med Biol*, vol. 49, no. 7, pp. 1235–1246, Apr. 2004.
[86] F. Spoler, S. Kray, P. Grychtol, B. Hermes, J. Bornemann, M. Forst, and H. Kurz, "Simultaneous dual-band ultra-high resolution optical coherence tomography," *Opt. Express*, vol. 15, no. 17, pp. 10832–10841, 2007.
[87] M. B. Nasr, O. Minaeva, G. N. Goltsman, A. V. Sergienko, B. E. Saleh, and M. C. Teich, "Submicron axial resolution in an ultrabroadband two-photon interferometer using superconducting single-photon detectors," *Opt Express*, vol. 16, no. 19, pp. 15104–15108, Sep. 2008.
[88] J. M. Schmitt, "Restoration of Optical Coherence Images of Living Tissue Using the CLEAN Algorithm," *Journal of Biomedical Optics*, vol. 3, no. 1, p. 66, Jan. 1998.
[89] T. S. Ralston, D. L. Marks, F. Kamalabadi, and S. A. Boppart, "Deconvolution methods for mitigation of transverse blurring in optical coherence tomography," *Image Processing, IEEE Transactions on*, vol. 14, no. 9, pp. 1254 –1264, Sep. 2005.

[90] Y. Takahashi, Y. Watanabe, and M. Sato, "Application of the maximum entropy method to spectral-domain optical coherence tomography for enhancing axial resolution," *Appl. Opt.*, vol. 46, no. 22, pp. 5228–5236, 2007.
[91] J. Gong, B. Liu, Y. L. Kim, Y. Liu, X. Li, and V. Backman, "Optimal spectral reshaping for resolution improvement in optical coherence tomography," *Opt Express*, vol. 14, no. 13, pp. 5909–5915, Jun. 2006.
[92] S. Carrasco, J. P. Torres, L. Torner, A. Sergienko, B. E. A. Saleh, and M. C. Teich, "Enhancing the axial resolution of quantum optical coherence tomography by chirped quasi-phase matching," *Opt Lett*, vol. 29, no. 20, pp. 2429–2431, Oct. 2004.
[93] 15. J. D. Taylor, Ultra wideband radar technology, (CRC press LLC, 2001), Chap. 11., .
[94] T. Misaridis and J. A. Jensen, "Use of modulated excitation signals in medical ultrasound. Part I: basic concepts and expected benefits," *Ultrasonics, Ferroelectrics and Frequency Control, IEEE Transactions on*, vol. 52, no. 2, pp. 177 –191, Feb. 2005.
[95] W. H. RICHARDSON, "Bayesian-Based Iterative Method of Image Restoration," *J. Opt. Soc. Am.*, vol. 62, no. 1, pp. 55–59, Jan. 1972.
[96] A. Kartakoullis, E. Bousi, and C. Pitris, "Scatterer size-based analysis of optical coherence tomography images using spectral estimation techniques," *Opt. Express*, vol. 18, no. 9, pp. 9181–9191, Apr. 2010.
[97] X. Liu and J. U. Kang, "Progress toward inexpensive endoscopic high-resolution common-path OCT," *Proceedings of SPIE*, vol. 7559, no. 1, pp. 755902–755902–11, Feb. 2010.
[98] B. Hermann, E. J. Fernandez, A. Unterhuber, H. Sattmann, A. F. Fercher, W. Drexler, P. M. Prieto, and P. Artal, "Adaptive-optics ultrahigh-resolution optical coherencetomography," *Opt. Lett.*, vol. 29, no. 18, pp. 2142–2144, 2004.
[99] Z. Ding, H. Ren, Y. Zhao, J. S. Nelson, and Z. Chen, "High-resolution optical coherence tomography over a large depth range with an axicon lens," *Opt. Lett.*, vol. 27, no. 4, pp. 243–245, Feb. 2002.
[100] M. J. Cobb, X. Liu, and X. Li, "Continuous focus tracking for real-time optical coherence tomography," *Opt. Lett.*, vol. 30, no. 13, pp. 1680–1682, Jul. 2005.
[101] T. S. Ralston, D. L. Marks, P. S. Carney, and S. A. Boppart, "Inverse scattering for optical coherence tomography," *J. Opt. Soc. Am. A*, vol. 23, no. 5, pp. 1027–1037, May 2006.
[102] T. S. Ralston, D. L. Marks, S. A. Boppart, and P. S. Carney, "Inverse scattering for high-resolution interferometric microscopy," *Opt. Lett.*, vol. 31, no. 24, pp. 3585–3587, Dec. 2006.
[103] T. S. Ralston, D. L. Marks, P. S. Carney, and S. A. Boppart, "Interferometric synthetic aperture microscopy," *Nature Physics*, vol. 3, no. 2, pp. 129–134, 2007.
[104] L. Yu, B. Rao, J. Zhang, J. Su, Q. Wang, S. Guo, and Z. Chen, "Improved lateral resolution in optical coherence tomography by digital focusing using two-dimensional numerical diffraction method," *Opt. Express*, vol. 15, no. 12, pp. 7634–7641, Jun. 2007.
[105] Y. Yasuno, J. Sugisaka, Y. Sando, Y. Nakamura, S. Makita, M. Itoh, and T. Yatagai, "Non-iterative numerical method for laterally superresolving Fourier domain optical coherence tomography," *Opt. Express*, vol. 14, no. 3, pp. 1006–1020, Feb. 2006.

[106] G. Liu, S. Yousefi, Z. Zhi, and R. K. Wang, "Automatic estimation of point-spread-function for deconvoluting out-of-focus optical coherence tomographic images using information entropy-based approach," *Opt. Express*, vol. 19, no. 19, pp. 18135–18148, 2011.
[107] T.-Y. Yu, G. Zhang, A. B. Chalamalasetti, R. J. Doviak, and D. Zrníc, "Resolution Enhancement Technique Using Range Oversampling," *Journal of Atmospheric and Oceanic Technology*, vol. 23, no. 2, pp. 228–240, Feb. 2006.
[108] R. T. Lacoss, "DATA ADAPTIVE SPECTRAL ANALYSIS METHODS," *Geophysics*, vol. 36, no. 4, p. 661, Aug. 1971.
[109] J. Li and P. Stoica, "An adaptive filtering approach to spectral estimation and SAR imaging," *Signal Processing, IEEE Transactions on*, vol. 44, no. 6, pp. 1469 –1484, Jun. 1996.
[110] P. Stoica, A. Jakobsson, and J. Li, *Matched-Filter Bank Interpretation of Some Spectral Estimators*. .
[111] T. M. Lee, A. L. Oldenburg, S. Sitafalwalla, D. L. Marks, W. Luo, F. J.-J. Toublan, K. S. Suslick, and S. A. Boppart, "Engineered microsphere contrast agents for optical coherence tomography," *Opt. Lett.*, vol. 28, no. 17, pp. 1546–1548, Sep. 2003.
[112] C. Pitris, C. Jesser, S. A. Boppart, D. Stamper, M. E. Brezinski, and J. G. Fujimoto, "Feasibility of optical coherence tomography for high-resolution imaging of human gastrointestinal tract malignancies," *J. Gastroenterol.*, vol. 35, no. 2, pp. 87–92, 2000.
[113] G. Isenberg, M. V. Sivak Jr, A. Chak, R. C. K. Wong, J. E. Willis, B. Wolf, D. Y. Rowland, A. Das, and A. Rollins, "Accuracy of endoscopic optical coherence tomography in the detection of dysplasia in Barrett's esophagus: a prospective, double-blinded study," *Gastrointest. Endosc.*, vol. 62, no. 6, pp. 825–831, Dec. 2005.

List of publications out of thesis

Book chapters

I. C. Pitris, A. Kartakoullis, and E. Bousi. “Chapter 14: Optical Coherence Tomography Theory and Spectral Time-Frequency Analysis,” in the “Handbook of Photonics for Biomedical Science,” V. Tuchin, ed, pp.299-326. CRC Press, 2010. ISBN: 9781439806289.

II. Y. Chen, E. Bousi, C. Pitris, and J.G. Fujimoto, “Optical Coherence Tomography: Introduction and Theory,” D. Boas, C. Pitris, N. Rammanujam, eds, in press. CRC Press, 2010. ISBN 1420090364

Journals

I. Evgenia Bousi and Costas Pitris, "Axial resolution improvement by modulated deconvolution in Fourier domain optical coherence tomography", J. Biomed. Opt. 17, 071307 (May 16, 2012)

II. Bousi, I. Charalambous, C. Pitris. “Axial resolution improvement in Time domain Optical Coherence Tomography by step-frequency encoding.” Optics Express, Vol. 18, Issue 11, pp 11877-11890 (2010)

III. A. Kartakoulis, E. Bousi, C. Pitris. “Scatterer size-based analysis of optical coherence tomography images using spectral estimation techniques.” Optics Express, 18: 9181-9191, 2010

IV. C. Pitris, A. Kartakoullis, E. Bousi, “AM-FM techniques in the analysis of optical coherence tomography signals,” J. of Biophotonics, 2: 364-369,2009.

V. E. Bousi, C. Pitris, “Lateral resolution improvement in oversampled optical coherence tomography images”, Submitted for publication .

Conferences

I. Evgenia Bousi and Costas Pitris, "Lateral resolution improvement in oversampled optical coherence tomography images assuming weighted oversampled multi-scatterer contributions", Proc. SPIE 8213, 82132T (2012).

II. Evgenia Bousi, Ismini Charalambous and Costas Pitris, "Fourier domain optical coherence tomography axial resolution improvement with modulated deconvolution", Proc. SPIE 8091, 80910P (2011),Conference on Biomedical Optics, Munich, Germany, May 23-29, 2011

III. E. Bousi, I. Charalambous, C. Pitris, “Modulated deconvolution for resolution improvement in Fourier domain optical coherence tomography,” Proc. SPIE 7889, 78893A, (2011), Photonics West, San Francisco, California USA, January 21–27, 2011.

IV. E. Bousi, I. Charalambous, C. Pitris, “Optical coherence tomography resolution improvement by step-frequency encoding,” Proc. SPIE 7554, 75541W (2010), Photonics West, San Francisco, California USA, January 23–28, 2010.

V. A. Kartakoullis, E. Bousi, C. Pitris, “AM-FM techniques in optical coherence tomography,” Proc. SPIE 7372, 73720U (2009), European Conference on Biomedical Optics, Munich, Germany, June 14-19, 2009.

VI. A. Kartakoulis, E. Bousi, C. Pitris, “AM-FM analysis of optical coherence tomography signals,” Proc. SPIE 7168, 71681M (2009), Photonics West, San Jose, California USA, January 24–29, 2009.

VII. E. Bousi, A. Kartakoullis, C. Pitris, “Spectral Analysis for Scatterer Estimation in Optical Coherence Tomography Images,” IEEE 9th International Conference on Information Technology and Applications in Biomedicine, November 5-7, 2009, Larnaca, Cyprus, DOI: 10.1109/ITAB.2009.5394413.